Predicting and analyzing geometric and morphing wing characteristics of the Grey-Headed Albatross

by

Alexander Ernest Winter (17001430)

supervised by

Dr. Lelanie Smith

Janine Schoombie

A dissertation presented for partial fulfilment of

Master of Engineering (Mechanical)

Department of Mechanical and Aeronautical Engineering

University of Pretoria

South Africa

Abstract

Geometric and aerodynamic properties of various avian species allow engineers and biologists to gain valuable insight into the evolutionary honing of the capabilities of natural flyers. Very little research has been done to establish reliable 3D models and detailed descriptions of the aerodynamic characteristics of the Grey-headed Albatross. Therefore, the purpose of this work was to determine the static and passively morphed geometric and aerodynamic characteristics of the Grey-headed Albatross. A laser scanned 3D point cloud of a Grey-headed Albatross wing specimen was used to obtain spanwise airfoils using the PARSEC method, a novel method to the field of avian wings. A single objective optimization study using a pseudo 2D computational fluid dynamics model was done on an averaged airfoil of the arm section of the Grey-headed Albatross to determine the maximum potential aerodynamic efficiency (lift-to-drag-ratio) at a Reynolds number of 2×10^5. This delivered the first reliable estimate of the passive morphing that an avian wing undergoes. The optimized Grey-headed Albatross airfoil decreased in camber creating a more streamlined body when compared to the highly cambered static airfoil. The optimized airfoil exhibited a maximum lift-to-drag ratio of 44 ($\alpha_{\text{actual}} = -0.5°$, $\alpha_{\text{geometric}} = -11.5°$) when compared to the baseline airfoil with a lift-to-drag ratio of 3 ($\alpha = 16°$). The increase in lift-to-drag ratio was partly due to the drastic decrease in pressure drag from 0.395 to 0.029 between the static and optimized airfoil, a decrease by a factor of 13.6. The optimized airfoil geometry was similar to that of a 3D laser scan which was done on a GHA wing in the presence of airflow. The increase of the aerodynamic efficiency is consistent with the notion that Grey-headed Albatrosses are efficient flyers.

Acknowledgements

I would like to start off by thanking my supervisors, Dr. Lelanie Smith and Janine Schoombie for their valuable input into this research. I would not have been able to complete this research without their experience and knowledge.

Then I would like to thank my parents, who enabled me to pursue this degree. Without them it would not have been possible. My wife, Petria, thanks for all your input and experience and guiding my academic writing. Thanks for keeping me accountable and motivating me through this journey.

Abstract ii

Acknowledgements iii

List of Figures vi

List of Tables xi

List of Symbols xii

List of Abbreviations xiv

1. Background 1
  - 1.1. Present day avian wing geometry analysis 1
  - 1.2. Bird wing Aerodynamics 2
  - 1.3. Research Gap 4
  - 1.4. Research Objectives 4
  - 1.5. Scope of work 5
  - 1.6. Structure of the dissertation 6

2. Literature Review 7
  - 2.1. The Grey-headed Albatross 7
  - 2.2. Previous work on avian wing geometries. 7
  - 2.3. Flight performance measurements of avian wings 10
    - 2.3.1. Biological and observed evidence 10
    - 2.3.2. Experimental estimations of avian flight efficiencies 11
  - 2.4. Relevant aerodynamic considerations 12
  - 2.5. Numerical modelling of low Reynolds number flow over airfoils 14
  - 2.6. Automated mesh refinement in CFD. 16
  - 2.7. Aerodynamic optimization of parameterized wings to capture dynamic morphing of wings 18

3. The Geometry of the Grey-headed Albatross 20
  - 3.1. Proposing a new airfoil parameterization method for avian wings 20
  - 3.2. Validation of the PARSEC Method 22
  - 3.3. Pre-processing Point Cloud data 26

3.4. Quantified geometry of the Grey-headed Albatross Wing ... 32
4. Validation of the numerical approach ... 42
4.1. Pseudo Two-Dimensional Domain Set-up ... 42
4.2. Benchmark Results ... 46
4.3. Meshing refinement strategy for optimization of different geometries ... 51
5. Aerodynamic Optimization of the Parametric model ... 60
5.1. The Parametric model of the Grey-headed Albatross ... 60
5.2. Calculating the Design Space ... 60
5.3. Optimized geometry of a Grey-headed Albatross airfoil ... 65
5.4. Aerodynamic findings of the optimized GHA airfoil ... 71
5.4.1. Steady and unsteady state validation study ... 71
5.4.2. Unsteady results of aerodynamic analyses on optimized GHA airfoil ... 72
6. Conclusions and Recommendations ... 79
6.1. Reconstructing the GHA wing ... 79
6.2. Modelling the aerodynamics of the GHA wing ... 80
6.3. Recommendations for Future Work ... 81
Bibliography ... 83
Appendix A – Optimizer comparison for calculating PARSEC Parameters ... 91
Appendix B – Airfoils of the GHA ... 99
Appendix C – Mesh Independence Study Prism Layer Mesher ... 101
Appendix D – Mesh Independence Study Advancing Layer Mesh ... 105
Appendix E – JAVA macro used for geometry updating ... 107
Appendix F – PARSEC Parameter Bound Investigation ... 113

List of Figures

Figure 1: The anatomy of an avian wing (König et al., 2016). 7

Figure 2: Eppler 387 (E387) airfoil used as an example to illustrate the requirements of a postprocessed airfoil. 8

Figure 3: (a) Seagull wing reconstructed by Liu et al. (2006) (b) Owl wing reconstructed by Klän et al. (2009) (c) Steppe eagle wing reconstructed by Carruthers et al. (2010) (d) Unknown wing reconstructed by Waldrop et al. (2020) and Rader et al. (2020). 10

Figure 4: 2D Laminar Separation Bubble formation (Horton, 1968). 14

Figure 5: An airfoil showing the 12 PARSEC parameters and their geometrical meaning [Reproduced from Sobieczky (1997, 1999)]. 20

Figure 6: Flowchart showing the process for determining the PARSEC parameters given the coordinates which makes up an airfoil. 23

Figure 7: Recreated E387 airfoil with the upper and lower errors with GD and DE. Times: GD: 0.25s, DE: 38.57s 25

Figure 8: A raw scatter plot of a 3D scanned airfoil of the GHA showing examples of open sections (orange) and outlier regions (green). 27

Figure 9: The airfoil creation process in CloudCompare showing (a) the lines where the sections were to be taken and (b) the result of the sectioning process. 28

Figure 10: Imported points as exported from CloudCompare. 28

Figure 11: Manually rotated points which aimed to ensure that airflow in the positive x direction would meet the leading edge first. 28

Figure 12: Data sorted in increasing x 29

Figure 13: Translating the data to have the leading edge located at the origin. 29

Figure 14: Rotating the points to ensure that the leading and trailing edges are exactly horizontal. 29

Figure 15: The quantities that were being monitored to ensure that the transforms did not induce new leading and/or trailing edges. 30

Figure 16: The points were scaled to a chord length of unity and the Birnbaum-Glauert camber line was fit to the data for the purpose of splitting the upper and lower surfaces. 31

Figure 17: The upper and lower surfaces split using the Birnbaum-Glauert camber line. 31

Figure 18: Sinusoidal spacing of x values used for the interpolation of the airfoil data. 31

Figure 19: Interpolated and sequenced data ready for use in the next part of the geometry investigation. 32

Figure 20: A comparison between the PARSEC method and the Birnbaum-Glauert method for calculating the (a) camber and (b) calculating the deviation between the actual camber (absolute value), and the PARSEC and Birnbaum-Glauert methods normalized by $c = 0.2$m. 34

Figure 21: A comparison between the PARSEC method and the Birnbaum-Glauert method for calculating the (a) thickness and (b) calculating the deviation between the actual thickness (absolute value), and the PARSEC and Birnbaum-Glauert methods normalized by $c = 0.2$m. 35

Figure 22: Local chord length, local twist, sweep, and dihedral as functions of the normalized wingspan of the GHA. The original data is plotted using the circular markers and the smoothed data is plotted using the line. 37

Figure 23: Visualization of the quarter chord location from the x translation and c values captured, for three arbitrarily spaced airfoils in the spanwise direction. The light grey line can be seen running through the quarter chord positions. The sweep angle is indicated by β. 37

Figure 24: Visualization of the quarter chord location from the z translation and the c values captured, for three arbitrarily spaced airfoils in the spanwise direction. The light grey line can be seen running through the quarter chord positions. The dihedral angle is indicated by γ. 38

Figure 25: Recreated GHA wing constructed from the macro wing parameters. (Grey lines on the Side View and Top View are included to indicate the twist). 39

Figure 26: Average arm and hand section airfoils as calculated using the PARSEC parameters. 40

Figure 27: GHA 3D CAD model created using the data presented in this section compared to a raw 3D scan showing the (a,b) top view (c,d) left view (e,f) front view, and (g,h) isometric view. 41

Figure 28: Domain used for the pseudo two-dimensional study showing the (a) right view and (b) front view. 42

Figure 29: The mesh used for the P2D study showing the (a) the entire domain with the two refinement regions (black arrow with cell sizes of $0.02c$ and red arrow with cell sizes of $0.08c$) and (b) the near airfoil mesh showing the prism layers. For this example, the flow vector is parallel to the arrows in (a). 44

Figure 30: Results using (a) 60 chord lengths of wake refinement and (b) 2 chord lengths of wake refinement at $\alpha = 4\circ$ and $\mathrm{Re} = 2 \times 105$ showing the laminar separation and turbulent reattachment locations as solid lines. 45

Figure 31: Change in CL and CD for the successive refinements 46

Figure 32: CL and CD results obtained for the angle of attack sweep for the E387 airfoil. 47

Figure 33: Pressure coefficient CP results obtained from an angle of attack sweep at (a) $\alpha = 0\circ$(b) $\alpha = 2\circ$ (c) $\alpha = 4\circ$ (d) $\alpha = 6\circ$ (e) $\alpha = 8\circ$using the advancing layer mesher, compared to result obtained by McGhee and Walker (1989). The laminar separation and turbulent reattachment locations are shown as solid lines. 50

Figure 34: Laminar separation (solid lines) and turbulent reattachment (dashed lines) locations as the angle of attack changes compared to experimental results in the literature. 51

Figure 35: The mesh generated and adaptively refined using the AMR technique discussed above for $\alpha = 8\circ$. The black arrow shows the $20c$ wake refinement done manually, and the red arrow shows the region where the mesh was adaptively refined. 53

Figure 36: CL and CD as function of α. 54

Figure 37: The coefficient of pressure results for the E387 using AMR compared to results from the literature fore (a) $\alpha = 0\circ$ (b) $\alpha = 4\circ$ (c) $\alpha = 8\circ$. The vertical blue and orange lines indicate the laminar separation and turbulent reattachment locations on the airfoil. The blue lines indicate the locations of this study, and the orange lines indicate the locations of McGhee and Walker (1989) 56

Figure 38: (a) CL and (b) CD plotted against the number of iterations comparing the steady and unsteady solver. 57

Figure 39: Normalized velocity magnitude contour plot comparing the steady and unsteady solver at $\mathrm{Re} = 2 \times 105$ and $\alpha = 8\circ$ for the S1223. 58

Figure 40: CL, CD as function of α compared to results obtained from XFOIL and Selig and Guglielmo (1997) 59

Figure 41: An airfoil showing the self-intersecting geometry caused when $Z\mathrm{up} \leq Z\mathrm{lo}$ for $X\mathrm{up} \simeq X\mathrm{lo}$ 61

Figure 42: Pigeon wings at $V1 = 5\mathrm{ms} - 1$, $V2 = 7.5\mathrm{ms} - 1$, $V3 = 10\mathrm{ms} - 1$ at a constant angle of attack of $\alpha = 10\circ$ (Nachtigall and Wieser, 1966). 64

Figure 43: Hypothesised GHA arm section wing under aerodynamic load and the airfoil produced by the PARSEC method using the bounds developed. 65

Figure 44: Aerodynamic quantities changing and improving as the number of designs tested increase. The red line shows the evolution of the best design. 66

Figure 45: Scatter plot showing each design's CD and CL. The aerodynamic efficiency is also indicated. The red line shows the evolution of the best design. 66
Figure 46: Scatter plot showing each PARSEC parameters changing for different designs. The aerodynamic efficiency is indicated with the colour of each design to give an indication on how it increases as the number of designs increase. 68
Figure 47: Spider plot showing the PARSEC parameters and angle of attack of 6 different designs, each increasing by roughly a count of 10 from the baseline design, shown in blue. 69
Figure 48: Airfoils created using the PARSEC parameters shown in Figure 47, each increasing in aerodynamic efficiency by roughly a count of 10. 70
Figure 49: The optimized airfoil of the GHA arm wing showing the aerodynamic efficiency and the angle of attack at the maximum efficiency. The dashed grey line indicates the baseline airfoil. The geometric angle of attack of the aerofoil is $-11.52 \circ$ due to the TE deflection and the flow angle is $11 \circ$. The net angle of attack (chord relative to airflow) is therefore $-0.52 \circ$. 70
Figure 50: Airfoil of the GHA in the presence of airflow at $V = 15\text{ms} - 1$ showing similar geometrical features when compared to the optimized airfoil. 71
Figure 52: The polars computed for the optimized GHA arm airfoil at $\text{Re} = 2 \times 105$ used to compare the two different solvers. 72
Figure 53: CL vs α polar comparison for the optimized airfoil and the baseline airfoil at $\text{Re} = 2 \times 105$. 73
Figure 54: CD vs α polar comparison for the optimized airfoil and the baseline airfoil at $\text{Re} = 2 \times 105$. 74
Figure 55: CF vs x/c at $\text{Re} = 2 \times 105$ for the (a) baseline GHA airfoil at $\alpha = 15 \circ$ and the (b) optimized GHA airfoil at $10 \circ$ showing the separation and reattachment locations as vertical lines. 75
Figure 56: Normalized velocity magnitude contour plot for the (a) baseline GHA airfoil and the (b) optimized GHA airfoil. 76
Figure 57: Normalized velocity profiles in the x direction as a function of the vertical height for different streamwise stations. 77
Figure 58: CL/CD vs α polar comparison for the optimized GHA airfoil and the GHA arm airfoil. 78
Figure 51: Optimized airfoil of the GHA showing the upper and lower crest locations which are required to have gradient of zero. 82
Figure 59: E387 GD: 0.25s, DE: 38.57s 91

Figure 60: E423 GD: 0.14s, DE: 13.25s ... 92
Figure 61: GOE176 GD: 0.20s, DE: 11.10s ... 93
Figure 62: GOE676 GD: 0.18s, DE: 11.68s ... 94
Figure 63: NACA0012 GD: 0.14s, DE: 15.01s ... 95
Figure 64: NACA0024 GD: 0.44s, DE: 14.93s ... 96
Figure 65: NACA6409, GD: 0.18s, 14.59s ... 97
Figure 66: S1223, GD: 0.20s, DE: 17.42s ... 98
Figure 67: The airfoils created using the PARSEC method for different spanwise locations ... 99
Figure 68: Pressure distributions for (a) coarse mesh (b) medium mesh and (c) fine mesh showing the separation and reattachment locations and CL and CD values. ... 102
Figure 69: Change in CL and CD for the successive refinements ... 103
Figure 70: The trailing edge prismatic cells using the (a) prism layer mesher and (b) the advancing layer mesher ... 104
Figure 71: Pressure distributions for (a) coarse mesh (b) medium mesh and (c) fine mesh showing the separation and reattachment locations and CL and CD values. ... 105
Figure 72: Change in CL and CD for the successive refinements ... 106
Figure 73: Covariance matrix of the failed designs with $\delta = 0.5$ ... 113
Figure 74: Scatter plots of each PARSEC parameter as a function of every other PARSEC parameter for all failed designs with $\delta = 0.5$. ... 114
Figure 75: Covariance matrix of the PARSEC parameters after adjusting the bounds. 115

List of Tables

Table 1: A summary of the physical properties of the Grey-headed Albatross 7
Table 2: The 12 PARSEC Parameters 20
Table 3 Bounds used to determine PARSEC parameters of common airfoils using two different methods of optimization. 25
Table 4: Average PARSEC parameters and standard deviations for the arm and hand section of the GHA wing. 40
Table 5: Flow variables used in the numerical analyses. 42
Table 6: PARSEC parameters of the optimized GHA arm airfoil compared to the baseline values indicating the change in each parameter. 71
Table 7: Quantities calculated for the mesh independence study performed at $\alpha = 4 \circ$ and $\mathrm{Re} = 2 \times 105$ 103
Table 8: Quantities calculated for the mesh independence study performed at $\alpha = 4 \circ$ and $\mathrm{Re} = 2 \times 105$ 106
Table 9: PARSEC parameters bounds and baseline values for the arm section (a) before (50% success rate) and (b) after (80% success rate) updating the Xlo, Xup,βte, and Zte bounds. 116
Table 10: PARSEC parameters bounds and baseline values for the hand section (a) before (50% success rate) and (b) after (80% success rate) updating the Xlo, Xup,βte, and Zte bounds. 116

List of Symbols

Latin

p	Arbitrary Parsec Parameter	-
A	Brinbaum-Glauer Coefficient	-
F	Centered and Scaled Failure Matrix	-
c	Chordlength	m
C	Coefficient	-
x	Design Vector	-
D	Drag Force	N
f	Failure Matrix	-
w	Flow Field Variables	-
f	Function/Objective Function	-
g	Gravitational Acceleration	ms^{-2}
k	Kilo	-
l	Length	m
L	Lift Force	N
M	Million	-
β	PARSEC Angle	deg
a	PARSEC Coefficient	-
b	PARSEC Coefficient	-
p	PARSEC Column Vector of an arbitrary parameter	-
P	PARSEC Parameter Vector	-
X	PARSEC Positional Coordinate	-
Z	PARSEC Positional Coordinate	
z	Positional Coordinate	m
x	Positional Coordinate	m
y	Positional Coordinate	m
P	Pressure	Pa
S	Projected Area/Birnbaum Glauert Coefficient/Discretized Domain	m^2/-/-
r	Radius	m
r	Residual	-
Re	Reynolds Number	-
T	Sequence	-
U	Speed	ms^{-1}

t	Time	s
V	Velocity	ms^{-1}

Greek

α	Angle of Attack	Deg
ρ	Density	kgm^{-3}
μ	Dynamic Viscosity	kg/(ms)
γ	Intermittency	-
η	Normalized Chordlength	-
δ	Sensitivity/Increment/Boundary Layer Thickness	-/-/m
τ	Shear Stress	Pa
ω	Specific Turbulent Dissipation Rate	s^{-1}
σ	Standard Deviation	-
k	Turbulent Kinetic Energy	J/kg
ϵ	Turbulent Dissipation Rate	J/kgs
θ	Twist Angle	Deg

Subscripts

actual	Actual
c	Camber
failed	Failed
∞	Freestream
F	Friction
0	Initial/Total
le	Leading Edge
L	Lift
lo	Lower
lower	Lower
l	Lower
max	Maximum
min	Minimum
model	Model

θ	Momentum Thickness
P	Pressure
xx	Second derivative in x
s	Sinking
t	Thickness
total	Total
te	Trailing Edge
translate	Translate
up	Upper
upper	Upper
u	Upper
w	Wall

Superscripts

d	Dimension
$+$	Non-dimensional
$*$	Optimal
T	Transpose

List of Abbreviations

AMR	Adaptive Mesh Refinement
.csv	Comma Separated Value
CFD	Computational Fluid Dynamics
CAD	Computer Aided Design
DE	Differential Evolution
GHA	Grey-headed Albatross
GCI	Grid Convergence Index
LSB	Laminar Separation Bubble
LTPT	Low-Turbulence Pressure Tunnel
MSE	Mean Squared Error
NACA	National Advisory Committee for Aeronautics
PIV	Particle Image Velocimetry
PCA	Principle Component Analysis

P2D	Pseudo 2-dimensional
RANS	Reynolds Averaged Navier Stokes
SST	Shear Stress Transport
SHERPA	Simultaneous Hybrid Exploration that is Robust, Progressive and Adaptive
S-A	Spallart Almaras
UAV	Unmanned Aerial Vehicle
URANS	Unsteady Reynolds Averaged Navier Stokes

1. Background

Birds are known to fly at speeds and Mach numbers which are similar to unmanned aerial vehicles (UAV) of roughly the same size (Harvey and Inman, 2021). The geometrical features of avian wings need to be determined after which the aerodynamic characteristics of an avian wing can be studied using modern numerical techniques or wind tunnel experiments. Gliding and soaring are excellent ways for birds to travel because they use less energy compared to flapping flight (Tucker, 1972; Baudinette and Schmidt-Nielsen, 1974; Sakamoto *et al.*, 2013; Duriez *et al.*, 2014). Albatrosses, in particular, are skilled at soaring for long distances, harnessing energy from the wind over the open ocean (Richardson, 2011; Sachs *et al.*, 2012). Despite the need to flap their wings more often than previously thought (Schoombie et al., 2023), albatrosses have evolved with high aspect ratio wings, similar to man-made gliders (Denny, 2009; Anderson, 2012).

Albatrosses are valuable subjects for studying fixed-wing aerodynamics, especially relevant for designing UAVs (unmanned aerial vehicles) at specific Reynolds numbers. Numerous researchers have found albatrosses to be useful for improving our understanding of this field (Pennycuick and Lighthill, 1982; Lazos, 2005; Henningsson and Hedenström, 2011; van Oorschot, Mistick and Tobalske, 2016; Harvey *et al.*, 2019; Usherwood *et al.*, 2020; Harvey and Inman, 2021).

1.1. Present day avian wing geometry analysis

Herzog (1968) used a sand moulding technique to investigate the wing cross sections of 46 different species of birds and included the wandering albatross (*Diomedea exulans*). There is little to no evidence of the methods used in doing so and it is believed that this could be the source of the Göttingen airfoils, GOE174 and GOE176, also called the Albatros 5020 and Albatros 7020, respectively. The moulding process that was used may have also altered the shape of the wing due to the weight of the sand packed around the wing. The levels of uncertainty are not quantified, and reliable geometrical properties of bird wings remain inconclusive.

More recently, the geometries of a seagull, merganser, teal, owl, and the steppe eagle wing has been investigated (Liu *et al.*, 2006; Klän *et al.*, 2009; Carruthers *et al.*, 2010; Wagner *et al.*, 2017). Liu et al. (2006) and Klan et al. (2009) use the Birnbaum-Glauert (BG) method which dates back to 1943. Klan et al. (2009) notes that the BG method led to non-realistic airfoil configurations and unsmooth spanwise airfoil shapes. The method used by Carruther et al. (2010) uses a polynomial regression technique for which no documentation is supplied through as few as 252 points. This would intuitively require large amounts of interpolation (and therfore uncertainty) between points.

A 3D model of a Grey-headed Albatross (GHA, *Thalassarche chrysostoma*) wing does not exist, and the development thereof will increase the understanding of the geometry of avian wings, especially seabirds which is hypothesized to be highly efficient.

1.2. Bird wing Aerodynamics

The aerodynamic characteristics of gliding birds have been studied multiple times using different approaches (Nachtigall and Wieser, 1966; Withers, 1981; Pennycuick and Lighthill, 1982; Liu *et al.*, 2006; Klän *et al.*, 2009; Henningsson and Hedenström, 2011; van Oorschot, Mistick and Tobalske, 2016; Wagner *et al.*, 2017; Harvey *et al.*, 2019; Omar, Rahuma and Emhemmed, 2020; Usherwood *et al.*, 2020; Cheney *et al.*, 2021; Harvey and Inman, 2021; Boughou *et al.*, 2022). The approach that is used affects the estimated aerodynamic efficiency (C_L/C_D, and therefore other aerodynamic characteristics) which can lead to different results, ultimately causing disagreement between efficiency estimates. Aerodynamic characteristics and efficiency estimates can be obtained by using numerical analyses, wind tunnel experimentation, or theoretical methods such as the sink speed method. The sink speed method makes use of the ratio between the horizontal airspeed and the vertical velocity (called the sink speed) to estimate the maximum lift-to-drag ratio (Harvey and Inman, 2021). From the three methods, wind tunnel experiments on live birds were considered the most reliable method of calculating avian efficiency whilst the sink speed method would require sink speed estimates to be accurate to within 0.01m/s to for reasonable results.

Computational fluid dynamics (CFD) uses numerical analysis to solve fluid flow fields and has been used to estimate the aerodynamic characteristics of avian wings (Omar, Rahuma and Emhemmed, 2020; Boughou *et al.*, 2022). Two-dimensional CFD analysis has been performed on eagle, stork, hawk and albatross airfoils by Omar, Rahuma and Emhemmed (2020). The origin of the airfoils used are unknown, and no clear evidence of how it was obtained is given. The study used an open source CFD code, and it was found that the chosen turbulence model could achieve agreement between the numerical modelling and experimental data by Selig and Guglielmo (1997). The aim of the study was to determine the aerodynamic efficiencies of avian airfoils in order to compare the performance thereof to a man-made Eppler 193 airfoil at between $\mathrm{Re} = 10^5$ and $\mathrm{Re} = 2.7 \times 10^5$. It was concluded that the Albatross airfoil had the highest aerodynamic efficiency at an angle of attack of 0°.

Pseudo two-dimensional (P2D) CFD analysis on an owl-like airfoil inspired by Liu et al. (2006) and Wagner et al. (2017) found that 2D Reynolds Averaged Navier-Stokes (RANS) can predict the unsteadiness of the aerodynamic coefficients when compared to 3D large eddy simulation (LES) results (Boughou *et al.*, 2022).

None of the studies mentioned above considers the fluid structure interaction of the airflow with the wing. Nachtigall and Wieser (1966) and Cheney et al. (2021) both showed that the airfoil of an avian wing morphs when comparing a wing with no airflow to a wing in the presence of airflow. In both these studies, it was found that the peak camber of an airfoil decreases with an increase in flight speed and angle of attack. Changing the camber would alter the shape of the airfoil and therefore, it would alter the aerodynamic load acting on the wing of the bird. Decreasing the camber would lead to a smaller aerodynamic body when viewed from the perspective of the air, essentially decreasing the produced (pressure) drag.

Aerodynamic characteristics of an avian wing has also been investigated using wind tunnel experiments. Henningsson and Hedenström (2011) used a live bird (Swift, Barn Owl, Tawny Owl and Goshawk) in a tilted wind tunnel (Usherwood et al., 2020). The maximum wingspan of the swift used was 0.392m, and that of the barn owl, tawny owl, and goshawk were 0.86m, 0.819m, and 1.066m, respectively, where the GHA wingspan was 2.18m (Alerstam et al., 1993). Capturing and attempting to train a GHA to fly in a tilted wind-tunnel, 2000km from its origin is not feasible.

An alternative possibility is to use a half span wing, prepared using taxidermy techniques. This has been done on glaucous-winged and western gulls and the maximum observed C_L/C_D was 5 (Harvey *et al.*, 2019). Comparing this to a full span gull wing of Lazos (2005) with $(C_L/C_D)_{\max} = 22°$ proves the discrepancies between different experimental set-ups. More comparisons between studies prove this discrepancy between different experimental cases. The maximum lift-to-drag ratio of a western jackdaw wing was 68% lower compared to the measurement taken on a live bird in a wind tunnel (Rosén and Hedenström, 2001; Lees et al., 2016). So far, only a single wing measurement demonstrated greater aerodynamic efficiency than the entire bird. A half-span common swift wing had a $(C_L/C_D)_{\max}$ of 17, which was 34% higher than the live wind tunnel measurement (Withers, 1981; Henningsson and Hedenström, 2011). Nevertheless, a separate study conducted on full-span common swift wings estimated a $(C_L/C_D)_{\max}$ of 10.4, indicating an 18% decrease compared to the live wind tunnel measurement (Lentink *et al.*, 2007; Henningsson and Hedenström, 2011). These inconsistencies might be attributed to wing preparation techniques or variations in experimental methodology. Van Oorschot et al. (2016) studied 13 species of falcon in a similar way and the highest lift-to-drag ratio obtained was similar to that of Harvey et al. (2019).

Finally, the sink speed method requires observing the horizontal and vertical velocity components of the bird in gliding flight in its natural habitat. The aerodynamic efficiency is then calculated as the ratio between the horizontal and vertical velocities when the glide angle is sufficiently small. All these velocity measurements require that the measurements are adjusted for the local wind conditions that the bird encounters. This theoretical method has been used by Pennycuick and Lighthill (1982) to estimate the maximum aerodynamic efficiency of the GHA and a lift-to-drag ratio of 22 was determined for the GHA.

1.3. Research Gap

A 3D geometrical model of the GHA (or birds of similar size and clade) does not exist to the best of the researcher's knowledge. There is also no evidence of the aerodynamic characteristics (C_L, C_D, and C_L/C_D, at different α) of the GHA. Furthermore, the process in which a mathematical model of an avian wing is obtained is outdated, using techniques predating 1943. Modern methods of quantifying airfoils exist, and these methods can be applied to avian airfoils. In addition, the passive morphing of a GHA wing when exposed to airflow has not been studied previously.

1.4. Research Objectives

This main aim of this research is to obtain the geometry of the GHA wing in the presence of airflow. A baseline static airfoil in a parameterized domain is required to obtain a passively morphed airfoil. This would enable the optimization of the airfoil to obtain a reasonable first estimate of the geometric and aerodynamic characteristics of the GHA wing. The following questions are investigated in this work:

- Can the quantification method of the geometry of avian wings be improved on and is there a novel way to do so which enables the creation of more accurate 3D models?

- Can a 3D model of the GHA wing be developed? Although this study is limited to P2D CFD, the development and availability of a 3D model would allow future researchers to do CFD analysis on a 3D GHA wing. Furthermore, the development of a 3D model could enable the manufacturing of a wing for use in wind tunnels to validate CFD methods or obtain further aerodynamic results.
- If a 3D model is developed using 3D scans of wings subject to zero velocity, how can the geometry of a wing subject to airflow be obtained? This is an obvious downfall of using 3D scans from static wings, and it is known that avian wings undergo geometrical changes due to fluid structure interaction (Nachtigall and Wieser, 1966; Ruck and Oertel, 2010; Deshpande and Modani, 2019), but quantified deformation results in the presence of airflow of an actual avian wing is yet to be studied.

Following the aerodynamic analyses of the developed GHA wing and airfoils, the specific quantitative questions to be answered are:

- What is the maximum aerodynamic efficiency of the GHA at the flight conditions in which it would normally operate?
- What is the lift and drag polars of a representative GHA airfoil?

The qualitative questions to be answered are:

- Can an aerodynamic optimization study aiming to maximize the aerodynamic efficiency of an avian wing estimate the morphed geometry of that wing when subject to airflow?

1.5. Scope of work

The study will not aim to resolve the geometry of the tip of the GHA wing. This is due to the thin nature of this region and the inaccuracy involved in extracting the geometry from this region.

This study will be limited to the use of CFD for flow analysis and will not include wind tunnel experiments. The CFD will be limited to P2D to speed up the simulation time whilst still obtaining results that can capture the 3D flow structures expected in low Reynolds number flows. P2D is used rather than 2D because of the chosen transition model which is not suited for 2D domains. 3D CFD is not used due to the added complexity of the wing geometry itself, and the further complication of the optimization process, which aims to obtain an in-flight configuration of the wing/airfoil. P2D therefore serves as the best trade-off between accuracy and complexity. Surface roughness, porosity, temperature effects, and the fluid structure interaction of the GHA wing will not be accounted for due to the increase in complexity. Finally, the aerodynamic effect of the body and tail will not be included.

1.6. Structure of the dissertation

Section 2 summarizes relevant literature. The GHA geometry and the flight dynamics of birds are discussed. This is followed by an introduction on the chosen airfoil parameterization method. The aerodynamics of the expected flow in which GHA operate are introduced and the numerical modelling thereof is investigated. This section ends with a discussion on the aerodynamic optimization of aerodynamic bodies.

Section 3 starts with the validation of the PARSEC method as a suitable method to quantify airfoils which exhibit outliers. Since the scanned GHA wing will exhibit outliers, it is necessary to test whether the PARSEC method can replicate airfoils that contain outliers. Afterwards the process which enables the conversion of a point cloud to a 3D model of the GHA wing is presented.

Section 4 verifies and validates the CFD approach to be used in the rest of the study. This is done using Richardson extrapolation to ensure that the solution is independent of the computational grid used (ASME, 2008). Next, it is compared to a well-known previously documented study which will contain similar flow fields and flow phenomena. A meshing strategy is developed which will be able to automatically adapt to any airfoil generated using the PARSEC method. Results obtained using this meshing strategy for a new airfoil can be compared to documented results of the same airfoil to validate the new meshing strategy.

Section 5 shows the setup of a parametric model of the GHA airfoil which will enable automatic geometry updating during the optimization study. The baseline case of the arm airfoil is quantified using CFD. An optimization study is performed on the parametric model of the GHA arm airfoil and the geometric and aerodynamic results are presented and discussed in comparison to the baseline case.

Section 6 concludes the dissertation and makes recommendations for future research in the field of the geometry of avian wings and its aerodynamic characteristics.

.

2. Literature Review

2.1. The Grey-headed Albatross

The physical properties of the Grey-headed Albatross (GHA) are summarized in Table 1.

Table 1: A summary of the physical properties of the Grey-headed Albatross

	Catry et al. (2004)	Brooke (2004)	Alerstam et al. (1993)
Mass (kg)	3.05	2.7-4.4 (mean = 3.7)	3.79
Wingspan (m)		2.2	2.18
Aspect Ratio			13.5
Ground speed (m/s)			11.0-15.5 (mean = 13.2, sd = 1.5)
Air speed (m/s)			11.3-15.1 (mean = 13.0, sd = 1.2)

The anatomy of a bird wing, shown in Figure 1, is similar to of other four-limbed animals. The main skeletal features are the humerus which attaches to the shoulder inside the body of the bird, and the radius and ulna. These three bones are what is referred to as the arm section, shown in Figure 1a. When thin slices of the arm are "removed", it has resembling features of airfoils. The next section is the hand section which consists of the manus. The hand section has 10 primary feathers (remiges), and the arm section can have in the region of 20 secondary feathers. From Figure 1b the airfoil sections can be seen to change in the spanwise direction. Going from the root to the tip, the chord length changes, and the thickness and camber decrease (changing the thickness to chord length ratio and camber to chord length ratio). The profile at the tip of the wing is seen to be made up of just a few feathers (König *et al.*, 2016).

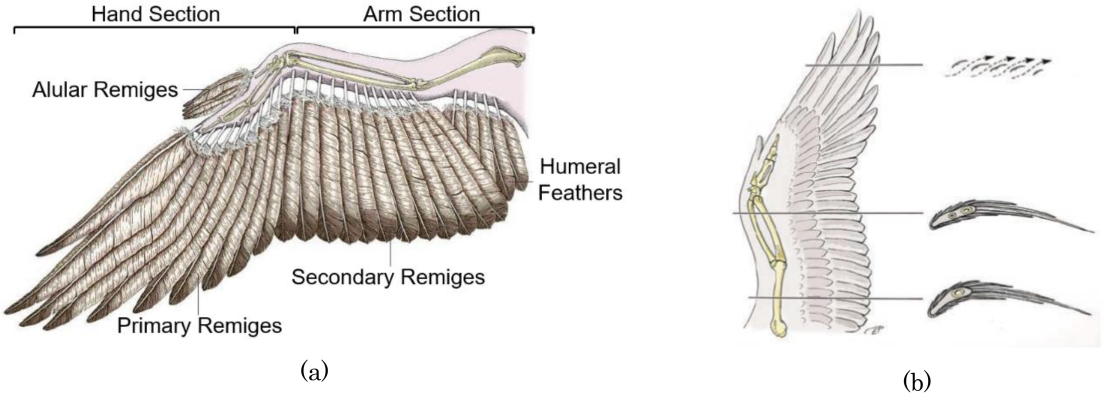

(a)

(b)

Figure 1: The anatomy of an avian wing (König et al., 2016).

2.2. Previous work on avian wing geometries.

Liu et al. (2006) reconstructed 3D models of avian wings (seagull, merganser, teal and owl) using 3D scanning and obtaining a point cloud of each wing. The point cloud was then sliced into 2D sections at various spanwise locations to form airfoils consisting of many randomly ordered points. The data points that form the 2D airfoils were noisy and had to be postprocessed to recreate an avian wing. Each airfoil was then rotated, translated, and transformed such that the local airfoil's leading edge was located at a (x, z) location of (0,0) and the trailing edge was located at (1,0) so that the angle between the leading and trailing edge is exactly 0°, i.e., horizontal chord and the chord length is 1, as shown in Figure 2.

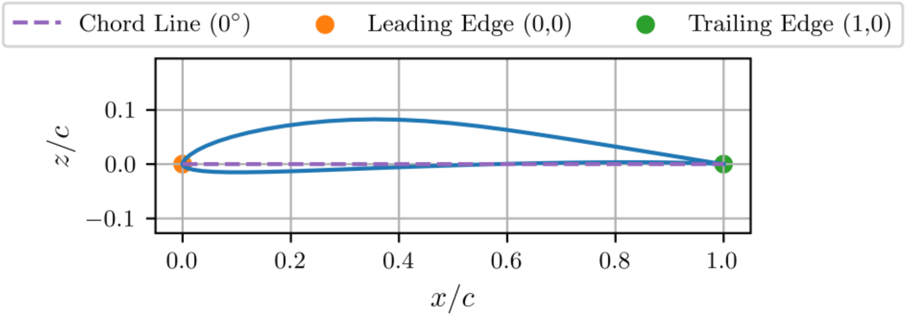

Figure 2: Eppler 387 (E387) airfoil used as an example to illustrate the requirements of a postprocessed airfoil.

Next, each airfoil's camber line was determined by using a three-term approximation (Helmbold and Keune, 1943) of the Birnbaum-Glauert camber line equation (Mair, 1961) shown in equation (1), for which the coefficients, S_n were solved using a least squares approach,

$$\frac{z_c}{c} = \frac{z_{c,\max}}{c} \eta(1-\eta) \sum_{n=1}^{3} S_n (2\eta - 1)^{n-1} \tag{1}$$

where $\eta = x/c$ is the normalized chordwise coordinate and $z_{c,\max}$ is the maximum camber coordinate and c is the local wing chord. The thickness distribution was then calculated using a four-term approximation of the Birnbaum-Glauert thickness (Mair, 1961) shown in equation (2),

$$\frac{z_t}{c} = \frac{z_{t,\max}}{c} \sum_{n=1}^{4} A_n \left(\eta^{n+1} - \sqrt{\eta}\right) \tag{2}$$

where $z_{t,\max}$ is the maximum thickness coordinate so that the maximum thickness is $2z_{c,\max}$. The constants, A_n, were then solved using a least squares approach. The upper and lower surfaces of an individual airfoil was then expressed as the addition and subtraction of the camber line with the thickness as shown in equations (3a) and (3b) respectively.

$$z_{\text{upper}} = z_c + z_t \tag{3a}$$

$$z_{\text{lower}} = z_c - z_t \tag{3b}$$

The airfoil slices for which the camber and thickness distributions were calculated were joined using information about the change in twist as a function of the wingspan. An example of the reconstructed seagull wing can be seen in Figure 3a.

The same method was followed by Klän et al. (2009), and it was reported that this approach resulted in non-realistic configurations when applied to owl wings due to varying coefficients of S_n and A_n along the span of the wing. This caused discontinuous changes in the geometry of the wing in the spanwise direction. Furthermore, discrepancies of the maximum camber and maximum thickness of adjacent airfoils were very high. This meant that a reconstructed wing would not have a smooth profile in the spanwise direction. It was solved by using a least square fit on the coefficients for the camber line, S_n, and thickness distribution, A_n, in the spanwise direction which yielded a smooth wing surface. An example of the reconstructed wing can be seen in Figure 3b.

Carruthers et al. (2010) used a different method, for which no documentation is supplied. In their method, a spatially averaged surface was constructed using polynomial regression techniques to fit a smooth surface through as few as 252 points and doing so only for the arm section of the wing. The curved leading edge and trailing edge sections (planform) was approximated using a quadratic polynomial. The surface and planform curves were then used to model the z coordinate of all the points. A reconstructed wing using this method can be seen in Figure 3c.

Waldrop et al. (2020) and Rader et al. (2020) used principal component analysis (PCA) to align a 3D point cloud in an (x, y, z) 3D space. From this, the spanwise length of the wing was calculated. The point cloud was then sectioned into airfoils similar to Liu et al. (2006) and Klän et al. (2009). Following this, the only metrics extracted was the chord length $(x_{\max} - x_{\min})$ and the maximum section thickness $(z_{\max} - z_{\min})$. These values were then used, and the already existing wandering albatross airfoil (Ananda and Selig, 2018), was rescaled to match the chord length and thickness of the scanned wing. The albatross airfoil used is however not mentioned in Ananda and Selig (2018) but the airfoil shapes are said to be “bird-like”. The scaling process was then done to the remaining airfoils in the spanwise direction. The reconstructed wing is shown in Figure 3d. This study was not necessarily an aerodynamic investigation into bird wings but rather a morphological study containing 126 bird types.

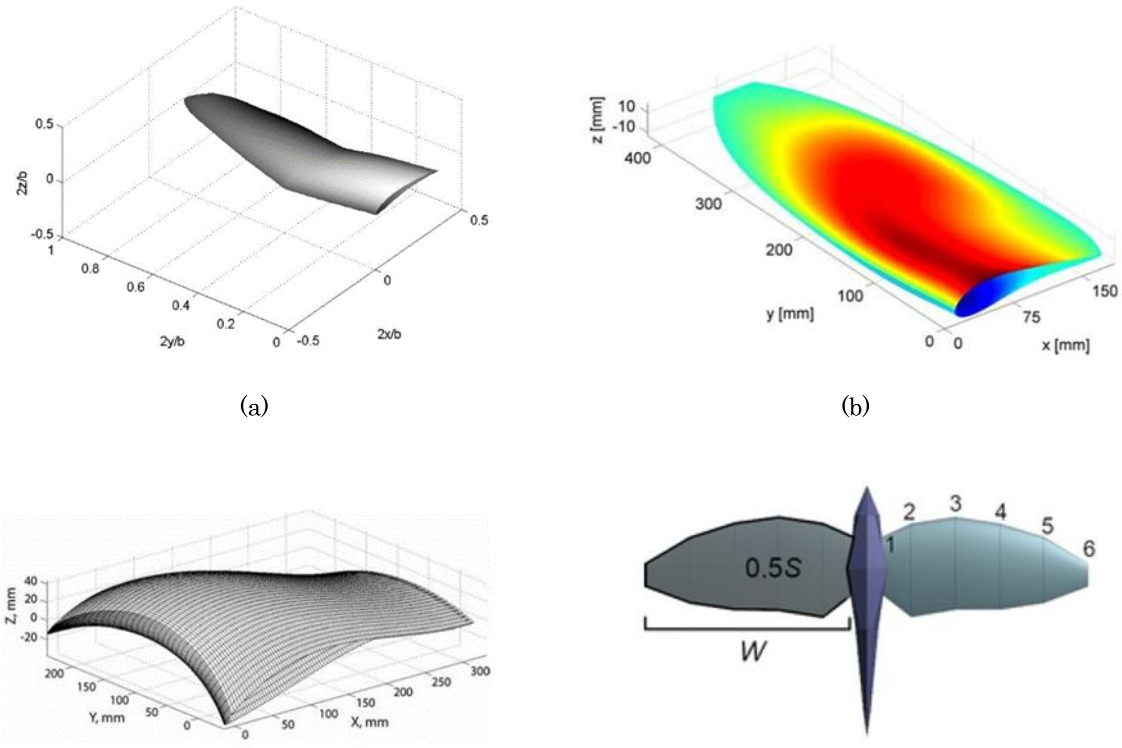

(a) (b)

(c) (d)

Figure 3: (a) Seagull wing reconstructed by Liu et al. (2006) (b) Owl wing reconstructed by Klän et al. (2009) (c) Steppe eagle wing reconstructed by Carruthers et al. (2010) (d) Unknown wing reconstructed by Waldrop et al. (2020) and Rader et al. (2020).

2.3. Flight performance measurements of avian wings

2.3.1. Biological and observed evidence

Gliding and soaring are highly effective modes of transport for birds, and it requires less energy than flapping flight. Baudinette and Schmidt-Nielsen (1974) investigated oxygen consumption of birds in wind tunnels. The oxygen consumption of birds tended to increase when birds required flapping flight when compared to gliding flight. The metabolic rate of a laughing gull during gliding flight and at rest were found to be equivalent (Tucker, 1972).

Sakamoto et al. (2013) and Duriez et al. (2014) investigated the heart rates of black-browed albatrosses and griffon vultures respectively. It was found that heart rates would increase during the take-off and landing phases of flight. After a certain period of gliding flight, heart rates would return to baseline levels. The former showed that flapping flight only contributes to 4.6% of the time flying for the black-browed albatross and only accounted for 13.3% of the total energy use during cruising flight. The authors’ conclusion was that albatrosses achieve energy efficient flight by greatly reducing the time spent flapping.

Albatrosses have been shown to soar for thousands of kilometres exchanging energy from the velocity gradient above the ocean for potential energy, known as dynamic soaring (Richardson, 2011; Sachs *et al.*, 2012).

2.3.2. Experimental estimations of avian flight efficiencies

The aerodynamic efficiencies of gliding birds have been studied to compare it to those of man-made unmanned aerial vehicles (UAVs), with many sources using bird wings as inspiration for efficient UAVs (Withers, 1981, Pennycuick and Lighthill, 1982; Lazos, 2005; Henningsson and Hedenström, 2011; van Oorschot et al., 2016; Harvey et al., 2019; Usherwood et al., 2020; Harvey and Inman, 2021).

Withers (1981) investigated the aerodynamic characteristics of bird wings at Reynolds numbers of 1.5×10^4. Morphological features like aspect ratio, camber, nose radius, and position of maximum thickness were included. The disparities in aerodynamic properties among bird, insect, and airplane wings was primarily attributed to their varying Reynolds numbers. Bird wings, which operate at lower Reynolds numbers compared to aerofoils, exhibit higher minimum drag coefficients (0.03-0.13), lower maximum lift coefficients (0.8-1.2), and lower maximum lift-to-drag ratios (3-17). There was a clear trade-off between lift and drag performance. Wings with low drag generally had lower maximum lift coefficients, while those with high maximum lift coefficients tended to have higher drag coefficients. The flow pattern over bird wings, as observed through pressure-distribution data, aligned with aerodynamic theory for airplane wings at low Reynolds numbers, corroborating the observed lift and drag coefficients. The highest performing bird in this study was the swift with $(C_L/C_D)_{\max} = 17$.

Lazos (2005) studied biologically inspired fixed-wing configurations. In this research it was stated that natural flyers were expected to have been optimized to provide enhanced efficiency. He investigated 4 different wing configurations using an SD7032 airfoil in a series of wind tunnel tests. Results showed two of the biologically inspired wings, one based on a combination of a shark pectoral and dorsal fin and the other, based on a seagull in a high-speed glide exhibit maximum lift-to-drag ratios of 22.43 and 19.88, respectively.

A review by Harvey and Inman (2021) on the aerodynamic efficiency of gliding birds highlighted the differences in efficiency estimation of gliding birds. In the review, theoretical and experimental methods were compared. It was concluded that the efficiency estimates which use the sinking speed, U_s, of gliding birds need to be accurate to the order of 0.01ms^{-1}, which is difficult to achieve. The maximum efficiency (or glide ratio) of the

GHA was estimated by Pennycuick and Lighthill (1982) as 22 using the sink speed method mentioned earlier and the speed at which this was achieved was 14ms^{-1}.

Efficiency estimations using live birds in controlled environments deliver the most reliable minimum estimate of avian gliding efficiency but is highlighted as a difficult task. Henningsson and Hedenström (2011) used particle image velocimetry (PIV) to sample the wake of a gliding common swift in a tilted wind tunnel. The maximum reported lift-to-drag ratio was ± 12. Strong emphasis was placed on the aerodynamic effect of the tail of the bird. This was also studied on a gliding barn owl, tawny owl and goshawk, reporting coefficient of lift (C_L) values of 0.69, 1.06, 1.01 respectively. These values were also computed using PIV (Usherwood *et al.*, 2020).

Another method of estimating the efficiency of bird wings is to use prepared specimens. Prepared specimens include full birds or half span wings prepared by taxidermy techniques or manufactured replicas. Using these kinds of specimens allow for direct force measurement in wind tunnels whilst eliminating behavioural considerations. Knowing that birds are active gliders, these test specimens may not accurately replicate the bird's true gliding posture (Harvey and Inman, 2021).

Harvey et al. (2019) extensively investigated the aerodynamic pitch stability and aerodynamic performance of different wing configurations due to different skeletal positions in two distinct types of gulls. Single cadaver wings were placed in wind tunnels and were tested at Reynolds numbers between 9.2×10^4 and 1.79×10^5. Testing included pitch angles between $-50°$ and $50°$ and aerodynamic forces were measured. For the different wing configurations, the highest lift-to-drag ratio was found to be ± 5.

Van Oorschot et al., (2016) performed similar wind tunnel tests on single wings of 13 species of falcon. The average lift-to-drag ratio for an extended wing glide and swept wing glide was the highest at ± 4.5 when compared to those for extended and swept flapping. Maximum C_L values for the four different configurations were in the angle of attack range of $17.5°$ to $45°$.

2.4. Relevant aerodynamic considerations

The Reynolds number of the flow over a wing gives a quantification of the ratio between the inertial forces to the viscous forces. The Reynolds number is a dimensionless quantity used to categorize fluid flow and is given as,

$$\mathrm{Re} = \frac{\rho V l}{\mu} \tag{4}$$

where ρ is the density of the freestream air, V is the freestream velocity, l is a characteristic length (chord length, c, when applicable to wings) and μ is the dynamic viscosity of the fluid.

The following descriptions of the force coefficients are used in this work:

$$C_L = \frac{L}{\frac{1}{2}\rho V^2 S} \tag{5}$$

and

$$C_D = \frac{D}{\frac{1}{2}\rho V^2 S} \tag{6}$$

where L and D are the lift and drag forces respectively, ρ is the freestream density, and S is the projected area of the wing onto a horizontal plane. The coefficient of pressure is calculated as,

$$C_P = \frac{P - P_\infty}{\frac{1}{2}\rho V^2} \tag{7}$$

where P and P_∞ denote the local pressure on the wing/airfoil and the freestream pressure respectively. This dimensionless quantity gives an indication of the pressure distribution and gradients on the surface of the wing. The skin friction coefficient is given as,

$$C_F = \frac{\tau_w}{\frac{1}{2}\rho V^2} \tag{8}$$

where τ is the wall shear stress on the surface of the wing. The skin friction coefficient gives an indication on regions on the wing/airfoil which might experience separation and reverse flow.

Gliding albatross have been shown to operate at Reynolds numbers of 2×10^5 (Harvey and Inman, 2021). The Reynolds number given above will further in the text be referred to low Reynolds numbers. Low Reynolds number flows over wings are difficult to model and measure using experimental or numerical methods and results are sensitive to geometry, environment, and numerical modelling techniques (Tank et al., 2017). This is partly because low Reynolds numbers typically introduce flow features which are not present at fully developed turbulent flow.

Batill and Mueller (1980) experimentally showed that at low Reynolds numbers, laminar separation bubbles (LSB), shown in Figure 4, might occur which could introduce non-symmetric C_L. The formation of a laminar separation bubble is caused by the boundary layer over the suction surface of the airfoil that remains laminar into the adverse pressure gradient region. The laminar boundary layer cannot develop through the adverse pressure gradient and would cause the boundary layer to separate from the surface of the airfoil. This causes an increase in drag and a decrease in lift which leads to a sudden decrease in C_L/C_D. If the separation location is early enough, the separated boundary layer could transition to a turbulent state and reattach to the airfoil surface due to increased mixing and momentum transfer from the outer flow toward the airfoil. When this reattachment takes place, a recirculating region called a LSB forms.

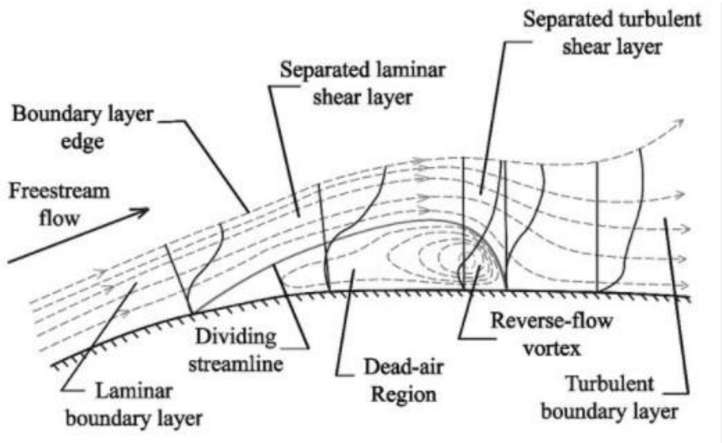

Figure 4: 2D Laminar Separation Bubble formation (Horton, 1968).

2.5. Numerical modelling of low Reynolds number flow over airfoils

The shear stress transport (SST) $k - \omega$ turbulence model is commonly used for low Reynolds number flows in which separation and LSBs are expected (Babajee and Arts, 2013; Choudhry et al., 2015; Collison et al., 2017; Carreño Ruiz and D'Ambrosio, 2022). The specific SST $k - \omega$ transition model used is the $\gamma - \mathrm{Re}_\theta$ model, developed by Menter et al. (2006) and Langtry et al. (2006). This transition model is specifically formulated for unstructured CFD codes and provides an approach to predict the onset of transition in a turbulent boundary layer.

Most recently, Carreño Ruiz and D'Ambrosio (2022) investigated the $\gamma - \mathrm{Re}_\theta$ transition model for airfoils operating in the low Reynolds number regime. The model was validated against existing experimental data and high fidelity CFD simulations using direct numerical simulation (DNS) and LES. A parabolic domain extending 1000 chord lengths to the outlet were used with a polyhedral mesh which sped up simulation convergence because information spreading was enhanced due to more neighbouring cells when compared to quadrilateral or triangular grids. Two-dimensional CFD was performed on three low Reynolds number airfoils (E387, SD7003, and Ishii at $\mathrm{Re} = 2.3 \times 10^4$ to $\mathrm{Re} = 2 \times 10^5$), comparing the aerodynamic coefficients of lift and drag and separation bubble lengths with experimental and numerical results available in the literature.

For this transition model, a y^+ value of less than 1 is required to properly resolve the wall region according to Langtry et al. (2006). This study concluded that the $\gamma - \mathrm{Re}_\theta$ transition model reproduced the transition behaviour in 2D airfoils. It was further found that the lift and drag coefficients compared to experimental data increased with an increase in Reynolds number, but prematurely predicted stall. There were also limitations regarding 2D simulations when comparing polars of the E387 airfoil to existing data, which showed that flow around the airfoil had 3D structures and that it affected the pressure distribution on the body. These types of structures could not be reproduced by 2D domains.

Chen et al. (2020) investigated the aerodynamic performance and transition prediction using the $k - \omega$ turbulence model using the $\gamma - \mathrm{Re}_\theta$ transition model and concluded that CFD results using this method predicted lift within 1% and drag within 3% of experimental results on a FX 63-137 airfoil at $\mathrm{Re} = 2 \times 10^5$. This was compared to the Spalart-Almaras (S-A) turbulence model which was found to overpredict the drag by 34%. The domain used was 2D and extended 40 chord lengths upstream and 60 chord lengths downstream. Again, it is noted that a $y^+ < 1$ was crucial in seeking results that correctly predict the transition and aerodynamic coefficients. Results showed oscillatory behaviour in the lift and drag coefficients as the simulation progressed. Oscillations in these coefficients were seen to be higher in magnitude as the angle of attack increased.

Counsil and Goni Boulama (2012) validated the use of unsteady RANS (URANS) in conjunction with the $k - \omega$ turbulence model using the $\gamma - \mathrm{Re}_\theta$ transition model over a pseudo 2D NACA0012 airfoil. The mesh used was bullet shaped, extending 20 chord lengths to the outlet and using a 20 chord length inlet radius. Results were compared to DNS results from Shan et al. (2005) and it was found that instantaneous and mean flow features were satisfactorily similar.

Choudhry et al. (2015) performed 2D CFD on a thick, symmetric NACA0021 airfoil at $\mathrm{Re} = 1.2 \times 10^5$ to investigate the effects of long separation bubbles. An O-type mesh with the airfoil in the centre using a radius of 20 chord lengths was used. The quadrilateral mesh made use of 30 boundary layer (prism layer) cells, and it was ensured that $y^+ \leq 1$. It was found the $\gamma - \mathrm{Re}_\theta$ model underpredicted the lift and drag coefficients when compared to experimental results by Hansen et al. (2011) at the same Reynolds number. The study compared the $\gamma - \mathrm{Re}_\theta$ model to the laminar kinetic energy ($k - k_\mathrm{L} - \omega$) model (Walters and Cokljat, 2008), which is not available in STAR-CCM+ and showed that the latter was better suited to thick airfoils which exhibited long separation bubbles.

Collison et al. (2017) investigated the E387 airfoil in 2D and P2D using the $\gamma - \mathrm{Re}_\theta$ transition model at $\mathrm{Re} = 2 \times 10^5$. The results were compared to existing experimental data (McGhee and Walker, 1989) and the laminar separation and turbulent reattachment locations were predicted within 4% and 6%. The domains were bullet shaped, using an inlet radius and outlet length of 5 chord lengths. Thirty and fifty prism layers were used for the 2D and P2D simulations, respectively. The P2D simulations used 220 nodes on the airfoil.

To reasonably resolve fluid domains at low Reynolds numbers, there are some key considerations based on the literature to consider:

- Domain shape of the computational mesh: The bullet shaped mesh is commonly used.
- Two- or three-dimensional models: P2D analyses (or 3D analyses) is often required since the flow exhibits 3D structures in low Reynolds number cases.
- Selection of the turbulence and transition models: The $k - \omega$ turbulence model paired with the $\gamma - \mathrm{Re}_\theta$ transition model is commonly used.
- Steady or unsteady solvers: Steady RANS solvers can lead to oscillatory results compared to stable results when using URANS. Time averaged oscillatory results can relate to unsteady results without the time penalty of resolving a full unsteady simulation.

2.6. Automated mesh refinement in CFD.

In the current research, it is expected that many different airfoil geometries will be generated in the CFD. Automated adaptive meshing is used to simplify the application of different meshes for different geometries. The commercial CFD software used in this research (Siemens Simcenter STAR-CCM+) allows for automation of mesh refinement, but the criteria which decides whether cells are to be refined or coarsened is programmed by the user. This important choice is highly dependent on the type of flow expected.

Carreño Ruiz and D'Ambrosio (2022) used adaptive mesh refinement based on a linear combination of the magnitudes of the pressure and velocity gradients on a logarithmic scale. The weights of the linear combinations were dependent on the type of flow and the Reynolds number. Therefore, the weights of the linear combination and the lower and upper thresholds had to be manually tuned to get results that were sufficient.

Michal et al. (2020) compared different adaptive mesh criteria using different flow adaptive mesh refinement methods on a multi-element airfoil at $\mathrm{Re} = 5 \times 10^6$. One of the methods used a weighted combination of the first and second spatial derivatives of the Mach number (which is related to the velocity magnitude). The second method that was used controlled the L^2-norm of a chosen scalar field developed by Loseille et al. (2007). This method was based on the multiplication of a Hessian of a scalar field and the determinant of the same Hessian. The Hessian, which is a square matrix of second order spatial derivatives, quantifies the curvature of a scalar field. The L^2-norm, therefore, gives the magnitude of the second order derivatives of a scalar field at a certain location. This method, again, made use of the Mach number as the scalar field. From this work it is noted that the scalar fields used in both applications can be changed to be any scalar field and it is not limited to the use of only the Mach number.

Wackers et al. (2017) used a criterion based on the square root of the absolute value (L^2-norm) of the pressure field multiplied by the cell size, squared. The investigation was extended to compare this criterion to one which uses the maximum of 4 flow variables (pressure and the three components of velocity). Results showed little refinement when only using the pressure-based refinement criteria. The refinement criteria making use of the 4 flow variables, however, showed good refinement in the wake regions.

The STAR-CCM+ documentation (Siemens Digital Industries Software, 2022a) proposes a method for smoothly varying scalar field solutions, such as for applications in aerodynamics, to make use of the Laplacian of a representative solution variable.

From the literature above, two strategies were used. The difference being the usage of either first derivatives or second derivatives. First derivative adaption criteria were used by Carreño Ruiz and D'Ambrosio (2022) and Michal et al. (2020) (the first criteria mentioned in their research). The scalars used were either velocity based only or a combination of velocity and pressure, giving the idea of total pressure.

Second derivative criteria such as the L^2-norm of a Hessian matrix of a scalar variable is the same as the Laplacian of a scalar variable. The Laplacian of the total pressure mentioned in the STAR-CCM+ user guide is similar to the method introduced by Carreño Ruiz and D'Ambrosio (2022), using both velocity and pressure gradients, except that the former uses a first derivative approach. The second method in the research of Michal et al. (2020) and developed by Loseille et al. (2007) is a second derivative method based on the Mach number, but it can be substituted for any flow field variable. Wackers et al. (2017) also used a second derivative approach but did so independently between 4 flow variables. The Laplacian captures both first and second derivative effects, and the total pressure captures the pressure and velocity fields. Therefore, this will be the choice for the refinement criteria going forward.

2.7. Aerodynamic optimization of parameterized wings to capture dynamic morphing of wings

An avian wing subject to airflow undergoes deformation due to fluid structure interaction which may lead to changes in the associated aerodynamic forces (Nachtigall and Wieser, 1966; Ruck and Oertel, 2010; Deshpande and Modani, 2019). If the geometry used in the CFD analysis is obtained from a wing scan subject to zero velocity, the expected passive morphing taking place in a live bird will not be captured.

It is hypothesized that the geometry of the wing will morph to a shape that maximizes the aerodynamic efficiency, C_L/C_D. Norberg (1990, 2006) indicated that birds aim to maximize their lift and minimize their drag, so in a sense, maximizing their lift to drag ratio. Van Oorschot et al. (2016) states that "wing morphing appears to be ubiquitous among flying birds, and it is generally hypothesized that such morphing optimizes aerodynamic performance". The estimation of the geometry of an avian wing in the presence of airflow can therefore be seen as an optimization problem. Starting from a baseline case (no airflow) and allowing the parameters which define the airfoil geometry to be changed to achieve the highest aerodynamic efficiency could therefore deliver the geometry of a GHA airfoil in flight or at least a realistic estimation thereof.

Two optimization methods are available in STAR-CCM+. The first is adjoint optimization and the second, a multiple search strategy optimizer using the SHERPA algorithm (defined below). With the adjoint method, the objective function is a function of the flow field variables, w, and the physical shape of the discretized domain, S. The optimization yields a sensitivity, δS, which transforms the shape of the discretized domain to minimize or maximize the objective function. Note that minimizing the objective function, posed as $f(x)$ is the same as maximizing an objective function posed as $-f(x)$. The disadvantage of the adjoint method is the fact that it is not compatible with large geometrical changes. Since large geometrical changes are expected when an avian airfoil is subject to airflow, this method will not be used.

The SHERPA (Simultaneous Hybrid Exploration that is Robust, Progressive, and Adaptive) algorithm, employs multiple search strategies at once and adapts to the problem as it "learns" about the design space. The advantages of the SHERPA algorithm are that the number of different search methods used can range between 2 and 10 at once. Traditional optimization algorithms require that tuning parameters (not to be confused with the design parameters) be chosen manually. SHERPA modifies these tuning parameters automatically as it learns more about the design space and better chooses the extent to which the different search methods are used (Siemens Digital Industries Software, 2022b).

Beneke (2018) used the SHERPA algorithm in STAR-CCM+ to optimize the nose and tail geometry of a high-speed train for drag minimization and crosswind stability. In this work the Ahmed body is optimized to minimize the drag and it served as a benchmark since the optimized inclination angle of the body is known to be a certain angle. The range of angles that could be used varied from 1° to 35° and the known optimal angle of 9° could be found using the SHERPA algorithm within 2.5% and 18.7% using the Reynolds stress turbulence model and the $k - \omega$ turbulence model respectively. As few as 40 designs were completed using each turbulence model.

3. The Geometry of the Grey-headed Albatross

Converting an airfoil from a list of coordinates in x and z (which consists of hundreds of points) to a domain which uses but a few parameters need to be investigated. The reason for introducing an airfoil parameterization method is twofold. The first reason for doing this is to smooth the noisy airfoils that are obtained using 3D scanning (see Figure 7). The second reason is to produce an airfoil that is optimizable. Recalling the goal of this research, which is to obtain an in-flight geometry of a GHA airfoil, a parameterized version of the airfoil can be optimized.

3.1. Proposing a new airfoil parameterization method for avian wings.

The PARSEC parameterization method (Sobieczky, 1997, 1999) shown in Figure 5 and described in Table 2 is a well-established parameterization method which has not been applied to the investigation of avian airfoils.

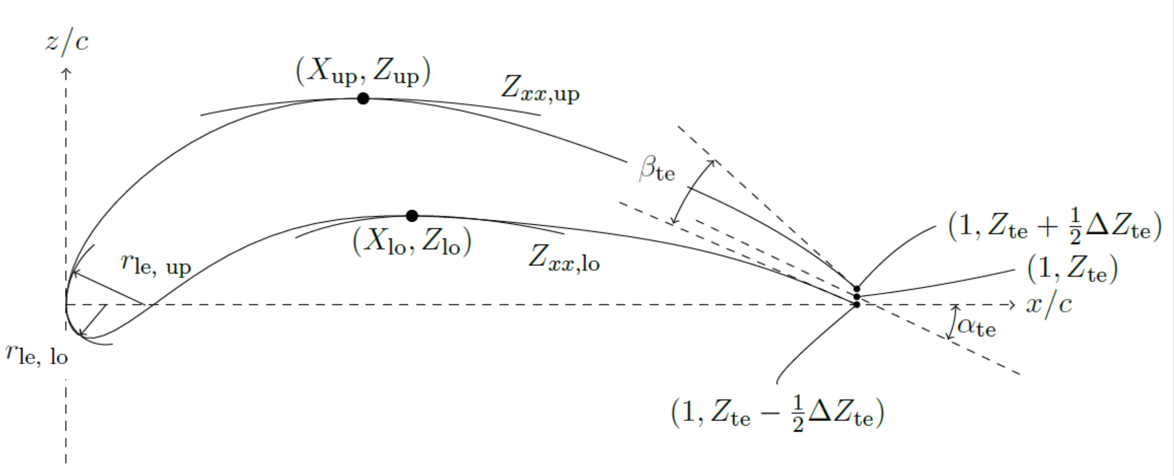

Figure 5: An airfoil showing the 12 PARSEC parameters and their geometrical meaning [Reproduced from Sobieczky (1997, 1999)].

Table 2: The 12 PARSEC Parameters

Parameter	Definition
$r_{\text{le, lo}}$	Lower leading edge radius
$r_{\text{le, up}}$	Upper leading edge radius
X_{lo}	Lower crest horizontal coordinate
X_{up}	Upper crest horizontal coordinate
Z_{lo}	Lower crest vertical coordinate
Z_{up}	Upper crest vertical coordinate
$Z_{\text{xx, lo}}$	Lower crest curvature (second derivative)
$Z_{\text{xx, up}}$	Upper crest curvature (second derivative)
α_{te}	Trailing edge direction
β_{te}	Trailing edge wedge angle
Z_{te}	Trailing edge vertical offset
ΔZ_{te}	Trailing edge thickness

The parameterization method makes use of 12 parameters and effectively controls the important aerodynamic and geometric features of an airfoil instead of arbitrary coefficients like that obtained by the Birnbaum-Glauert airfoils. The benefit in using the PARSEC method is the ability to have non-zero trailing edge thicknesses and non-zero trailing edge vertical offsets, which are not possible using the Birnbaum-Glauert airfoils.

The PARSEC method described is slightly modified to allow different upper and lower leading edge radii, similar to that done by Hájek (2011), Arias-Montano et al. (2012), Jung et al. (2016) and Akram and Kim (2021). This is later proven to be essential when considering airfoils with sharp leading edges. The PARSEC method is a widely used and more flexible approach towards developing airfoil profiles (Akram and Kim, 2021; Raul and Leifsson, 2021) compared to the Birnbaum-Glauert approach.

Using the 12 parameters shown in Figure 5 and Table 2 ,the coefficients, a_n and b_n where $n = 1,2, \dots ,6$ is solved from the following two equations.

$$\begin{bmatrix} 1 & 1 & 1 & 1 & 1 & 1 \\ X_{\mathrm{up}}^{1/2} & X_{\mathrm{up}}^{3/2} & X_{\mathrm{up}}^{5/2} & X_{\mathrm{up}}^{7/2} & X_{\mathrm{up}}^{9/2} & X_{\mathrm{up}}^{11/2} \\ 1/2 & 3/2 & 5/2 & 7/2 & 9/2 & 11/2 \\ \frac{1}{2}X_{\mathrm{up}}^{-1/2} & \frac{3}{2}X_{\mathrm{up}}^{1/2} & \frac{5}{2}X_{\mathrm{up}}^{3/2} & \frac{7}{2}X_{\mathrm{up}}^{5/2} & \frac{9}{2}X_{\mathrm{up}}^{7/2} & \frac{11}{2}X_{\mathrm{up}}^{9/2} \\ \frac{-1}{4}X_{\mathrm{up}}^{-3/2} & \frac{3}{4}X_{\mathrm{up}}^{-1/2} & \frac{15}{4}X_{\mathrm{up}}^{1/2} & \frac{35}{4}X_{\mathrm{up}}^{3/2} & \frac{63}{4}X_{\mathrm{up}}^{5/2} & \frac{99}{4}X_{\mathrm{up}}^{7/2} \\ 1 & 0 & 0 & 0 & 0 & 0 \end{bmatrix} \begin{bmatrix} a_1 \\ a_2 \\ a_3 \\ a_4 \\ a_5 \\ a_6 \end{bmatrix} = \begin{bmatrix} Z_{\mathrm{te}} + \frac{1}{2}\Delta Z_{\mathrm{te}} \\ Z_{\mathrm{up}} \\ \tan\left(\frac{2\alpha_{\mathrm{te}} - \beta_{\mathrm{te}}}{2}\right) \\ 0 \\ Z_{\mathrm{xx,\ up}} \\ \sqrt{r_{\mathrm{le,\ up}}} \end{bmatrix} \tag{9}$$

$$\begin{bmatrix} 1 & 1 & 1 & 1 & 1 & 1 \\ X_{\mathrm{lo}}^{1/2} & X_{\mathrm{lo}}^{3/2} & X_{\mathrm{lo}}^{5/2} & X_{\mathrm{lo}}^{7/2} & X_{\mathrm{lo}}^{9/2} & X_{\mathrm{lo}}^{11/2} \\ 1/2 & 3/2 & 5/2 & 7/2 & 9/2 & 11/2 \\ \frac{1}{2}X_{\mathrm{lo}}^{-1/2} & \frac{3}{2}X_{\mathrm{lo}}^{1/2} & \frac{5}{2}X_{\mathrm{lo}}^{3/2} & \frac{7}{2}X_{\mathrm{lo}}^{5/2} & \frac{9}{2}X_{\mathrm{lo}}^{7/2} & \frac{11}{2}X_{\mathrm{lo}}^{9/2} \\ \frac{-1}{4}X_{\mathrm{lo}}^{-3/2} & \frac{3}{4}X_{\mathrm{lo}}^{-1/2} & \frac{15}{4}X_{\mathrm{lo}}^{1/2} & \frac{35}{4}X_{\mathrm{lo}}^{3/2} & \frac{63}{4}X_{\mathrm{lo}}^{5/2} & \frac{99}{4}X_{\mathrm{lo}}^{7/2} \\ 1 & 0 & 0 & 0 & 0 & 0 \end{bmatrix} \begin{bmatrix} b_1 \\ b_2 \\ b_3 \\ b_4 \\ b_5 \\ b_6 \end{bmatrix} = \begin{bmatrix} Z_{\mathrm{te}} - \frac{1}{2}\Delta Z_{\mathrm{te}} \\ Z_{\mathrm{lo}} \\ \tan\left(\frac{2\alpha_{\mathrm{te}} + \beta_{\mathrm{te}}}{2}\right) \\ 0 \\ Z_{\mathrm{xx,\ lo}} \\ -\sqrt{r_{\mathrm{le,\ lo}}} \end{bmatrix} \tag{10}$$

With the 12 coefficients (a_n and b_n) known, the upper and lower surfaces are calculated given a horizontal distribution x which is a set of points between 0 and 1 using equations (11) and (12).

$$Z_{\text{upper}} = \sum_{n=1}^{6} a_n \, x^{n-\frac{1}{2}} \tag{11}$$

$$Z_{\text{lower}} = \sum_{n=1}^{6} b_n \, x^{n-\frac{1}{2}} \tag{12}$$

Classically, the PARSEC method starts with 12 parameters and yields an airfoil. In this study, the airfoil is known, and the PARSEC parameters are extracted, essentially reversing the order in which it is commonly used.

3.2. Validation of the PARSEC Method

The PARSEC parameters are the parameters to be determined, given a list of coordinates which define an airfoil. A simple flow diagram is given in Figure 6 which describes the steps followed in the next paragraph.

Consider an airfoil represented in 2D space by x and z coordinates. The calculation of the PARSEC parameters is an optimization problem. An airfoil's z coordinates, is cast into vector form $\boldsymbol{z} = \{z_1, z_2, \dots, z_n\}^T$ where n is the number of points. The design vector is the PARSEC parameters, given as $\boldsymbol{P} = \{r_{\text{le, lo}}, r_{\text{le, up}}, \dots, \Delta Z_{\text{te}}\}^T$. The initial guess for the PARSEC parameters is denoted as $\boldsymbol{P_0}$ and the vector which minimizes the objective function (i.e., the optimal vector) is denoted by $\boldsymbol{P}^*$. The objective function is defined as the mean squared error (MSE) of the actual airfoil, denoted by $\boldsymbol{z}_{\text{actual}}$ and the calculated airfoil, denoted by $\boldsymbol{z}_{\text{model}}$. The sequence of the values in the $\boldsymbol{z}$ vectors are important and is chosen to be ordered (or indexed) from the upper trailing edge to the leading edge and back to the lower trailing edge. The residual, $\boldsymbol{r}$, is defined as

$$\boldsymbol{r} = \boldsymbol{z}_{\text{actual}} - \boldsymbol{z}_{\text{model}} \tag{13}$$

and can then be used to calculate the MSE, which is the objective function, $f(\boldsymbol{P})$, as

$$f(\boldsymbol{P}) = \frac{\boldsymbol{r}^T \boldsymbol{r}}{n} \tag{14}$$

This is therefore an unconstrained optimization problem that can be formulated as

$$\text{minimize } f(\boldsymbol{P}) \tag{15}$$

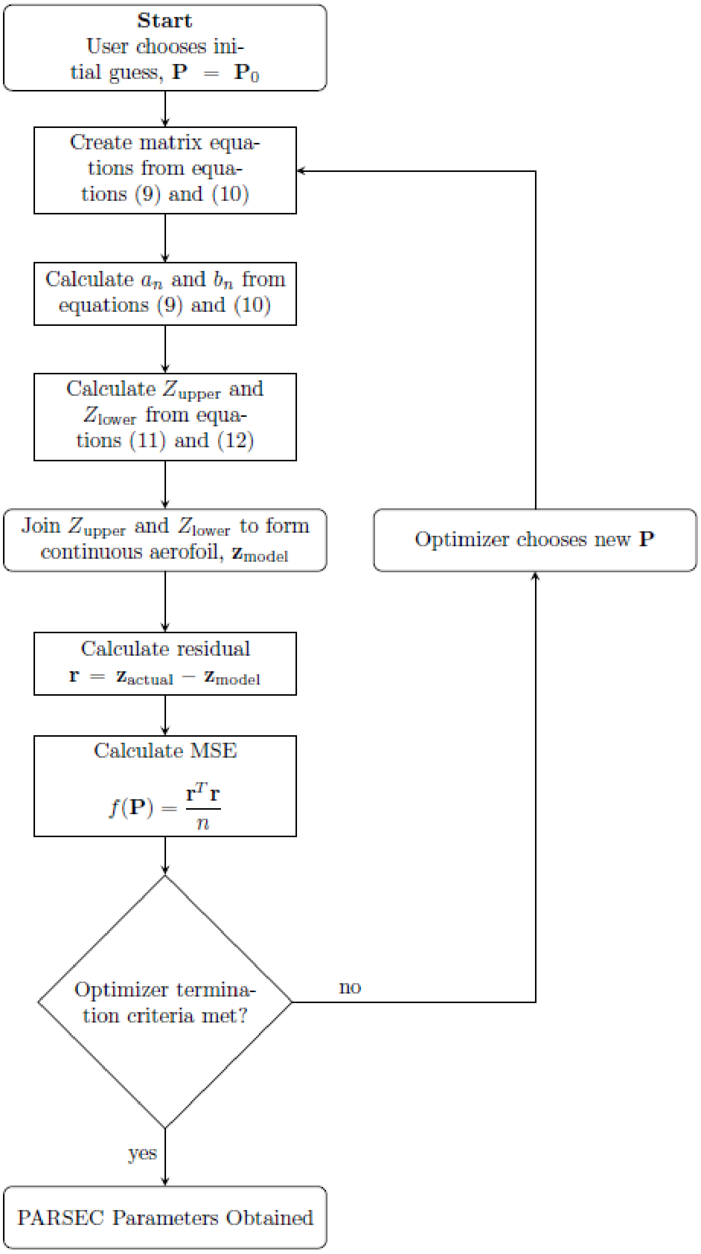

Figure 6: Flowchart showing the process for determining the PARSEC parameters given the coordinates which makes up an airfoil.

Known airfoils were used to verify whether this workflow can compute the PARSEC parameters from a set of coordinates. A random value in the range of [-0.005,0.005] was added to each *z* coordinate for the airfoil (which have chord lengths of unity) to incorporate outlier data. This introduced the uncertainty similar to the fitting of the actual GHA airfoils.

The next step was to choose an appropriate optimization algorithm. There are two algorithms that can be used. The first is a common gradient descent (GD) algorithm, which evaluates the influence of an infinitesimal change in each parameter and evaluates the resulting objective function value. The gradient is calculated between the original objective function value and the next iteration's objective function value. The design space is then traversed in the direction opposite to the calculated gradient with a certain step size. This will cause the optimizer to find a local minimum (Cauchy, 1847).

The other method that can be used is a metaheuristic algorithm. The specific optimizer used is that of differential evolution (DE, Storn and Price, 1997). This optimization algorithm does not work by computing gradients, and it does not require that the objective function be differentiable and continuous. DE optimizes a problem by presenting a population of candidate solutions. New candidate solutions are computed by combining existing ones according to the simple governing formula. Candidates which have the best score (referred to as fitness) are kept in the candidate solutions and candidates with low scores are eliminated. The further the solution progresses, increasingly more fit candidates are paired, giving better "children" (or next candidate solutions).

The two optimizers, the robustness thereof, and the ability to match the known airfoil was tested. This was done by attempting to recreate airfoils with known geometries. The optimization was done in Python using the *optimize* module in *SciPy*. The two functions used were, *minimize* and *differential evolution*.

Both optimizers take inputs which specify the lower and upper bound of each PARSEC parameter. The bounds were chosen at an arbitrary range of (-30, 30) to serve as an infinitely large search space for the airfoil (with a chord length of 1). All parameters were assigned these bounds (with the angular parameters having units of degrees), except for the parameters, $r_{\mathrm{le,\,lo}}$, $r_{\mathrm{le,\,up}}$, X_{lo}, and X_{up} whose lower bounds were set to 0. The reason for this is simple when looking at equations (9) and (10). The 4 parameters mentioned are encountered in terms where fractional powers are applied and therefore would produce non-real numbers when containing negative values. The reason for the other bounds being set to a range of (-30, 30) was simply to enlarge the design space.

These values could have been much larger, but it would increase the time to calculate the PARSEC parameters. Bounds smaller than this could lead to restrictions in the size of the design space. For clarity, the bounds are also shown in Table 3. The airfoils recreated using the PARSEC method is shown in Figure 59 through Figure 66 in Appendix A. The deviation of the calculated airfoil using both optimizers are also shown along with the time taken in seconds to calculate the PARSEC parameters. It is noted that the DE optimizers takes 15 to 150 times longer to compute the correct PARSEC parameters. An example of a recreated airfoil is shown in Figure 7.

Table 3 Bounds used to determine PARSEC parameters of common airfoils using two different methods of optimization.

	$r_{\text{le, lo}}$	$r_{\text{le, up}}$	X_{lo}	X_{up}	Z_{lo}	Z_{up}	$Z_{\text{xx, lo}}$	$Z_{\text{xx, up}}$	α_{te}	β_{te}	Z_{te}	ΔZ_{te}
Lower Bound	1e-5	1e-5	1e-5	1e-5	-30	0	-30	-30	-30	-30	-30	0
Upper Bound	30	30	1	1	-30	1	30	30	30	30	30	30

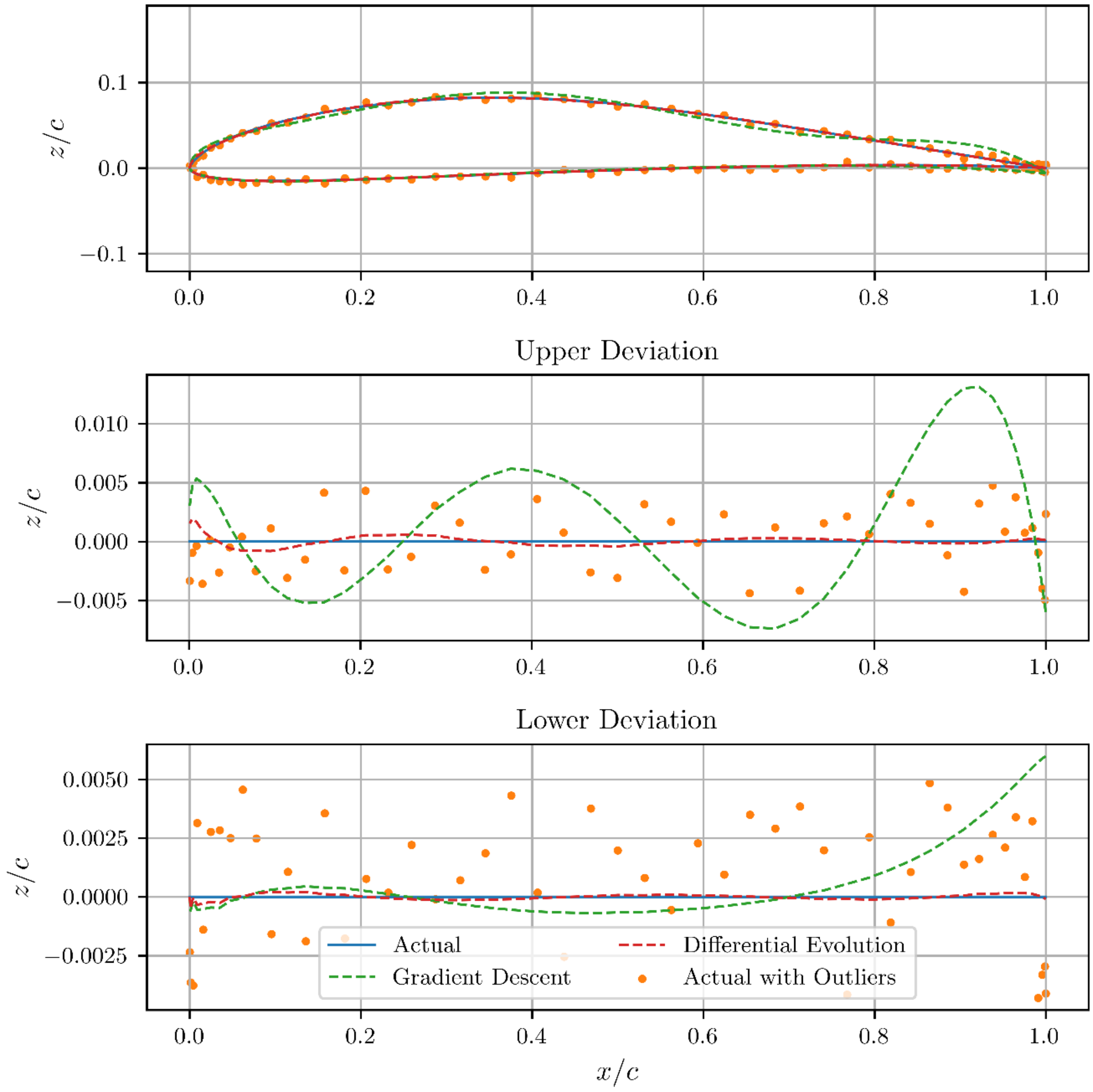

Figure 7: Recreated E387 airfoil with the upper and lower errors with GD and DE. Times: GD: 0.25s, DE: 38.57s

The MSE using the DE optimizer was on average 6.5×10^{-6} whereas the GD optimizer was on average 3.12×10^{-5}. The MSE between the airfoil with outliers and normal airfoil was on average 7.38×10^{-6}, showing that the DE optimizer is able predict the actual airfoil with the smallest MSE. This indicates that the PARSEC method using a DE algorithm is a reasonable method to extract the 12 PARSEC parameters from an airfoil containing outliers and recreate it without outliers. This method will be applied to the GHA wing.

The accuracy was however at the cost of time. The GD algorithms took on average less than a quarter second to calculate the PARSEC parameters from the airfoil provided, whereas the DE algorithm took in the order of 15 seconds, an increase of almost 100 times. This time penalty was acceptable since the focus was on developing a realistic geometry which has 30 airfoils along the span of the wing. The PARSEC method is a feasible approach to airfoil parameterization and was therefore used in the rest of the study.

3.3. Pre-processing Point Cloud data

Converting a real-life wing specimen to a useable 3D model (whether it be for simply quantifying the geometry of the wing, manufacturing a wing, or performing numerical analysis on a wing) is an interest which divides many authors (Liu *et al.*, 2006; Klän *et al.*, 2009; Carruthers *et al.*, 2010; Rader *et al.*, 2020; Waldrop *et al.*, 2020) and therefore the methods employed to do so varies drastically between publications as shown in Section 2.2.

The process used in this study started with 3D laser scanning the wing which produced a point cloud, each point having its own (x, y, z) coordinate in space. The point cloud could simply be meshed to form a useable model, if it were not for two fundamental problems about bird wings. The first problem was the thin nature of the wings (and other avian wings in general). It was found that there were sections on the trailing edge which were essentially a few microns thick, and the 3D laser scanner simply did not have the capability to capture this type of resolution. This caused "open" sections in the wing surface and the final model should ideally be watertight (shown in the orange region in Figure 8).

The second problem was the presence of feathers which were out of place, i.e., outlier feathers (shown in the green region in Figure 8). This could have been caused by many factors, such as transportation, handling, or the curing process through which the wings went.

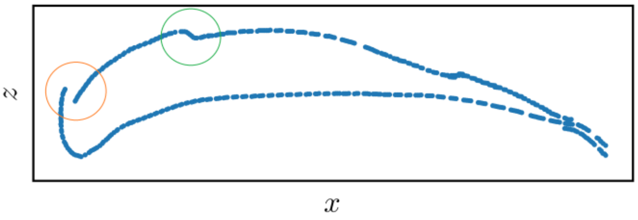

Figure 8: A raw scatter plot of a 3D scanned airfoil of the GHA showing examples of open sections (orange) and outlier regions (green).

Therefore, the 3D point cloud had to be smoothed using consistent mathematical models. This is a one of the two reasons why the PARSEC method was used (remembering that the two reasons were smoothing noisy airfoils and creating an airfoil in a parameterized domain). The PARSEC method enables smoothing and interpolation between open sections in a way that is airfoil-like (made for creating airfoils).

In this study the point cloud was generated by a handheld 3D scanner (Einscan Pro HD, Shining 3D). The point cloud was then imported into CloudCompare, an open-source point cloud processing software. The points were transformed to a coordinate system roughly located at the tip of the wing. The sectioning function in CloudCompare was used to extract airfoils at different spanwise locations, shown in Figure 9.

Individual airfoils were exported as *.txt* files containing (x, y, z) coordinates. The exported points were not in a typical order for defining airfoil surfaces (i.e., looping from the top trailing edge to the leading edge and back to the lower trailing edge).

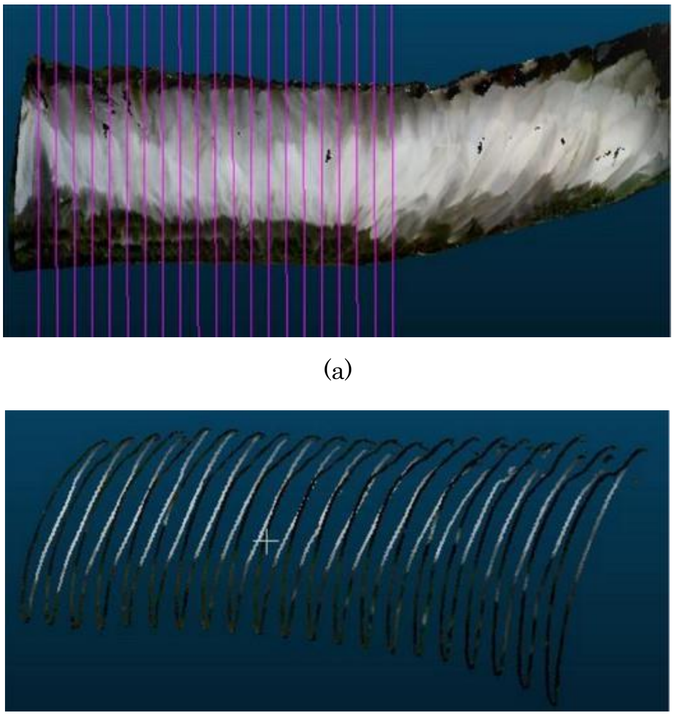

(a)

(b)

Figure 9: The airfoil creation process in CloudCompare showing (a) the lines where the sections were to be taken and (b) the result of the sectioning process.

The airfoil extraction process started with importing the points, shown in Figure 10, using only the x and z coordinates.

The points were rotated manually so that airflow in the positive x direction would meet the leading edge before the trailing edge, shown in Figure 11. The solid blue lines connect consecutive data points according to their index number. This showed that the points were randomly ordered.

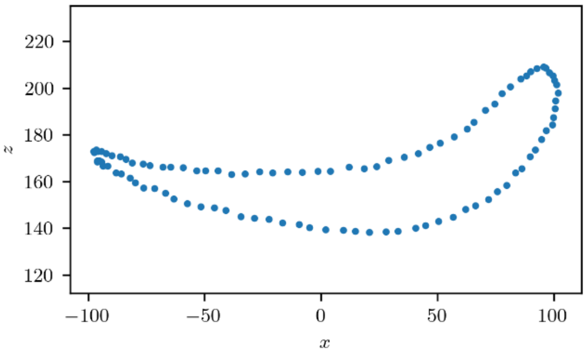

Figure 10: Imported points as exported from CloudCompare.

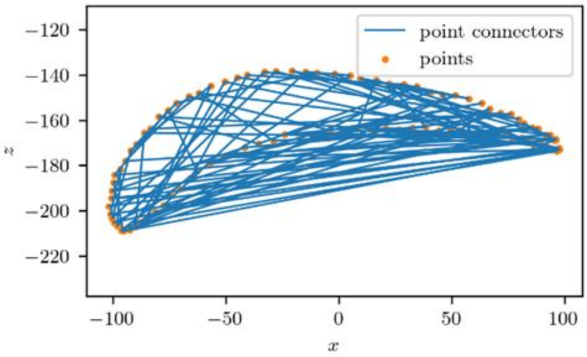

Figure 11: Manually rotated points which aimed to ensure that airflow in the positive x direction would meet the leading edge first.

The points were then sorted in increasing x so that if the data were plotted, lines would roughly move between the upper and lower surface, shown in Figure 12.

Next, three transformations were applied. The first being a translation, the second a rotation and the third a scaling transformation. The translation transformation located the leading edge (i.e., the point with the minimum x value) and recorded the x and z coordinate. All points were then moved so that this point was located exactly on the origin, shown in Figure 13.

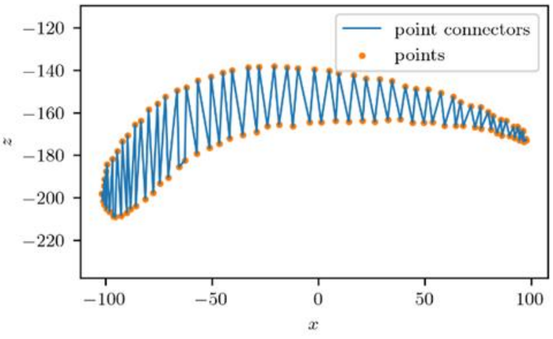

Figure 12: Data sorted in increasing x

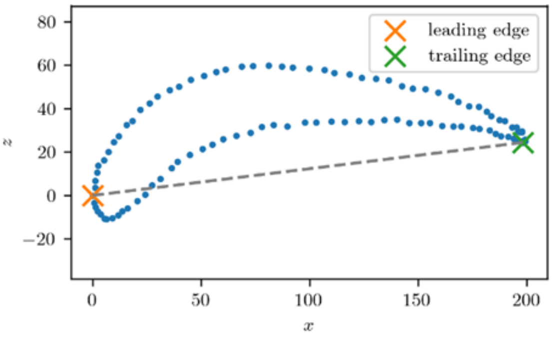

Figure 13: Translating the data to have the leading edge located at the origin.

The rotation transformation was applied to align the chord line to the x axis with the added benefit of calculating the local twist angle. The rotation transformation located the trailing edge by searching for the minimum z value in the second half of the data (i.e., to the right of the vertical line which would split the data in two). The local twist angle was then simply calculated as $\theta = arctan(z_{\text{te}}/x_{\text{te}})$ as the leading edge was already located at the origin. The rotated points were then computed as follows and is shown in Figure 14.

$$\text{rotated points} = \begin{bmatrix} x_1 & z_1 \\ x_2 & z_2 \\ \vdots & \vdots \\ x_n & z_n \end{bmatrix} \begin{bmatrix} cos(-\theta) & sin(-\theta) \\ -sin(-\theta) & cos(-\theta) \end{bmatrix} \tag{16}$$

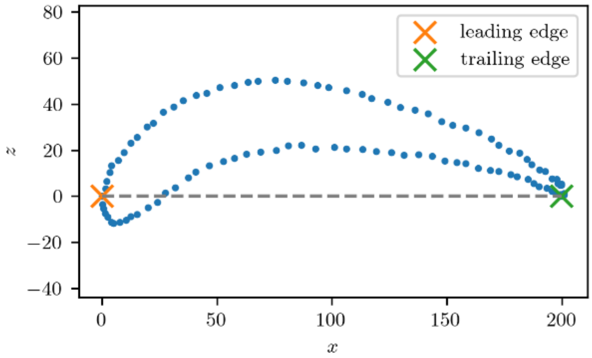

Figure 14: Rotating the points to ensure that the leading and trailing edges are exactly horizontal.

The data was shifted and rotated until both criteria were satisfied. In the example given, this was not required but it had to be implemented in some cases. This was done to ensure that the rotation transformation did not unintentionally introduce a new leading edge. The monitored quantities that were used to determine whether a new leading edge was introduced was the x and z location of the leading edge (which should both be equal to 0 in the end), the rotation θ and the trailing edge z coordinate. In this example, the transforms did not induce a new leading edge but in some cases this happened. The translations and rotations are shown in Figure 15.

The maximum x coordinate was determined, and all the points' x and z values were divided by this value, to scale the data. This caused the x data to be between 0 and 1 which normalized the chord length, shown in Figure 16. The total translation, $(x_{\text{translate}}, z_{\text{translate}})$, rotation, θ, and scaling, c, (which is also just the local chord length) was stored for later use.

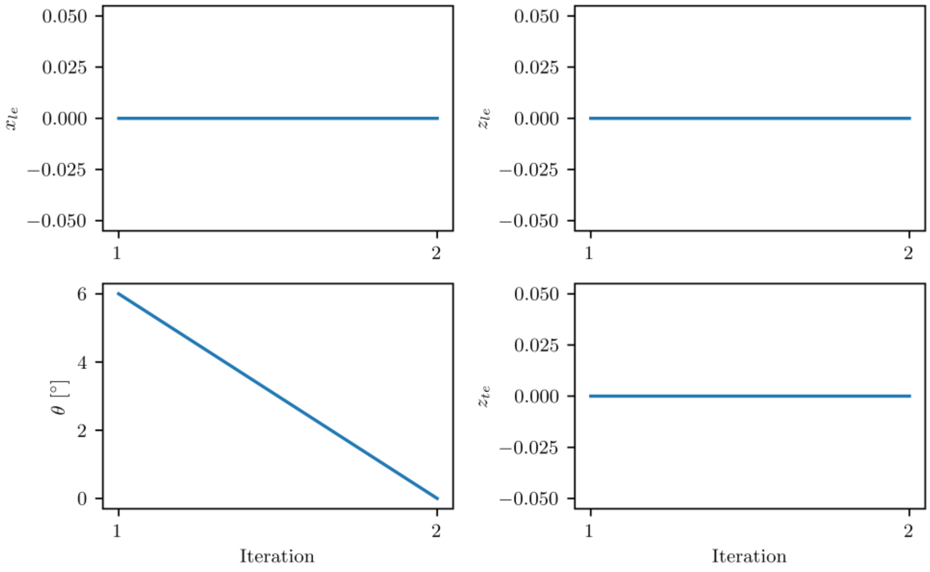

Figure 15: The quantities that were being monitored to ensure that the transforms did not induce new leading and/or trailing edges.

The next important consideration was the indexing of the data. The Birnbaum-Glauert camber line was calculated according to equation (1), shown in Figure 16 using $z_{\text{c, max}} = 0.3$. It was found that the value of $z_{\text{c, max}}$ did not play a significant role in the actual location of the maximum camber. This was again done using a least squares approach to calculate the values of S_n where $n = 1, 2, 3$.

The calculated camber line was then used to split the data into a top and bottom surface by simply checking whether the z value of the airfoil data point was above or below the camber z coordinate, shown in Figure 17.

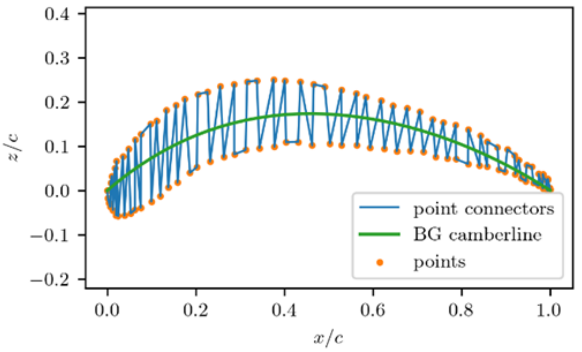

Figure 16: The points were scaled to a chord length of unity and the Birnbaum-Glauert camber line was fit to the data for the purpose of splitting the upper and lower surfaces.

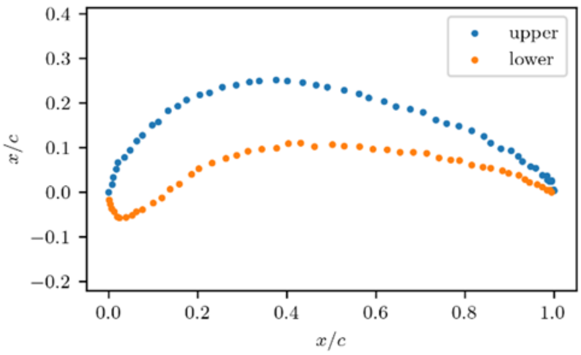

Figure 17: The upper and lower surfaces split using the Birnbaum-Glauert camber line.

The top and bottom surfaces had x spacings which were irregular lengths between successive points. The z data from the airfoil was interpolated against a self-defined distribution of x values. The x values which were used for the interpolation was a sequence created using the following formula,

$$x_i = \frac{1}{2}\left[\sin\left[\frac{-\pi}{2} + (n-1)\left(\frac{\pi}{50-1}\right)\right] + 1\right], \text{for } i = 1,2,\dots,50 \tag{17}$$

The calculated distribution is shown in Figure 18, and points were concentrated higher at the leading and trailing edges as the curvature in these regions were generally higher and more points were required to capture the data well.

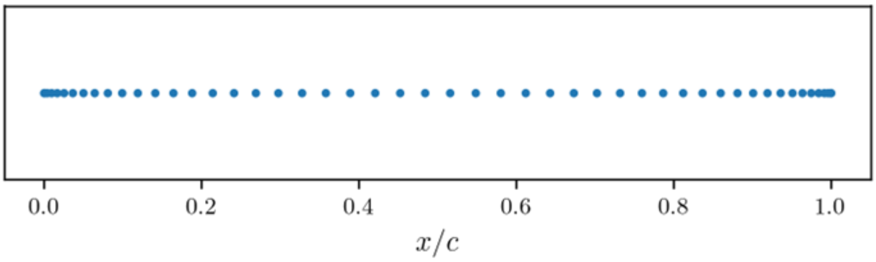

Figure 18: Sinusoidal spacing of x values used for the interpolation of the airfoil data.

The top and bottom surfaces were interpolated against the x values shown, and the data was then joined in the correct sequence. The data was indexed from the top point of the trailing edge (index 0), around the leading edge (some intermediate index), to the bottom point of the trailing edge (last index or index -1), shown in Figure 19.

All of these steps were repeated on each airfoil and the next step was to use of all the processed airfoils to create a quantified geometry of the GHA wing.

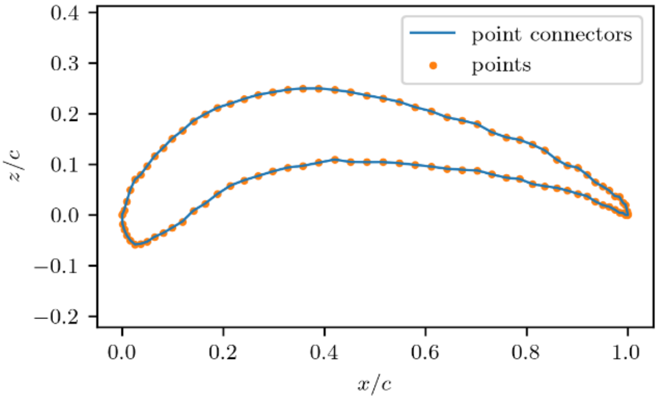

Figure 19: Interpolated and sequenced data ready for use in the next part of the geometry investigation.

3.4. Quantified geometry of the Grey-headed Albatross Wing

The airfoil data was used to calculate new airfoils using the PARSEC method as well as the Birnbaum-Glauert method used by Liu et al. (2006) and Klän et al. (2009). The PARSEC method was implemented exactly like that shown in section 3.2, Figure 6, using the DE optimizer. The airfoil camber and thickness profiles were estimated using the Birnbaum-Glauert method. The coefficients A_n and S_n were calculated from equations (1) and (2) using a least squares approach. These coefficients were then used to calculate the camber and thickness using equations (3). The PARSEC method results had to be broken down into thickness and camber lines in order to compare results to the Birnbaum-Glauert method. The camber was simply the average of the z coordinates of corresponding x values and the thickness was the difference between the top surface z values and the camber z values for corresponding x values. The quantified geometry of the GHA using the Birnbaum-Glauert and PARSEC method as well as the deviations between the two methods and the actual scanned quantities are shown in Figure 20 and Figure 21.

Figure 20 shows the Birnbaum-Glauert camber calculation and the PARSEC method camber calculation and it was evident that the Birnbaum-Glauert method had small regions of higher deviations from the actual measured camber, especially at the root section. The BG and PARSEC method shows bands of deviations as well as small local points of error, such as at the wrist section for the BG method and the root section for the PARSEC method.

Significant differences between the two methods were evident upon investigation of the calculated thickness distributions (Figure 21a). The average thickness deviation of the BG method has a magnitude of $0.0057c$ whereas the PARSEC method had an average deviation of $0.002c$ (Figure 21b). The BG thickness deviation exhibited broad bands of high deviation whereas the PARSEC method thickness did not. The PARSEC method therefore provides a more realistic description of the GHA wing geometry compared to that of the BG method. Although there were small locations of high deviations in both cases, these locations were consistent with the locations encountered in the camber deviations.

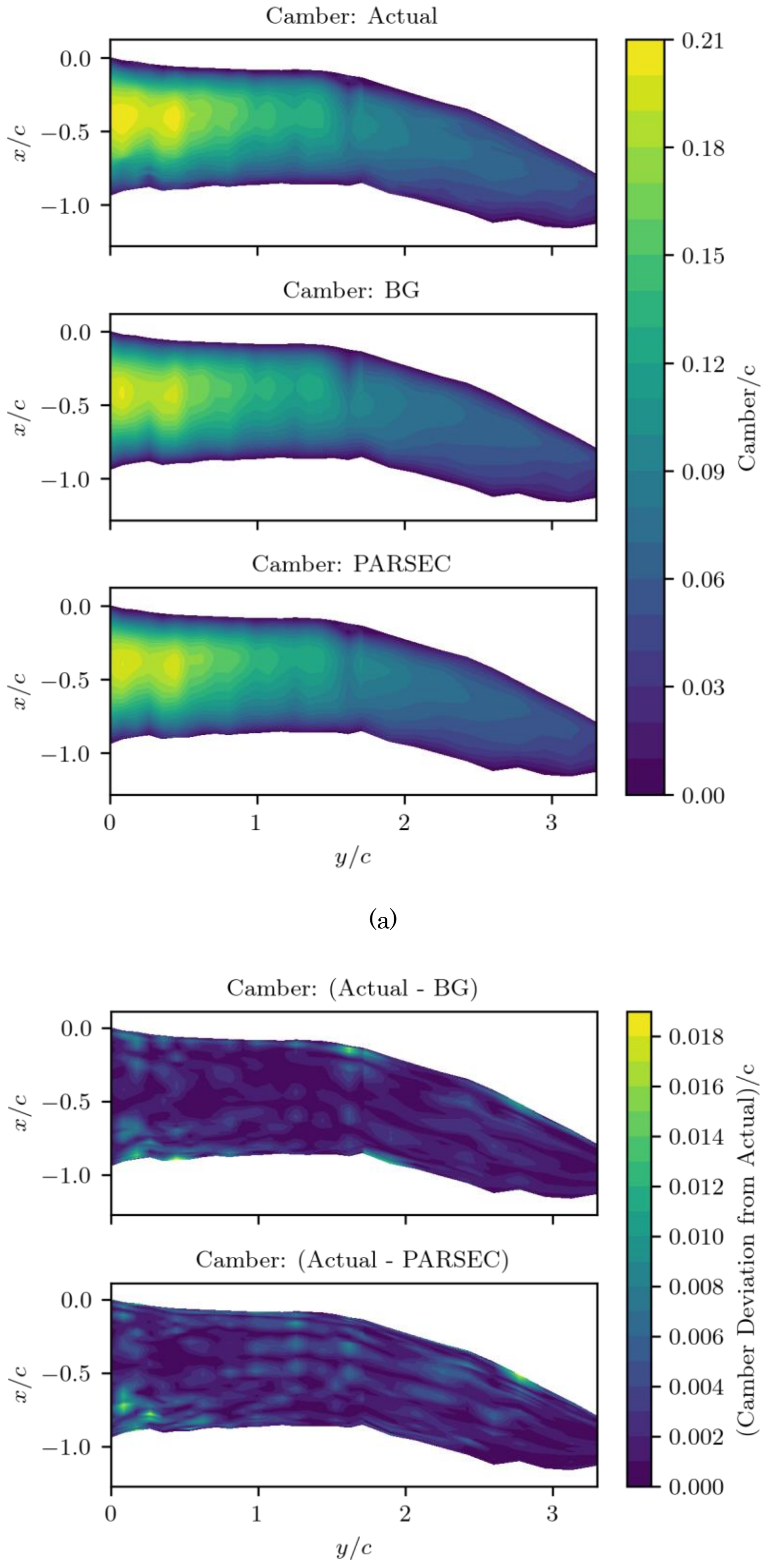

(a)

(b)

Figure 20: A comparison between the PARSEC method and the Birnbaum-Glauert method for calculating the (a) camber and (b) calculating the deviation between the actual camber (absolute value), and the PARSEC and Birnbaum-Glauert methods normalized by $c = 0.2$m.

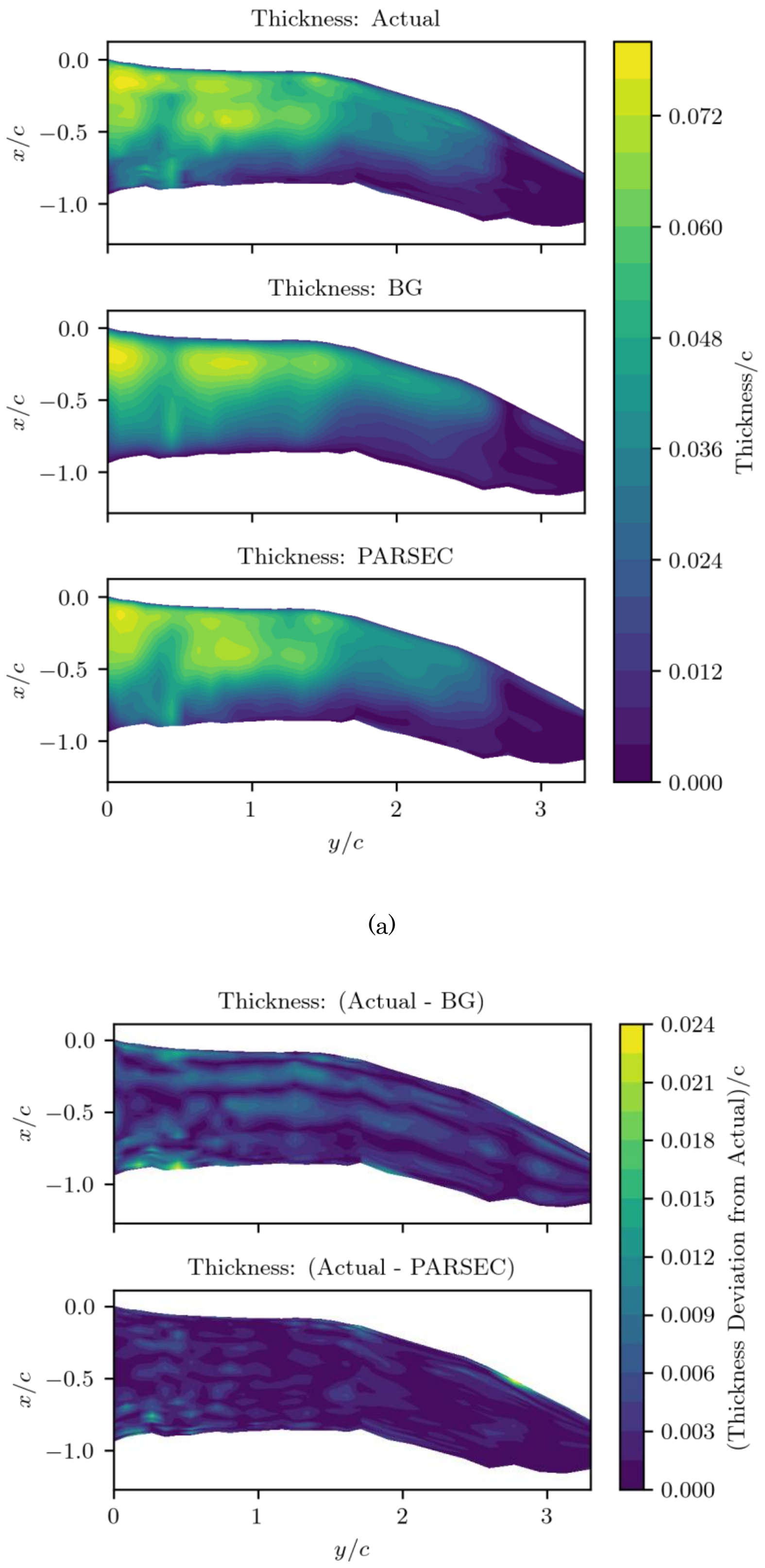

(a)

(b)

Figure 21: A comparison between the PARSEC method and the Birnbaum-Glauert method for calculating the (a) thickness and (b) calculating the deviation between the actual thickness (absolute value), and the PARSEC and Birnbaum-Glauert methods normalized by $c = 0.2$m.

The quantities of chord length, twist, sweep, and dihedral are all plotted against the normalized spanwise coordinate in Figure 22. Airfoils and data thereof were not extracted for spanwise locations near to the tip of the wing since the small chord length eventually terminates at a chord length of zero.

The chord length is simply the value which was used to scale the airfoils to a chord length of unity, which was previously calculated. The twist of each airfoil was the sum of all the rotation transformations applied. The sweep and dihedral were the only quantities which required a bit more work to obtain.

For the sweep values, the quarter chord locations of the different airfoils were used. To determine this, the x translation of an airfoil was used in conjunction with the chord length. Visualizing an xy plane, which would represent the planform of the wing this concept can be easily understood. Knowing the location of the leading edge, i.e., the x translation and the chord length, can yield the trailing edge x location. The quarter chord position was simply the addition of $0.25c$ with the x location of the leading edge in the direction of the trailing edge. Doing this with each airfoil yielded a set of points which described the quarter chord line, from the root to the tip in the spanwise direction. The sweep values reported was the displacement in the x direction relative to the quarter chord position of the root airfoil. The idea is visually explained in Figure 23.

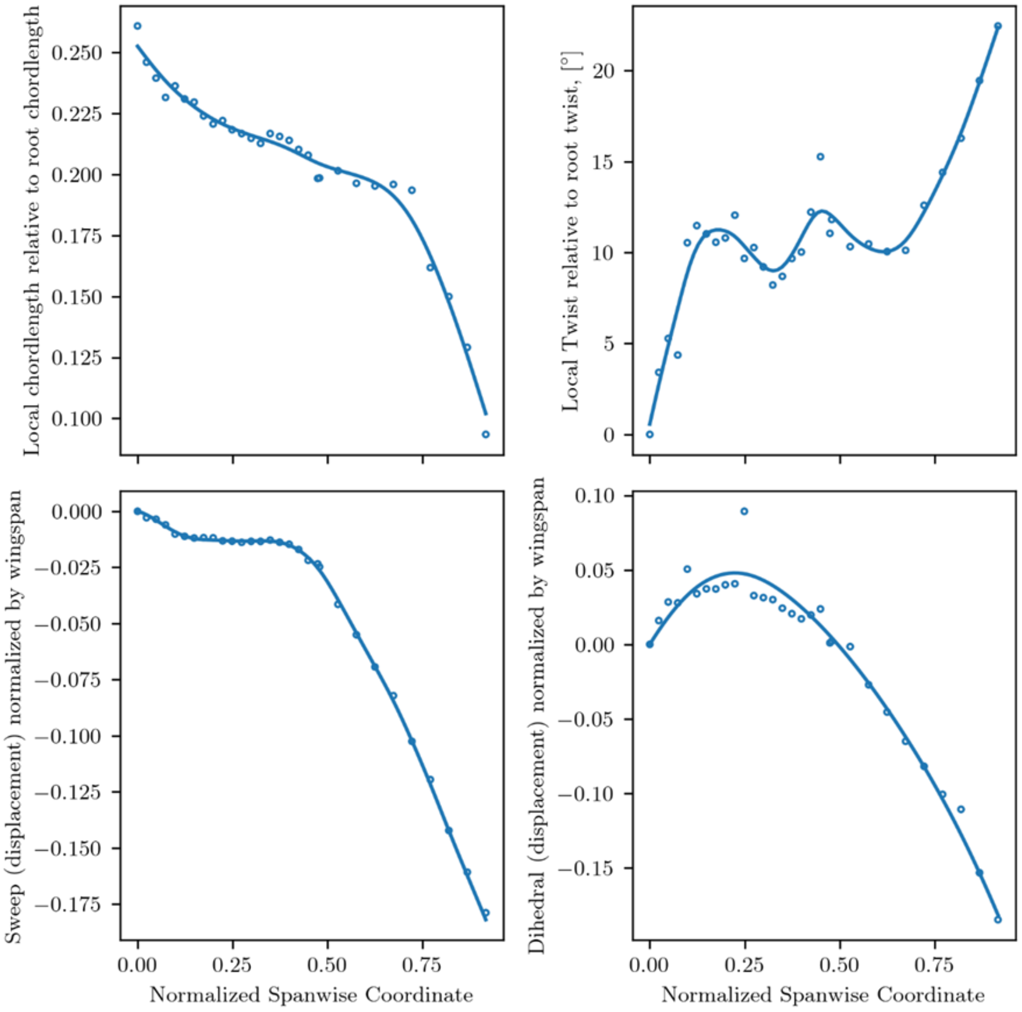

Figure 22: Local chord length, local twist, sweep, and dihedral as functions of the normalized wingspan of the GHA. The original data is plotted using the circular markers and the smoothed data is plotted using the line.

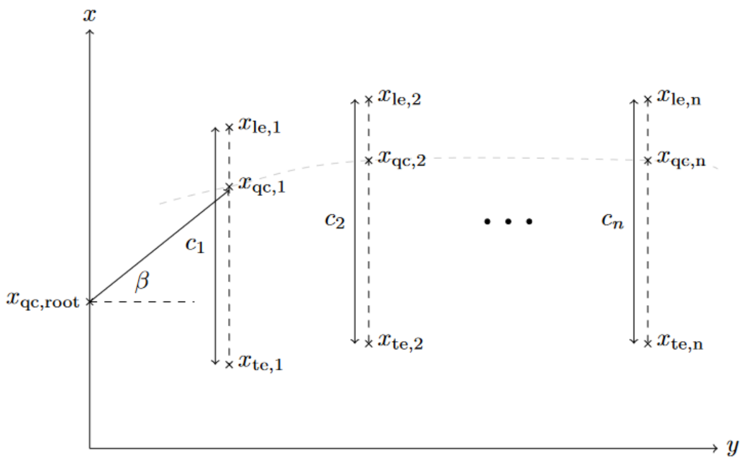

Figure 23: Visualization of the quarter chord location from the x translation and c values captured, for three arbitrarily spaced airfoils in the spanwise direction. The light grey line can be seen running through the quarter chord positions. The sweep angle is indicated by β.

After all the quarter chord x coordinates were known, the z coordinate of quarter chord position had to be determined. This was done in the same way as the x locations shown in Figure 23, except in this case on the yz plane. Visualizing the dihedral on the yz plane simplifies this concept, as shown in Figure 24.

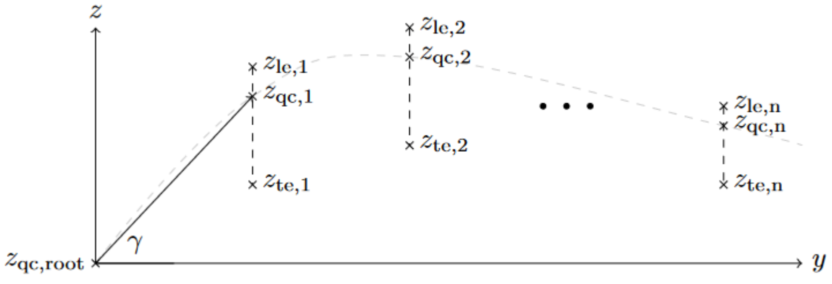

Figure 24: Visualization of the quarter chord location from the z translation and the c values captured, for three arbitrarily spaced airfoils in the spanwise direction. The light grey line can be seen running through the quarter chord positions. The dihedral angle is indicated by γ.

The dihedral reported is the z displacement between the root and the specific airfoil normalized by the wingspan using a half span length (single wing length) of 650mm. The original data shown in Figure 22 cannot be used unprocessed, since the sudden changes in these parameters would cause discontinuities in the geometry. To account for these discontinuities, a cubic spline was fitted to the data. This spline requires an input called a smoothing value which ranges between 0 and 1. A smoothing value of 1 will have no smoothing and will include all points through which the interpolation will happen. A value of 0 will fit a least-squares straight line through the data. The smoothed data is also shown in Figure 22.

Using the chord length, twist, sweep and dihedral data (Figure 22), the wing was reconstructed as a smooth model shown in Figure 25.

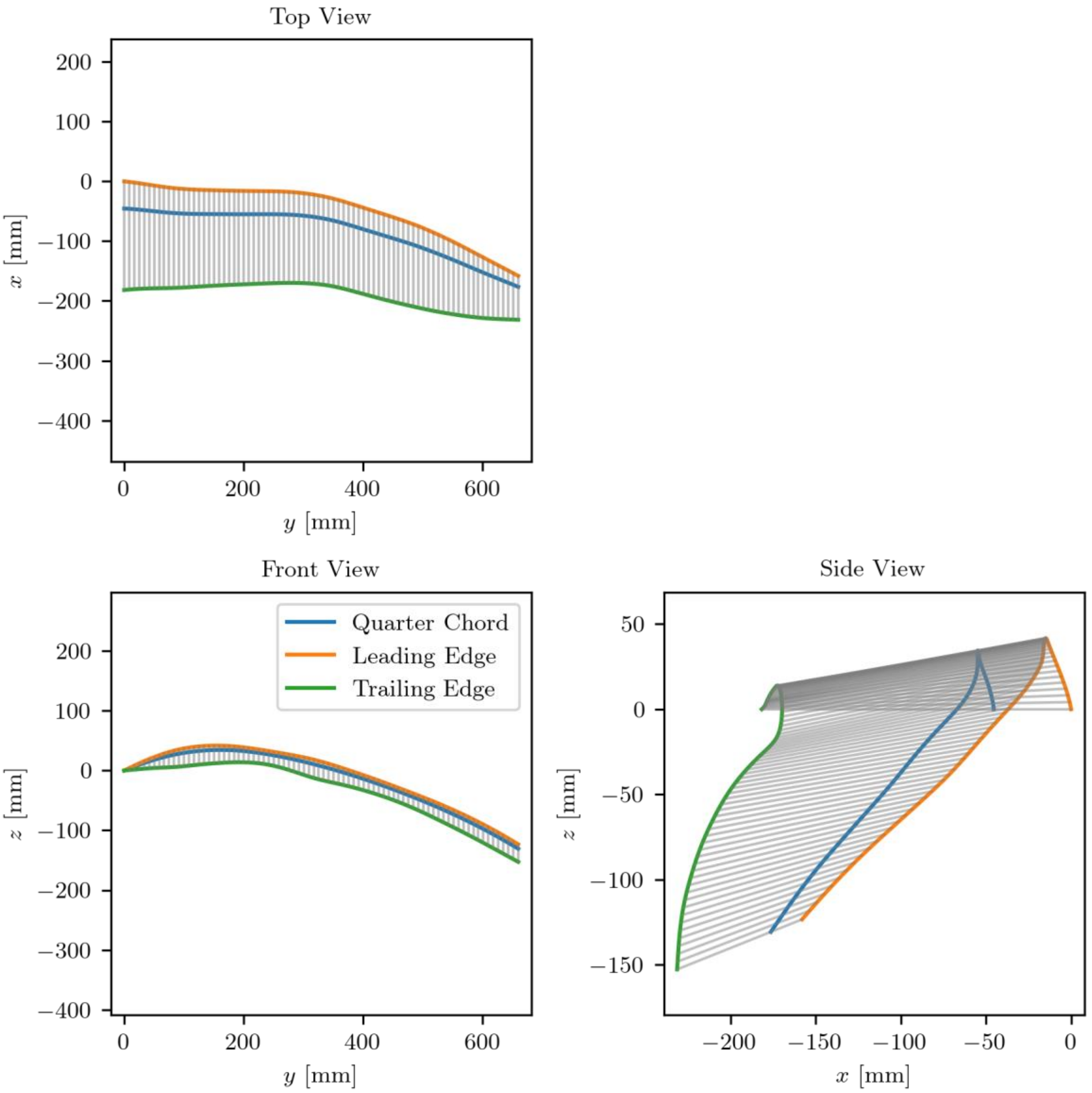

Figure 25: Recreated GHA wing constructed from the macro wing parameters. (Grey lines on the Side View and Top View are included to indicate the twist).

The 3D computer-aided design (CAD) model was created using a loft action in SolidWorks. At least two guide curves are required to perform a loft action. The two guide curves in this case were the leading and trailing edge curves, shown in Figure 25. These curves are a set of (x, y, z) coordinates which are used to enforce the twist, chord length, and spanwise profile of the wing. The two profiles that were used were the average hand section airfoil (located at the tip), and the average arm section airfoil (located at the root), shown in Figure 26. The fidelity of the 3D model can be increased if more airfoils are used as loft profiles between the two extremes (root and tip). Since the outcome of this part of the research is stated as simply aiming to provide a methodology and concept for 3D model creation, using two airfoils are sufficient.

Table 4: Average PARSEC parameters and standard deviations for the arm and hand section of the GHA wing.

Parameter	Arm		Hand	
$r_{\text{le, lo}}$	0.1405	0.09	0.0441	0.06
$r_{\text{le, up}}$	0.2485	0.09	0.1348	0.07
X_{lo}	0.4230	0.11	0.3774	0.07
X_{up}	0.3683	0.02	0.3431	0.07
Z_{lo}	0.1131	0.03	0.0728	0.02
Z_{up}	0.2616	0.04	0.1509	0.03
$Z_{\text{xx, up}}$	-2.0722	0.50	-1.0825	0.40
$Z_{\text{xx, lo}}$	-1.2498	0.65	-0.7354	0.74
α_{te}	-32.593	6.93	-18.491	11.49
β_{te}	17.691	14.12	-2.758	13.04
Z_{te}	0.0106	0.01	0.0130	0.01
ΔZ_{te}	0.0200	0.02	0.0054	0.01

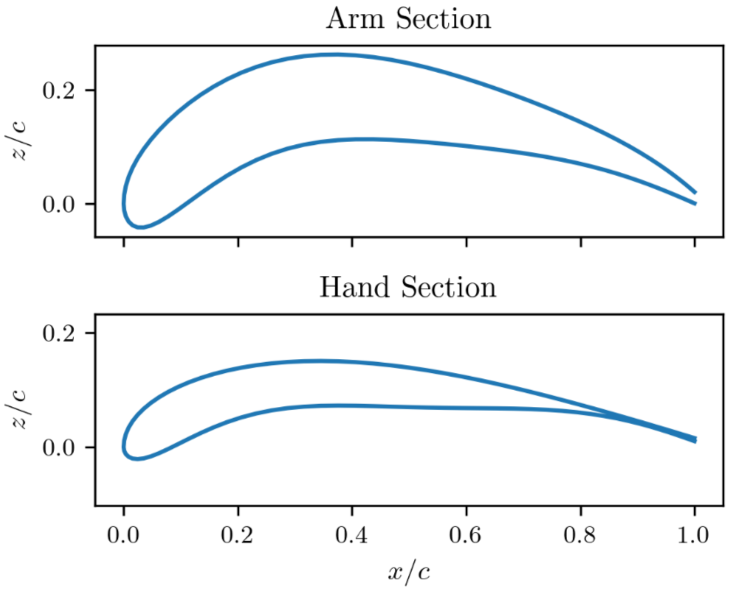
Arm Section

Hand Section

Figure 26: Average arm and hand section airfoils as calculated using the PARSEC parameters.

An example of a 3D CAD model created using all the information presented above is shown in Figure 27.

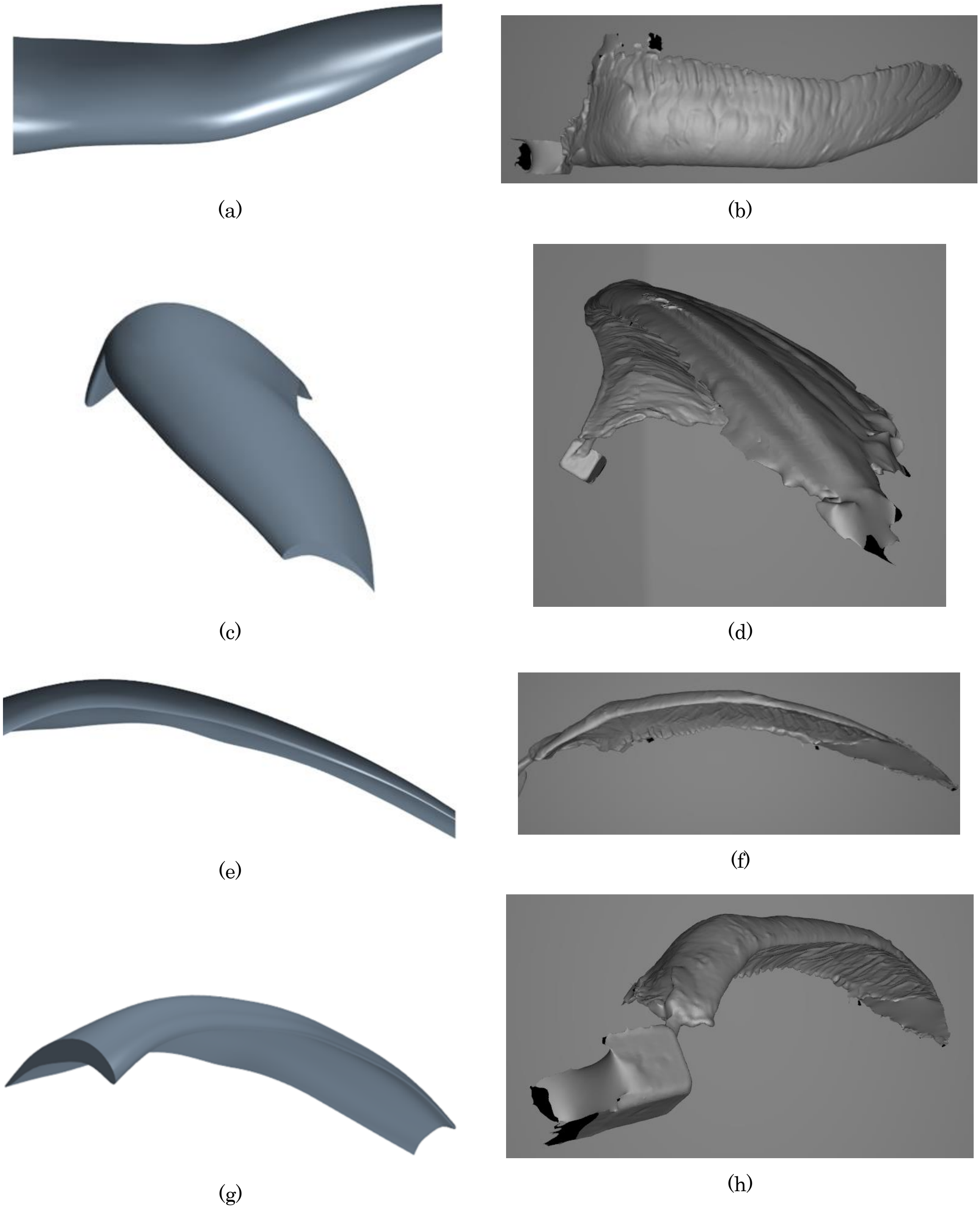

Figure 27: GHA 3D CAD model created using the data presented in this section compared to a raw 3D scan showing the (a,b) top view (c,d) left view (e,f) front view, and (g,h) isometric view.

4. Validation of the numerical approach

In this section the CFD approach is validated. An Eppler 387 (E387) airfoil was chosen as a test geometry. This is a cambered low Reynolds number airfoil which is similar to the geometry of the GHA wing that was used later in the study. The experimental data that was used in this section was that obtained by McGhee and Walker (1989) at the Langley Low-Turbulence Pressure Tunnel (LTPT), Althaus and Wortmann (1981) in Stuttgart, and Volkers (1977) in Delft. The domain and mesh are validated before the generated results are compared to these literature sources.

4.1. Pseudo Two-Dimensional Domain Set-up

A P2D domain was used to capture 3D effects on the model. The outlet length of the domain was 60c downstream of the wing, the inlet radius was 30c and the width was 0.1c, as shown in Figure 28. The values for the flow variables and reference lengths and areas used in the numerical analyses is given in Table 5.

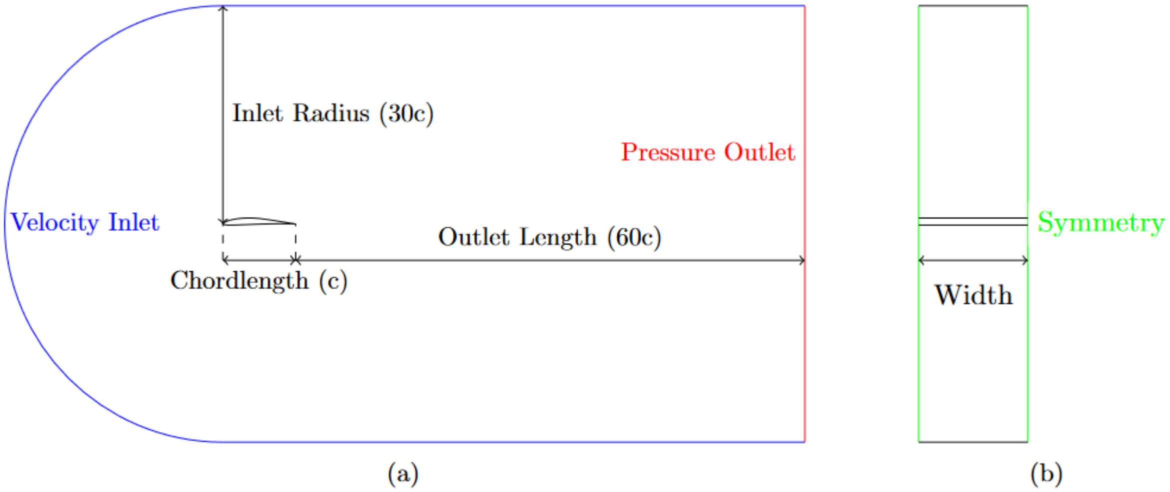

Figure 28: Domain used for the pseudo two-dimensional study showing the (a) right view and (b) front view.

Table 5: Flow variables used in the numerical analyses.

Quantity	Symbol	Value
Inlet Velocity	V	15.7ms^{-1}
Freestream Pressure	P_∞	101.325kPa
Freestream Density	ρ	1.1768kgm^{-3}
Freestream Dynamic Viscosity	μ	1.855×10^{-5} kg(ms)$^{-1}$
Chord length	c	0.2m
Area	S	4×10^{-3}m^2

The SST $k-\omega$ turbulence model with the $\gamma-\mathrm{Re}_\theta$ transition model (Menter *et al.*, 2006), is selected with low y^+ wall treatment similar to other low Reynolds number studies (Choudhry et al., 2015; Chen et al., 2020). The initial mesh, shown in Figure 29, incorporated downstream wake refinement parallel to the incoming flow vector which extended $30c$ downstream with cell sizes of $0.02c$. This was staggered with another downstream wake refinement region which was also $30c$ (i.e., to the outlet length of the domain) with cell sizes of $0.08c$. The prism layer mesh on the surface of the airfoil used eighty prism layers, with a first prism layer height of 0.01mm ($5\times10^{-5}c$) and a total thickness of 14mm ($0.07c$). The 80 prism layers were necessary to resolve both the velocity gradients introduced by the boundary layer and the separation bubble formation due to the adverse pressure gradient. The target surface cell size was 2mm ($0.01c$). The solution was initialized using the grid sequencing method which aimed to speed up the initial convergence of the simulation.

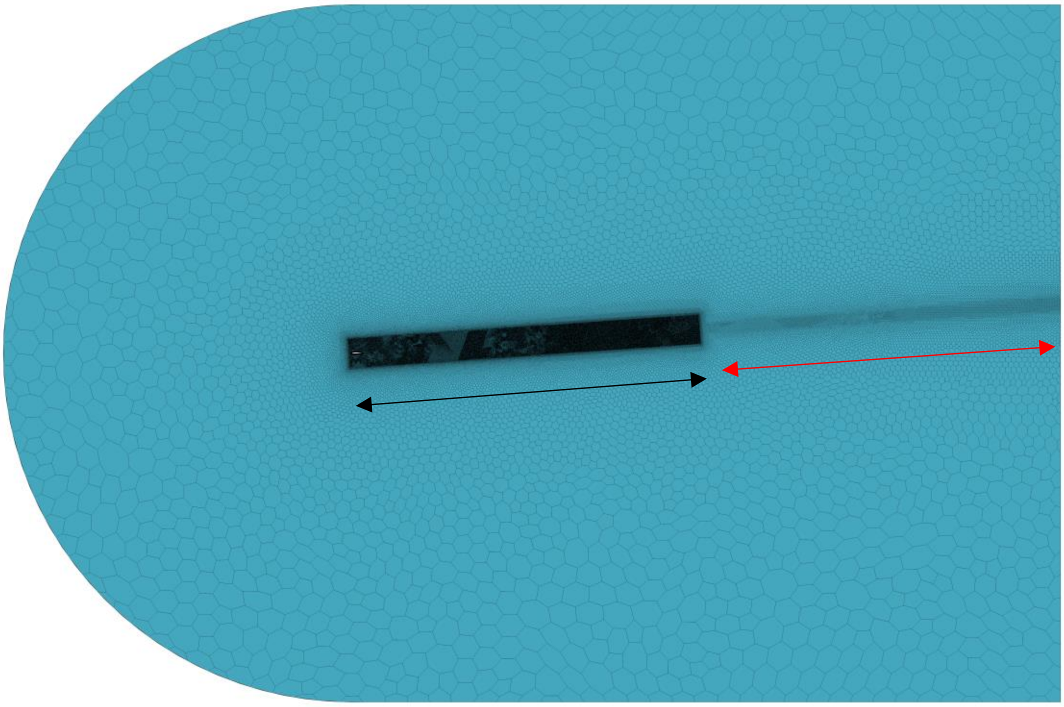

(a)

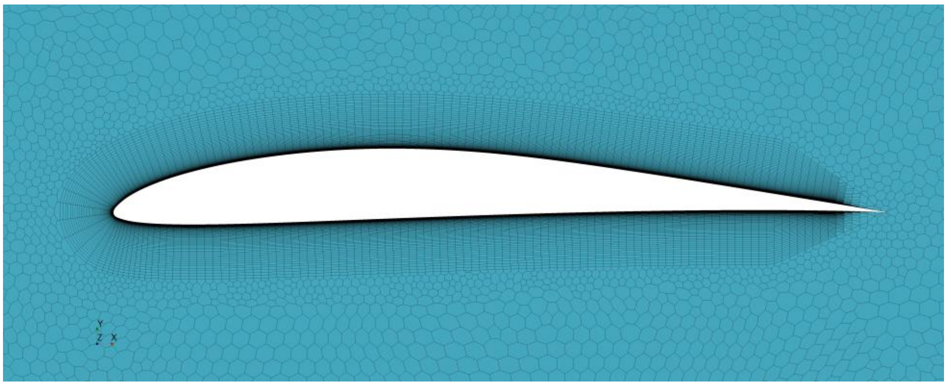

(b)

Figure 29: The mesh used for the P2D study showing the (a) the entire domain with the two refinement regions (black arrow with cell sizes of $0.02c$ and red arrow with cell sizes of $0.08c$) and (b) the near airfoil mesh showing the prism layers. For this example, the flow vector is parallel to the arrows in (a).

Results are shown in Figure 30a. This shows the coefficient of pressure as a function of the normalized chord length, x/c, at $\alpha = 4°$ and $\mathrm{Re} = 2 \times 10^5$ using the default turbulence intensity of 1%. The laminar separation and turbulent reattachment locations are also shown as solid lines on the same figure. The iterations were stopped when the C_L and C_D values differed less than 1% for the previous 50 iterations, or when the simulation reaches 1000 iterations at which time it would either have reached a steady state or constant oscillating frequency. The wake refinement length was decreased from $60c$ to $2c$ behind the airfoil changing the cell count of 1.7M to 430k with no change in the C_L and C_D values. This decrease in cell count did not affect results, but decreased the mesh size by 4, decreasing the computational time penalty. Considering the final objective of an optimization study which will run in the order of 500 simulations it was justified to keep the cell counts as low as possible, and the decision was made to continue using the wake refinement length of $2c$.

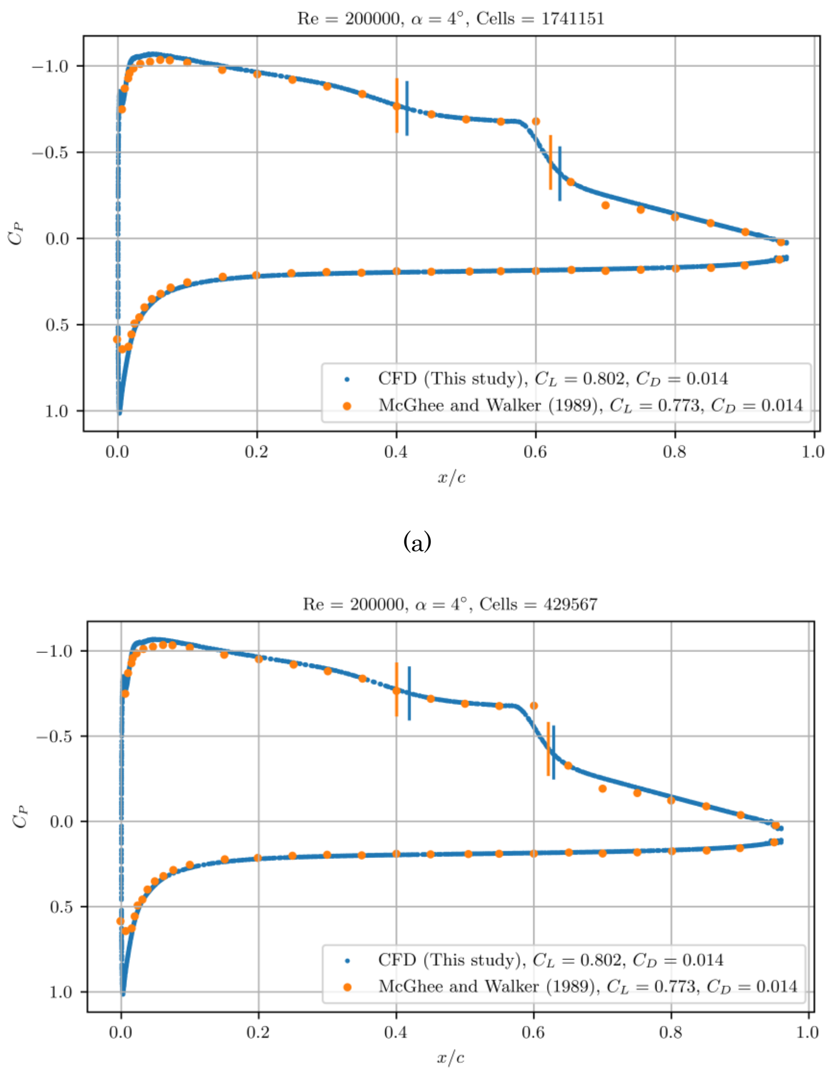

(a)

(b)

Figure 30: Results using (a) 60 chord lengths of wake refinement and (b) 2 chord lengths of wake refinement at $\alpha = 4°$ and $\mathrm{Re} = 2 \times 10^5$ showing the laminar separation and turbulent reattachment locations as solid lines.

The locations of the laminar separation and turbulent reattachment correlated well when considering that the experimental values for these quantities were determined using visual oil flow separation lines (McGhee and Walker, 1989). The difference between the obtained C_L and C_D was 4% and <1% respectively when compared to the experimental data. The pressure distributions around the airfoils also matched well, with one slight inaccuracy being the pressure increase through the adverse pressure gradient caused by the formation of the laminar separation bubble.

The effect of mesh refinement was investigated using the Richardson extrapolation (ASME, 2008). Relevant aerodynamic coefficients (in this case, C_L and C_D) were compared between three meshes of increasing cell count to see whether the solution obtained was mesh independent. The mesh convergence process is given in more detail in Appendix C and Appendix D. The type of prism layer mesh had to be changed to the advancing layer mesh which eliminated the collapsing cells at the trailing edge and the number of prism layers were reduced to 50. The aerodynamic coefficients are plotted against the cell counts in Figure 31.

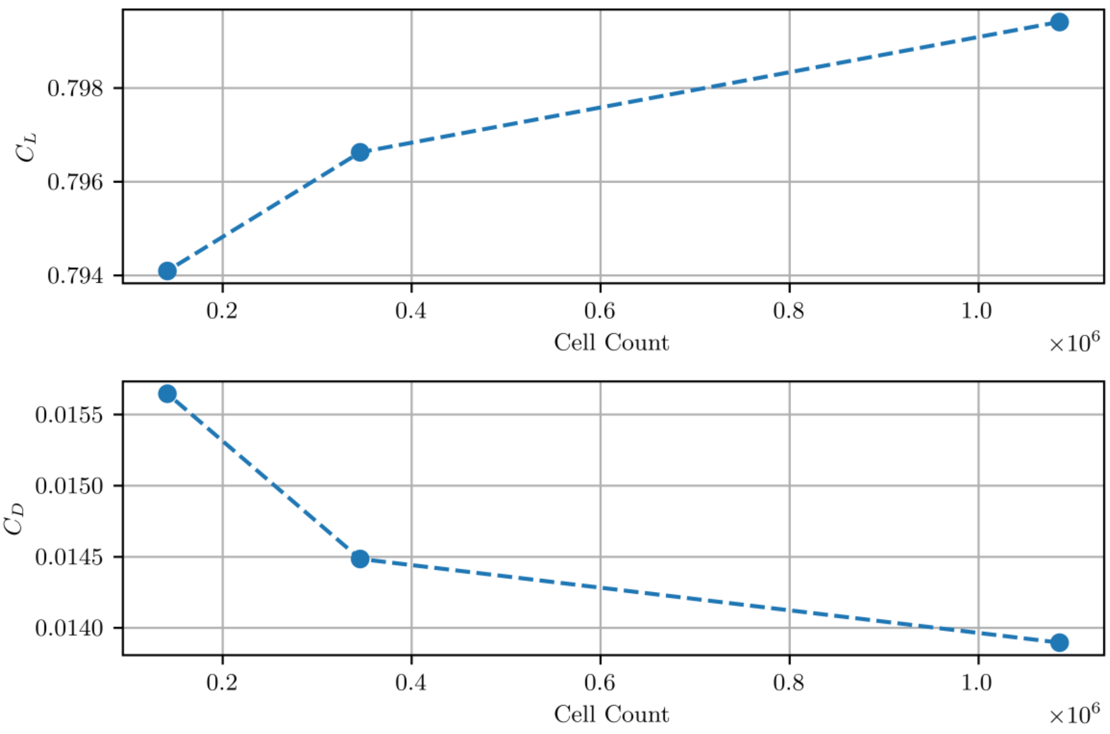

Figure 31: Change in C_L and C_D for the successive refinements

The lift and drag coefficients remained similar for the case where 1.1M cells were used and where 280k cells were used. This increase in cell size (and the computational time penalty) does not justify that the mesh is made larger than 280k cells.

4.2. Benchmark Results

An angle of attack sweep of $\alpha = 0°, 2°, 4°, 6°, 8°$ was done to further investigate the performance of the computational model used. Figure 32 shows C_L at different α and has less than 3% average difference between the CFD and experimental results. The CFD lift slope ($\Delta C_L/\Delta\alpha$) difference for the angles of attack between 0° and 6° is on average 1%, but for the range between 6° and 8° the CFD lift slope value is 30.4% less than that of McGhee and Walker (1989). The same figure shows the C_L at different C_D values, where there is a 2.8% average difference in drag slope ($\Delta C_D/\Delta\alpha$) of the CFD compared to the experimental results of McGhee and Walker (1989) between the angles of attack of 0° to 6° and 106.3%

difference between the angles of attack of 6° to 8°. This difference between the CFD and the experimental data of McGhee and Walker (1989) is acceptable and when looking at the difference between the McGhee and Walker (1989) data and the other two sets of data between the angles of 6° and 8°. This confirms the difficulty in experimentally modelling low Reynolds number flows. On Figure *32* the drag measurement of the CFD matched well with the experimental data of Althaus and Wortmann (1981) at the higher angles of attack (i.e., higher coefficients of lift).

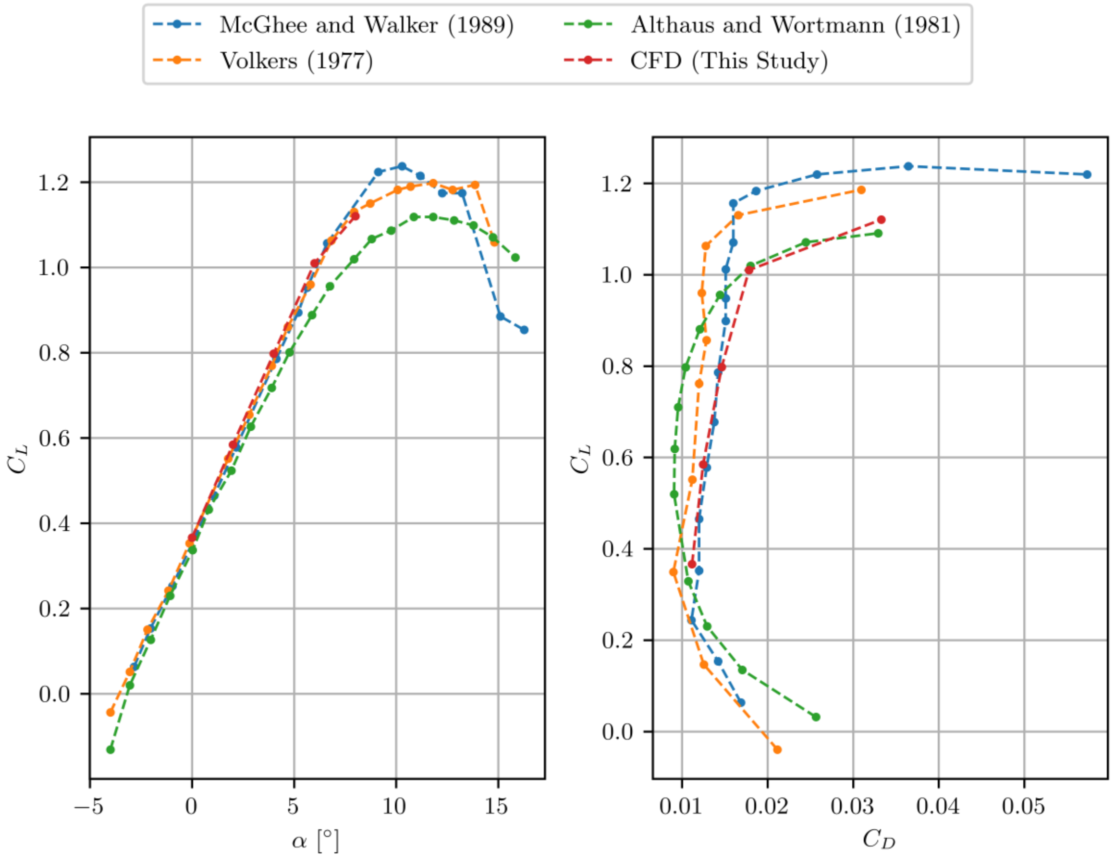

Figure 32: C_L and C_D results obtained for the angle of attack sweep for the E387 airfoil.

Figure 33 shows the C_P at x/c for various α, also showing the laminar separation and turbulent reattachment locations as predicted by the CFD and experimental data (using the blue and orange vertical lines; lines closer to the leading edge are laminar separation and points closer to the trailing edge are turbulent reattachment). The laminar separation and relocation locations were extracted by looking at the x/c location where the value of C_F is less than 1×10^{-4} as well as a local minimum. The pressure distributions match the experimental data of McGhee and Walker (1989) sufficiently for angles of attack 0° to 6°. The pressure distribution for α = 8° obtained using CFD underpredicts the suction on the top surface of the airfoil, which explains the underpredicted C_L for the CFD. This is due to the natural separation occurring at this angle of attack and the difficulty modelling this type of separated flow. For all the other angles of attack it is seen that the only region of an incorrectly predicted pressure is in the region where the LSB exists. The adverse pressure gradient is underpredicted in the CFD and is the cause for the overpredicted C_L values for α = 0° to α = 6°.

Figure 34 shows the laminar separation and turbulent reattachment locations at various angles of attack (omitting α = 8° due to the natural separation) compared to McGhee and Walker (1989) and Shen et al. (2017). Solid lines indicate the laminar separation and dashed lines indicate the turbulent reattachment. The laminar separation locations obtained using CFD differed on average by -3.6% and -0.4% and the turbulent reattachment location differed on average by -0.3% and 3.4% compared to Shen et al. (2017) and McGhee and Walker (1989) respectively. The trend of the laminar separation and turbulent reattachment locations moving toward the leading edge of the airfoil as the angle of attack increases, was similar between the CFD and the experimental data used. The separation locations for the CFD were obtained by locating the x/c corresponding to the lowest value of C_F on the airfoil (excluding stagnation points).

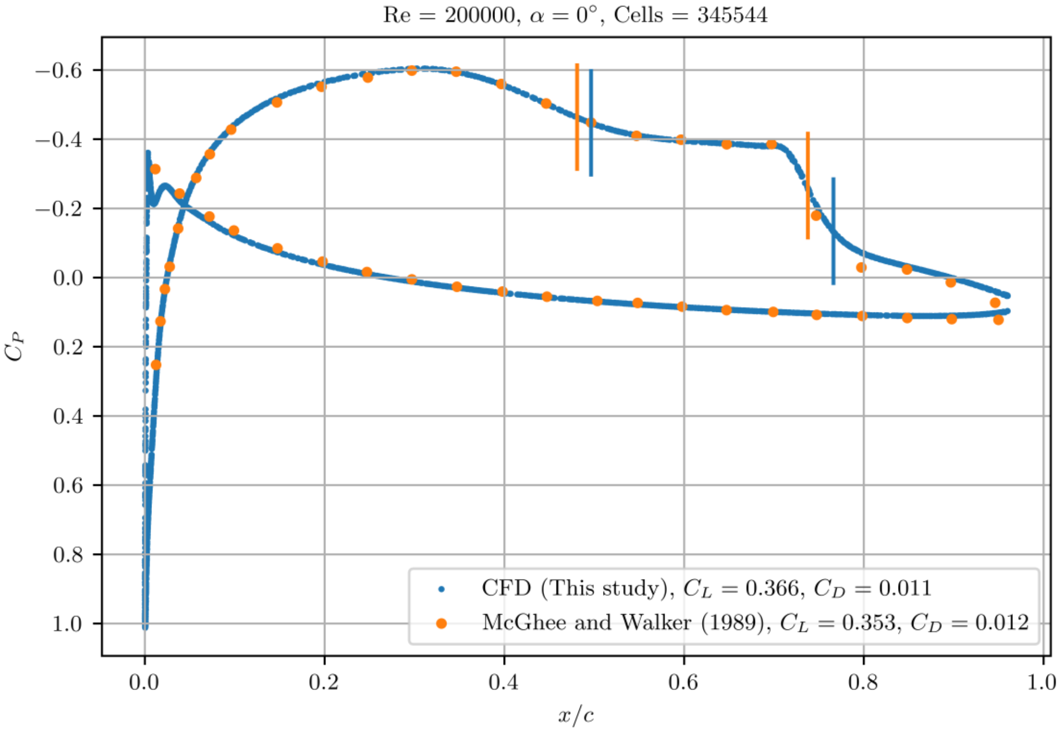

(a)

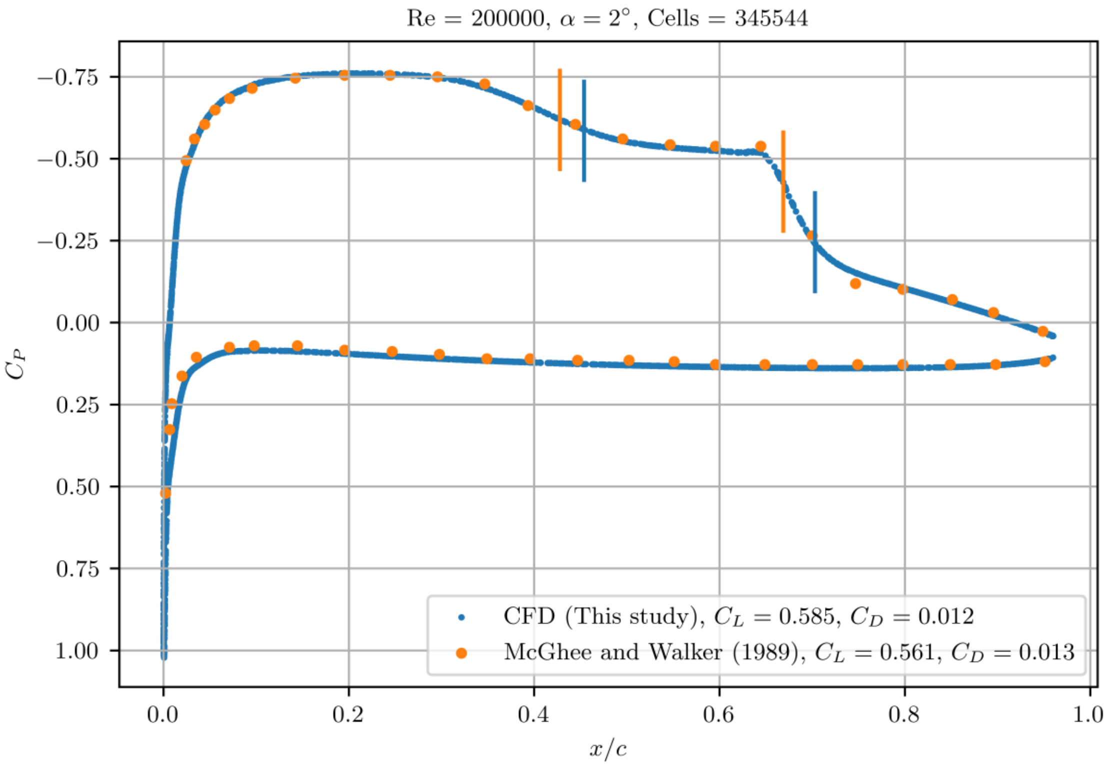
Re = 200000, $\alpha = 2°$, Cells = 345544
C_P
−0.75
−0.50
−0.25
0.00
0.25
0.50
0.75
1.00
0.0
0.2
0.4
0.6
0.8
1.0
x/c
CFD (This study), $C_L = 0.585$, $C_D = 0.012$
McGhee and Walker (1989), $C_L = 0.561$, $C_D = 0.013$

(b)

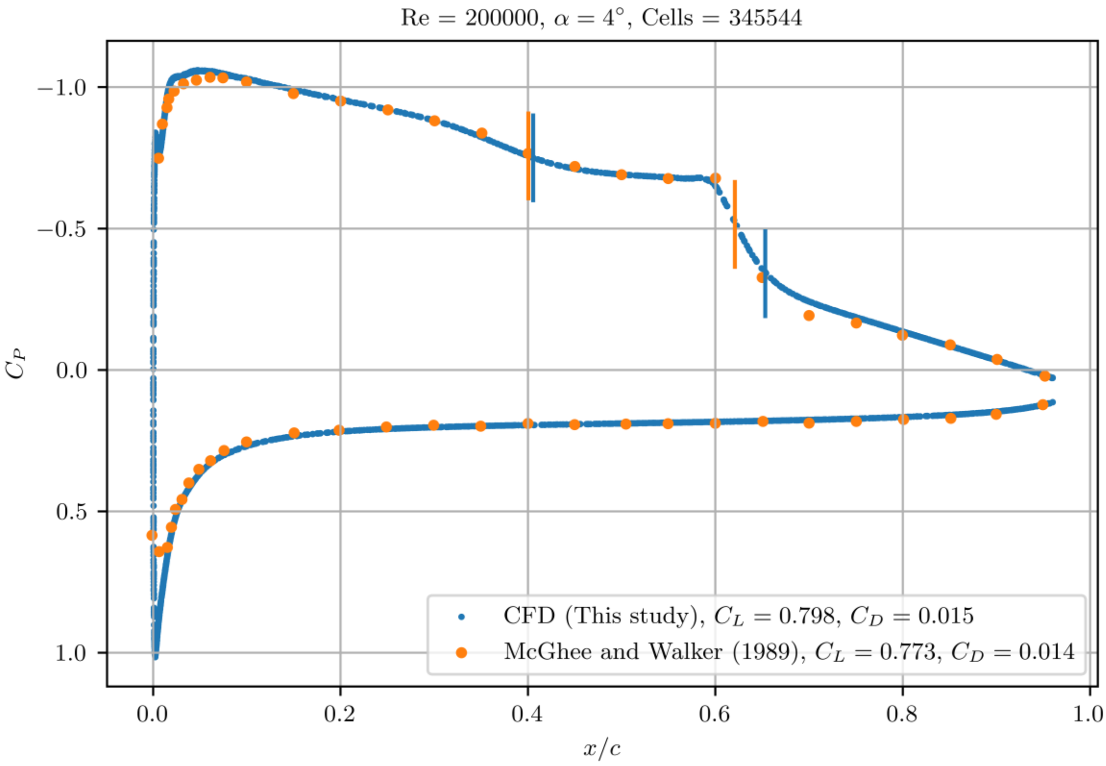
Re = 200000, $\alpha = 4°$, Cells = 345544
C_P
−1.0
−0.5
0.0
0.5
1.0
0.0
0.2
0.4
0.6
0.8
1.0
x/c
CFD (This study), $C_L = 0.798$, $C_D = 0.015$
McGhee and Walker (1989), $C_L = 0.773$, $C_D = 0.014$

(c)

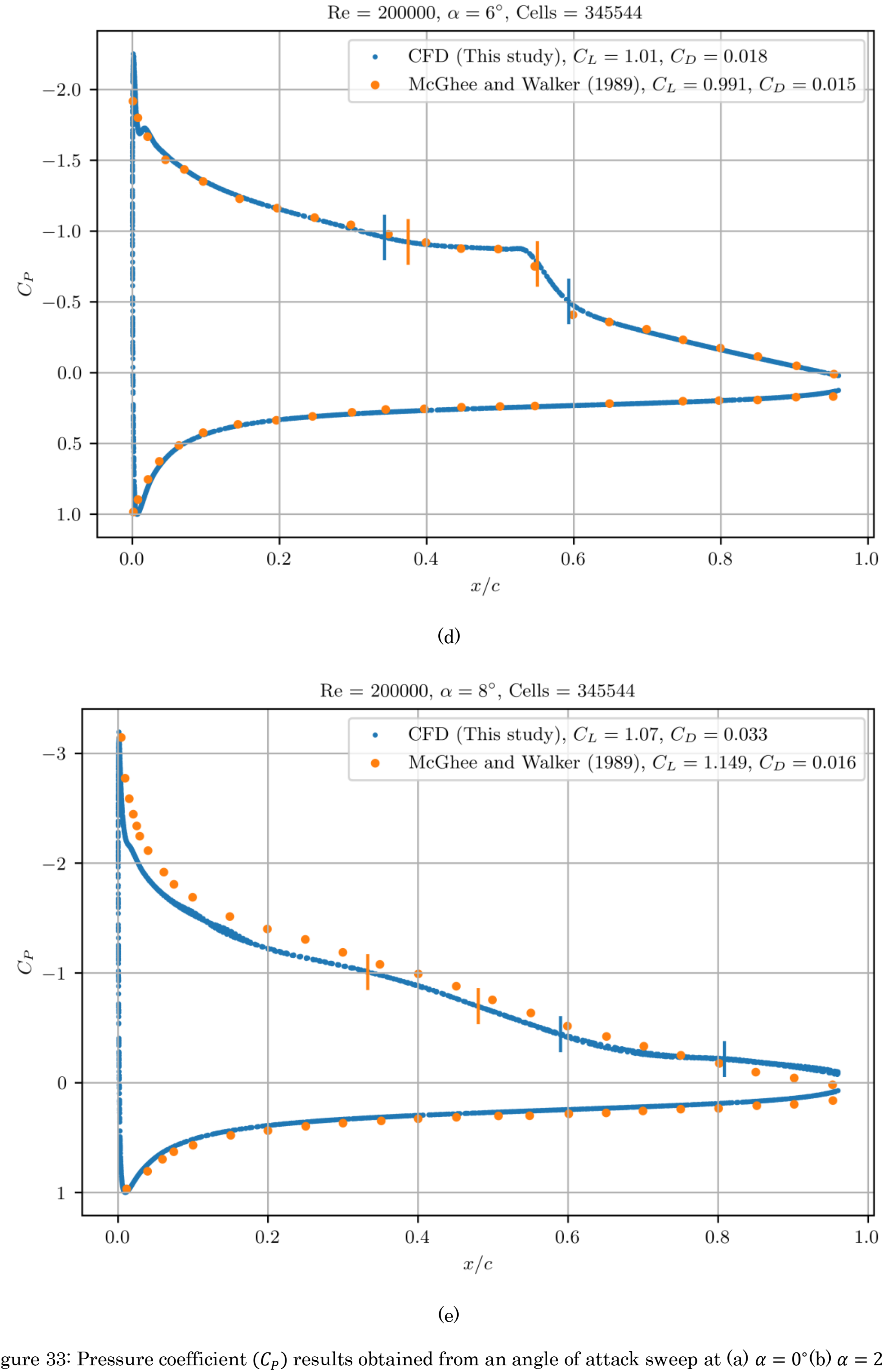

(d)

(e)

Figure 33: Pressure coefficient (C_P) results obtained from an angle of attack sweep at (a) $\alpha = 0°$(b) $\alpha = 2°$ (c) $\alpha = 4°$ (d) $\alpha = 6°$ (e) $\alpha = 8°$using the advancing layer mesher, compared to result obtained by McGhee and Walker (1989). The laminar separation and turbulent reattachment locations are shown as solid lines.

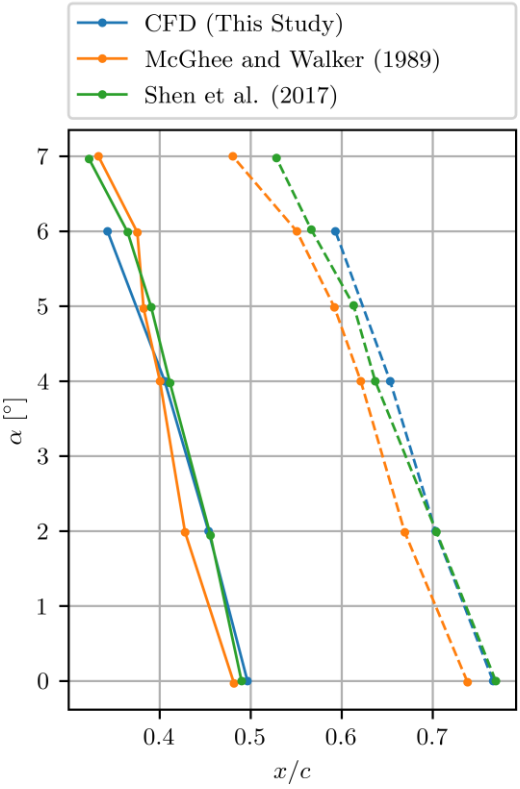

Figure 34: Laminar separation (solid lines) and turbulent reattachment (dashed lines) locations as the angle of attack changes compared to experimental results in the literature.

The results were acceptable for the purposes of this study when considering the findings of Tank et al. (2017). In this study it was proved that low Reynolds number flows over wings are notoriously difficult to model and measure using numerical and experimental methods and results are sensitive to geometry, environment, and numerical modelling techniques. The discrepancies between the three different sets of data further prove this point.

4.3. Meshing refinement strategy for optimization of different geometries

In the optimization study, airfoils with different geometries will be created using the PARSEC method. Knowing the "global" mesh settings, such as prism layer thickness, surface cell sizes etc., the effect of different geometries now had to be accounted for. This means that the same meshing strategy should be applicable to an airfoil such as the E387 and an airfoil such as that shown in Figure 26.

This refinement strategy is validated using two different airfoils. The E387 and the S1223 airfoils were simulated using the same meshing strategy, Reynolds number and angles of attack. The results were compared to experimental results available in the literature [E387: McGhee and Walker (1989); S1223: Selig and Guglielmo (1997)].

Adaptive mesh refinement (AMR) is a built-in model in STAR-CCM+ and it was used to refine or coarsen the initial mesh based on functions coded by the user. The function used for the refinement was the Laplacian of the total pressure, given as

$$\nabla^2 P_0 = \frac{\partial^2 P_0}{\partial x^2} + \frac{\partial^2 P_0}{\partial y^2} \tag{18a}$$

where the total pressure, P_0, was calculated as

$$P_0 = P + \frac{1}{2}\rho V^2 \tag{18b}$$

To account for cells of varied sizes, the function used was the Laplacian of the total pressure multiplied by the adaptation cell size squared, giving

$$\nabla^2 P_0 \cdot \Delta x^2 \tag{18c}$$

where Δx^2 can be thought of as the cell area. The adaption cell size indicates the current cell size in the volume mesh. Specifically, it is calculated as double the maximum distance between the cell centroid and any vertex of the cell and can be thought of as the diameter of a sphere enclosing a specific cell.

The bounds for the adaptive mesh refinement were manually tuned, and it was found that bounds of [10Pa,15Pa] were adequate to refine cells which were expected to be refined. Cells were refined when the scalar value shown in equation (18c) is above 15Pa, coarsened below 10Pa and kept as is between these two values. The maximum refinement level was set to 2, meaning that each polyhedral cell could successively only be refined twice. AMR uses midpoint subdivision to create refined cells. The midpoint subdivision of a polyhedral cell typically results in 12-15 child cells. The exact number of child cells is equal to the number of vertices present in the parent cell.

The mesh generated for the E387 at an angle of attack α = 8° is shown in Figure 35 as an example. The cells in the wake region of the airfoil were refined by the adaptive mesher to approximately 3.5c downstream. The decision was also made to manually increase the cell size of the wake and increase the length of the wake refinement to 20c with a cell size of 0.08c since it was expected that the AMR would refine cells where necessary.

The advancing layer mesh (boundary layer cells) is shown in Figure 35c and it is seen that the prism layer cells wrap around the trailing edge, eliminating the collapsing cell phenomena associated with the standard prism layer mesher. The cells inside the advancing layer mesh cannot be adaptively refined. The final mesh increased from 270k to 350k after implementing the adaptive mesh refinement.

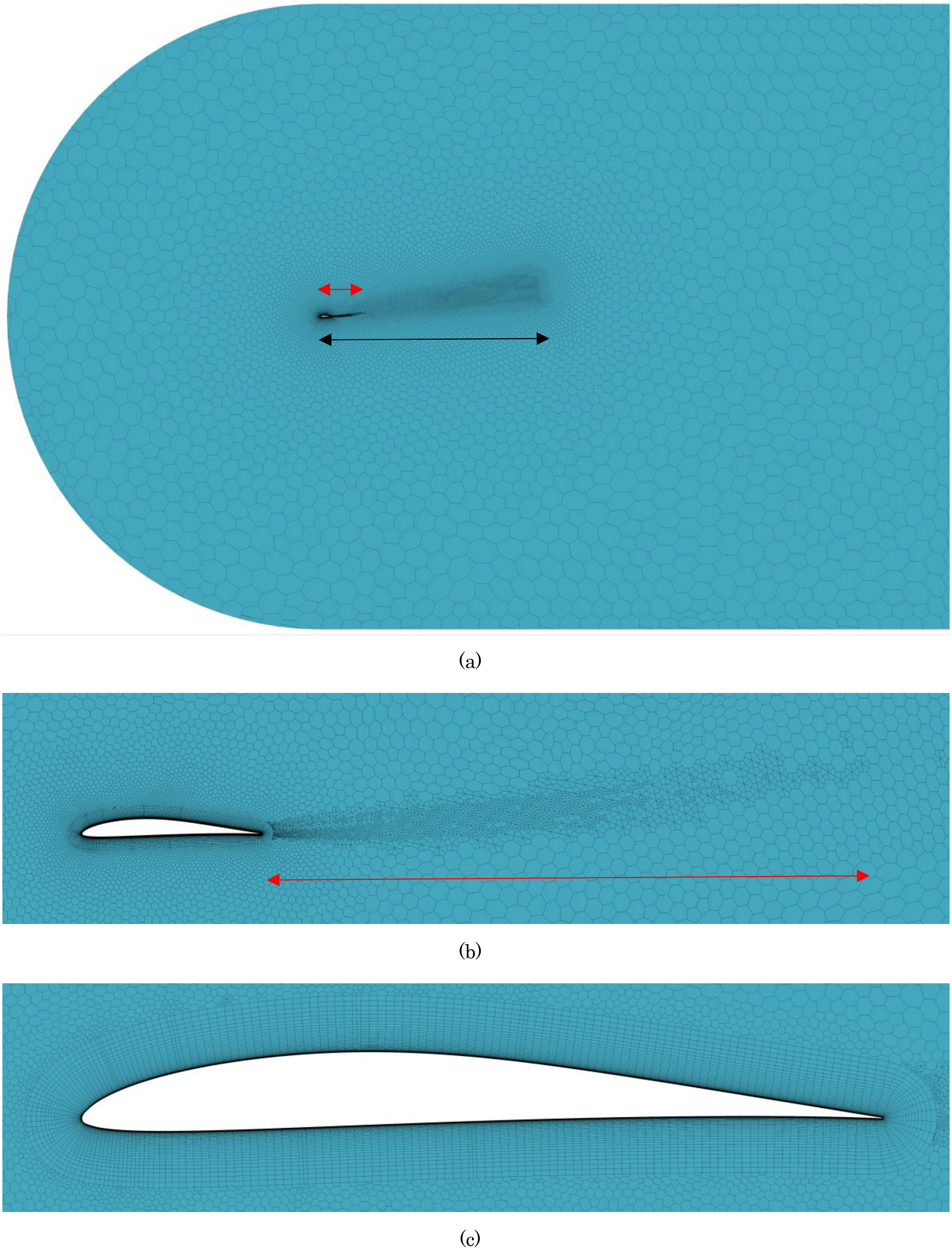

Figure 35: The mesh generated and adaptively refined using the AMR technique discussed above for $\alpha = 8°$. The black arrow shows the $20c$ wake refinement done manually, and the red arrow shows the region where the mesh was adaptively refined.

Figure 36 provides an overview of the results. The simulated C_L values for the unsteady solver correlated well, with an average error of 4% to the experimental data. The C_L vs α plot shows the lift might be overestimated for α = 8° but the C_L vs C_D trends correlated well with McGhee and Walker (1989). The average difference between the CFD with AMR and the results from McGhee and Walker (1989) regarding the C_D vs C_L plot was on average 7.4%. When AMR was not used the C_L error was 3% and the C_D error was 17.6%. It is evident that AMR is therefore better suited to predict the C_D.x

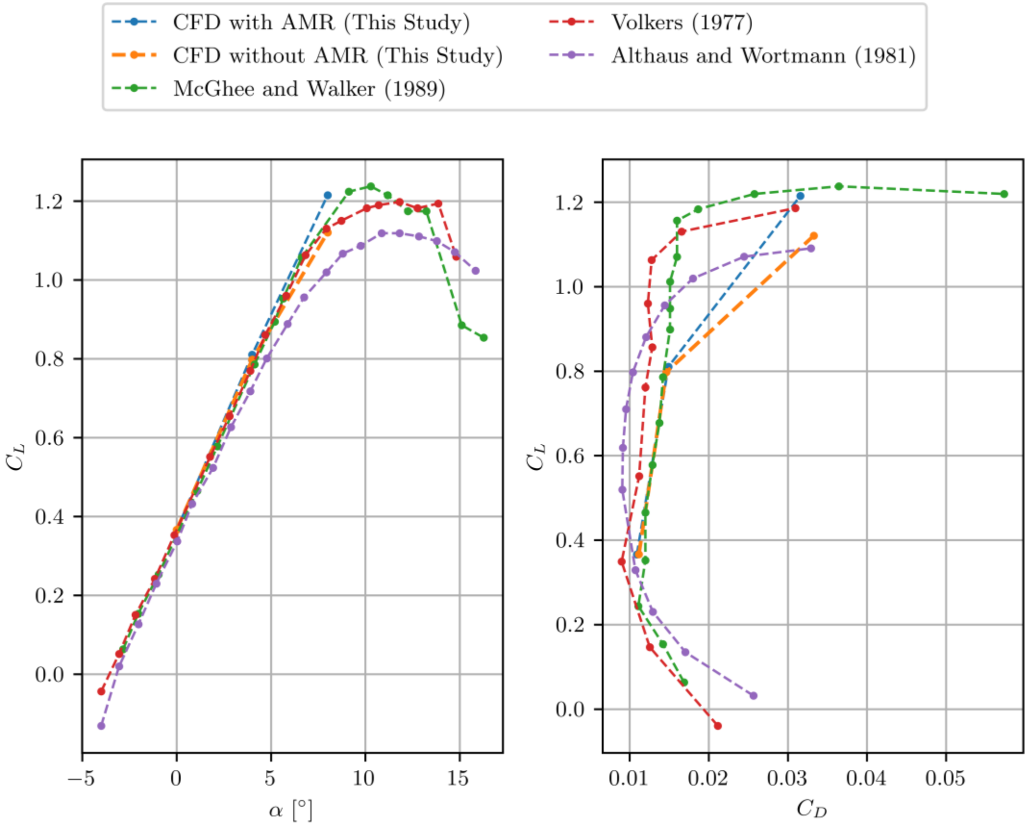

Figure 36: C_L and C_D as function of α.

Figure 37 shows the coefficient of pressure results for three angles of attack, namely $\alpha = [0°, 4°, 8°]$. The mesh was visually inspected, and it was found that the adaptively refined regions of the mesh were as expected (i.e., in the wake of the airfoil at almost the same angle as the angle of attack used). The coefficient of pressure plots indicates the laminar separation and turbulent reattachment locations using solid lines. The lines toward the left are the laminar separation locations and the lines to the right are the turbulent reattachment locations. There was no separation and reattachment for α = 8°. The simulation with AMR for α = 8° had a closer resemblance to the experimental data. The only other difference was the pressure increase through the adverse pressure gradient at $x/c = 0.75$.

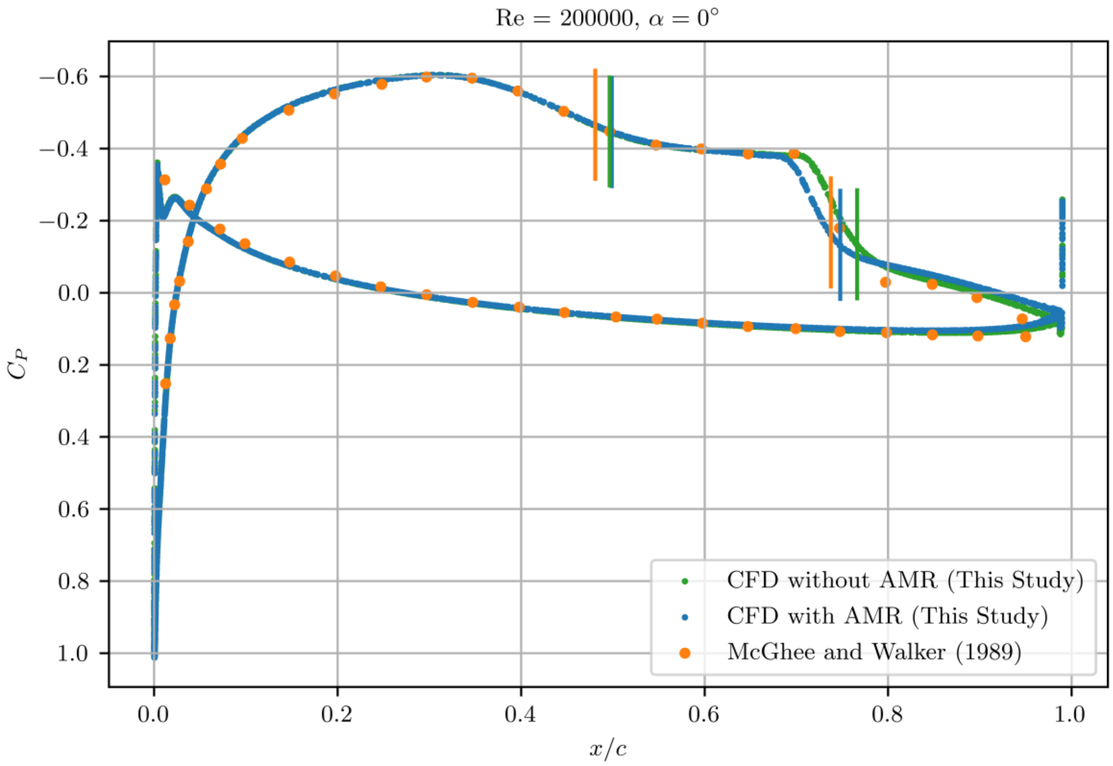
Re = 200000, $\alpha = 0°$
C_P
−0.6
−0.4
−0.2
0.0
0.2
0.4
0.6
0.8
1.0
0.0
0.2
0.4
0.6
0.8
1.0
x/c
CFD without AMR (This Study)
CFD with AMR (This Study)
McGhee and Walker (1989)

(a)

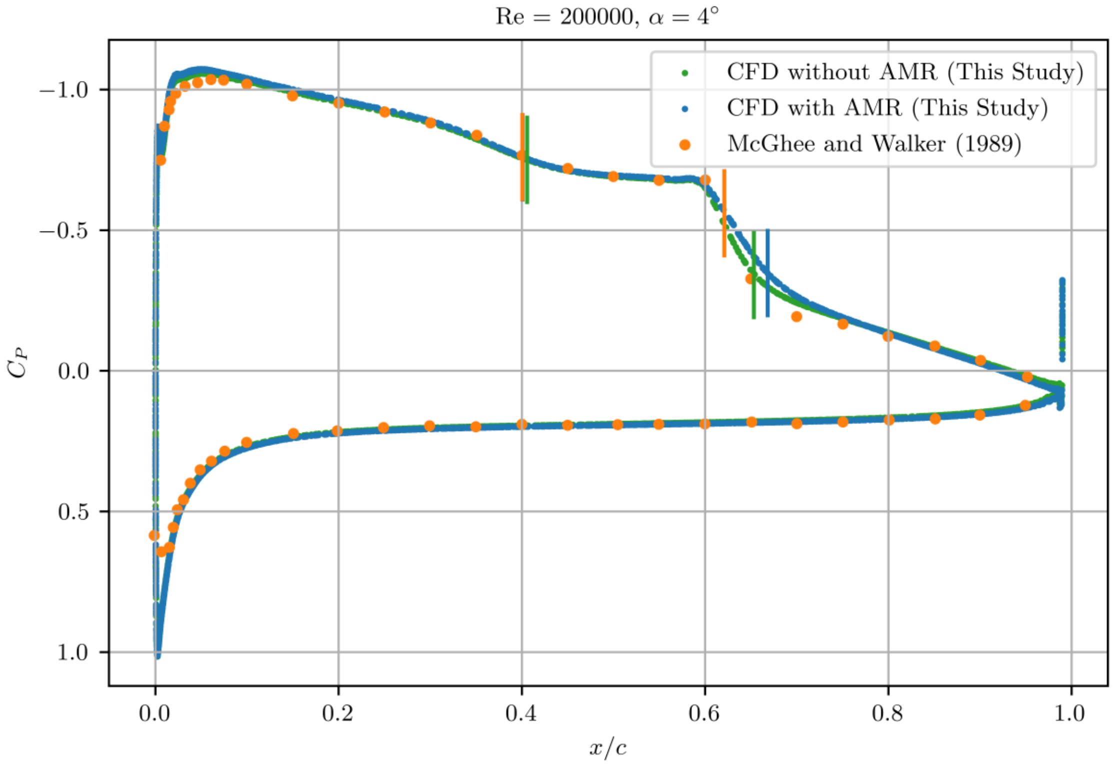
Re = 200000, $\alpha = 4°$
C_P
−1.0
−0.5
0.0
0.5
1.0
0.0
0.2
0.4
0.6
0.8
1.0
x/c
CFD without AMR (This Study)
CFD with AMR (This Study)
McGhee and Walker (1989)

(b)

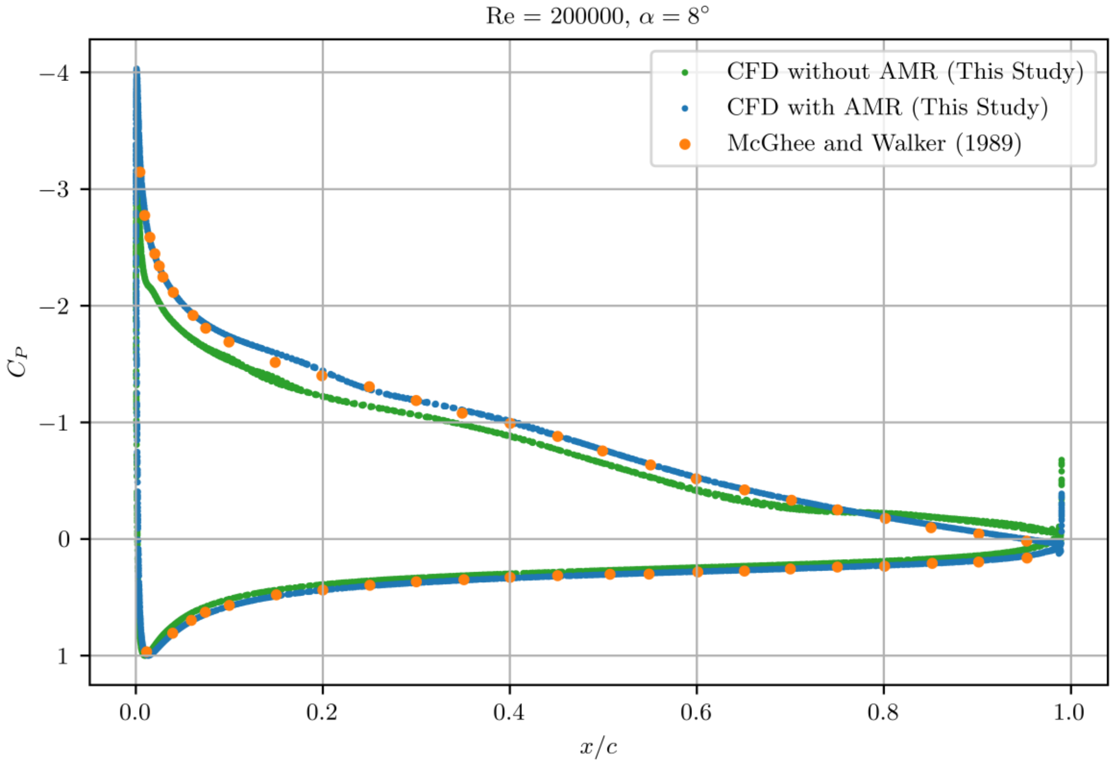

(c)

Figure 37: The coefficient of pressure results for the E387 using AMR compared to results from the literature fore (a) $\alpha = 0°$ (b) $\alpha = 4°$ (c) $\alpha = 8°$. The vertical blue and orange lines indicate the laminar separation and turbulent reattachment locations on the airfoil. The blue lines indicate the locations of this study, and the orange lines indicate the locations of McGhee and Walker (1989).

The next airfoil was the S1223, developed for low Reynolds number flows ($\text{Re} = 1 \times 10^5$ to $\text{Re} = 3 \times 10^5$). The airfoil features a much higher camber than the E387. The purpose of this evaluation was to estimate the AMR's capability to solve the correct flow field by meshing regions where higher gradients were expected.

It was observed that steady RANS simulations exhibited highly oscillatory results, as shown in Figure 38. If the solver was switched to URANS, the results converged asymptotically toward the final value. The mean values of the oscillating aerodynamic coefficients were almost equal to those obtained using an unsteady solver for $\alpha = 0°$ and $\alpha = 4°$, except for $\alpha = 8°$. The URANS simulations took on average 5 times longer to converge than the steady RANS simulations that has reached a steady state oscillation.

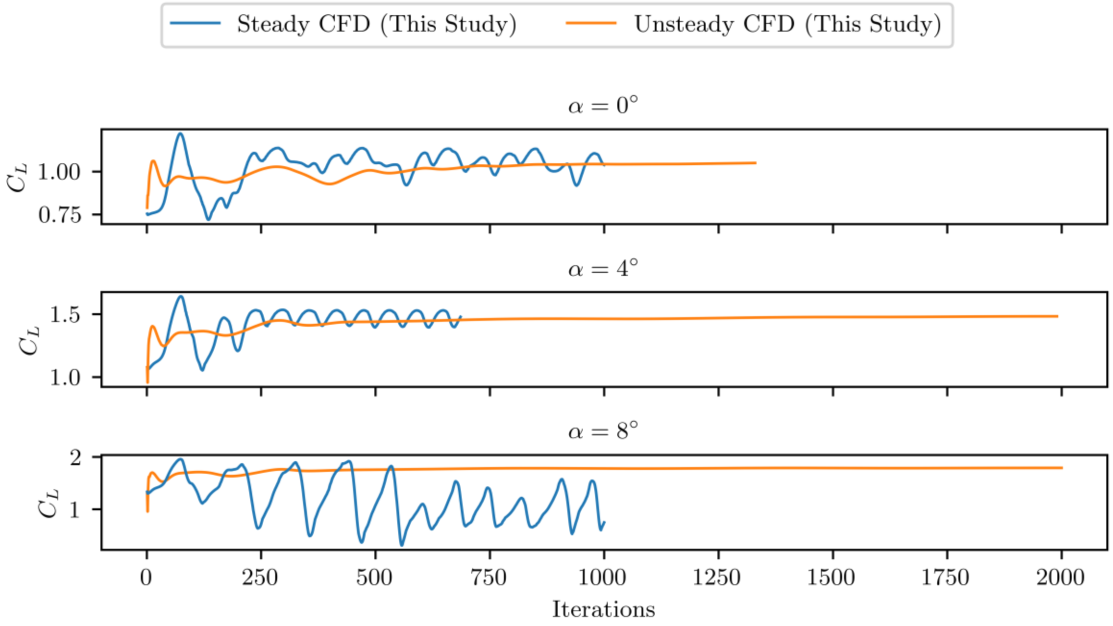

(a)

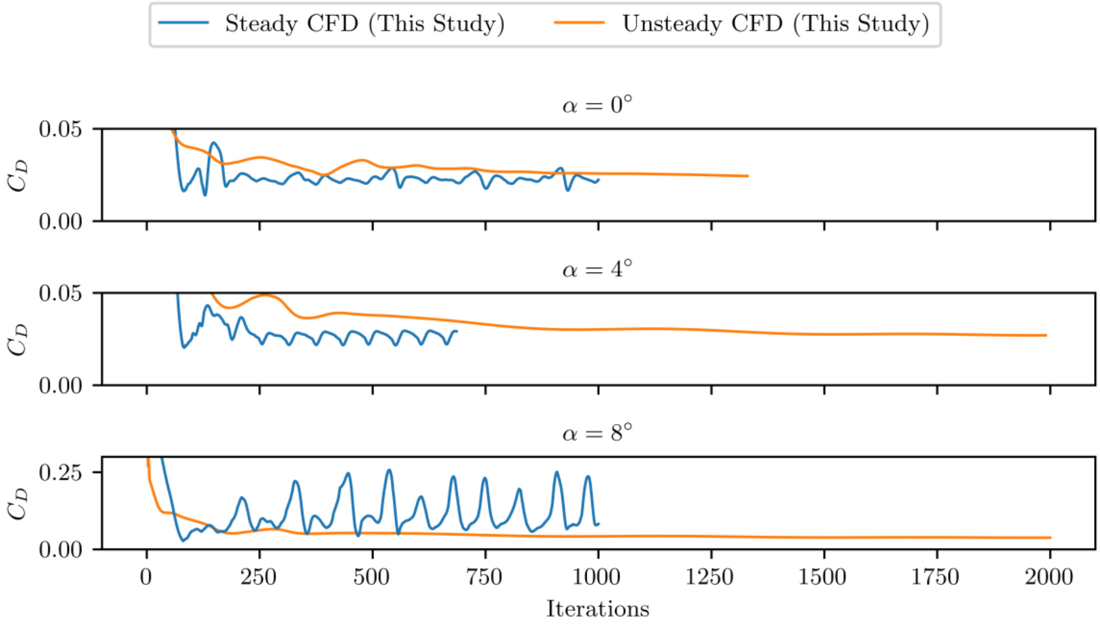

(b)

Figure 38: (a) C_L and (b) C_D plotted against the number of iterations comparing the steady and unsteady solver.

The unsteady effects were due to cyclically growing and bursting laminar separation bubble (LSB) on the suction side of the S1223 airfoil at higher angles of attack, as shown in Figure 39. In this specific example, the steady result is taken at the instance where the LSB has burst and has been detached from the top surface of the airfoil.

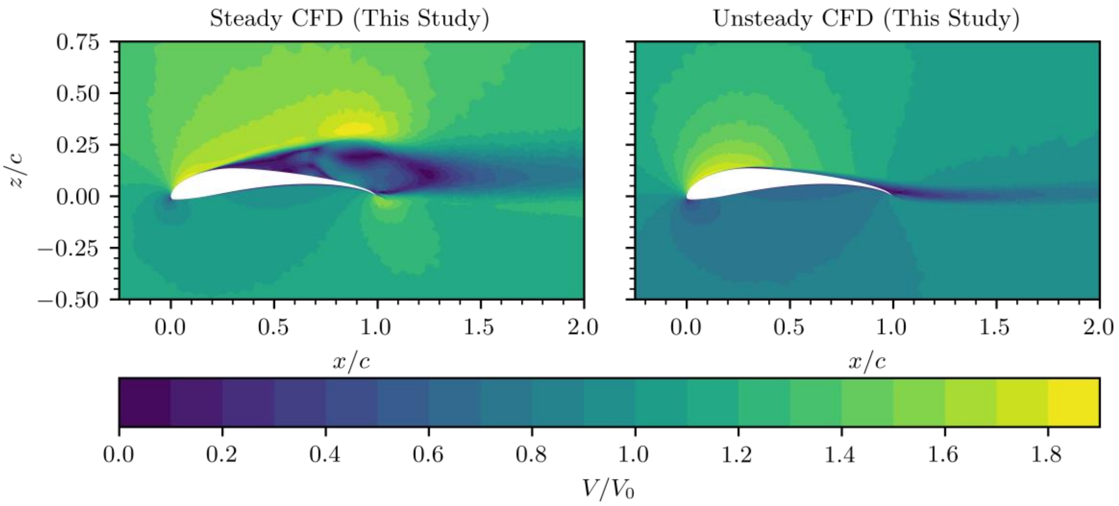

Figure 39: Normalized velocity magnitude contour plot comparing the steady and unsteady solver at Re = 2×10^5 and $\alpha = 8°$ for the S1223.

Figure 40 shows the C_L and C_D polars for the S1223, comparing the different solvers to values obtained experimentally by Selig and Guglielmo (1997) and with XFOIL, which yields rapid results that can act as an estimation of the expected values. The XFOIL computations were done on the same airfoil (S1223) at $\alpha = 4°, 6°, 8°$ for Re $= 2 \times 10^5$. A viscous analysis using the default $N_{\text{crit}} = 9$ value is used to trigger boundary layer transition. The steady solver C_L absolute average error for $\alpha = 0°$ and $\alpha = 4°$ is within 2% (maximum of -2.2%) and C_D within 10.2% (maximum of 10.9%) but for $\alpha = 8°$ the C_L error is 70% lower and C_D is 400% higher than expected. The C_L predicted using the unsteady solver differed on average by -0.2% (maximum of 3.6%) and the C_D on average differed by 16% (maximum of 20%) from the experimental results. In practice, if higher angles of attack are considered the unsteady solver should be used for more reasonable predictions.

The results obtained for the S1223 airfoil were consistent with conclusions from Carreño Ruiz and D'Ambrosio (2022), stating that results obtained for higher angles of attack were more accurate using an unsteady solver. Typically, airfoils at these angles have bursting LSB that allow URANS to better predict the fluid behaviour. The findings were consistent with Pauley et al. (1990) in which it was shown that a time-averaged solution using RANS produces a closed separation bubble, like that obtained when using URANS.

The steady RANS solver is used in the optimization due to the drastic time increase associated when using the unsteady solver. However, the final optimized airfoil will be evaluated using URANS to ensure any oscillatory behaviour is captured.

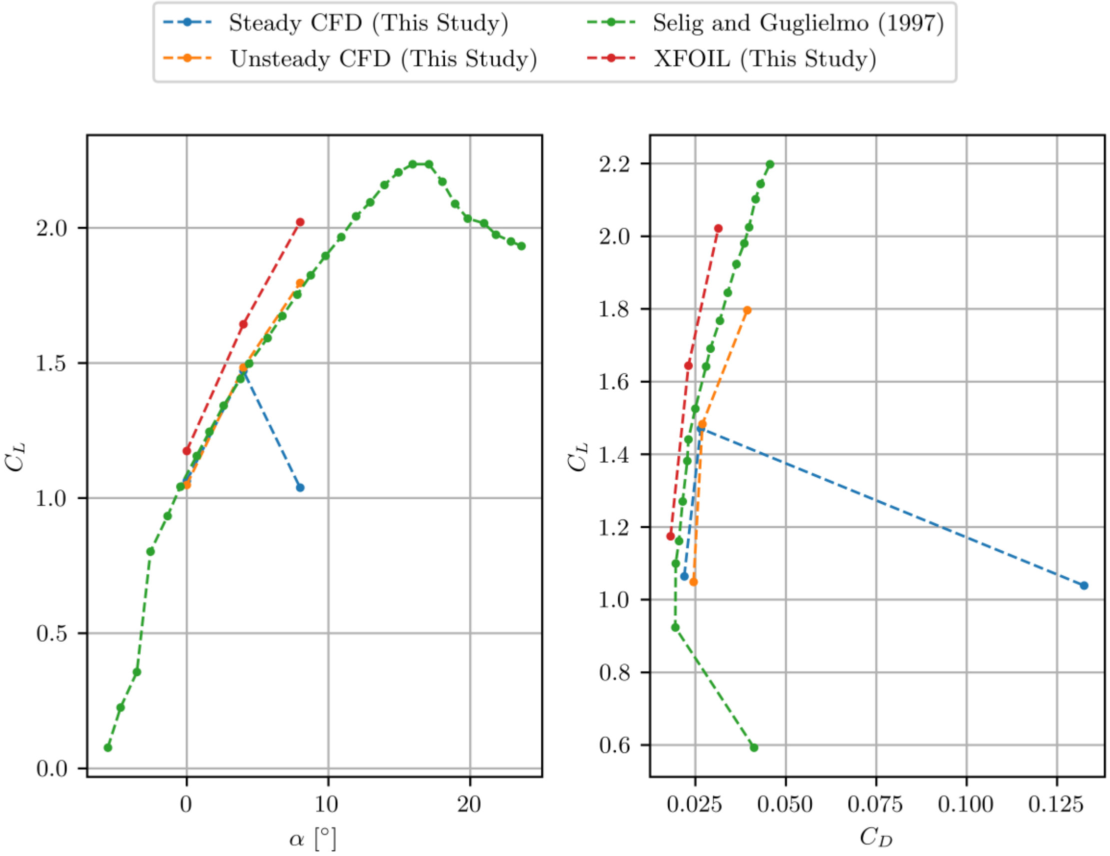

Figure 40: C_L, C_D as function of α compared to results obtained from XFOIL and Selig and Guglielmo (1997).

5. Aerodynamic Optimization of the Parametric model

5.1. The Parametric model of the Grey-headed Albatross

STAR-CCM+ makes use of global parameters that take any value and unit the user allocates to it. A global parameter was created for each PARSEC parameter in the simulation file (remembering that the 12 PARSEC parameters control the geometry of the airfoil). This simulation file was then used inside the STAR-CCM+ Design Manager to choose new values for following simulations based on the optimization algorithm output.

First, each PARSEC parameter was extracted from the simulation and saved as a double-precision floating point value. These values were used to create the 6 × 6 matrices, and the column vector on the right-hand side in equations (9) and (10). The column vector containing the coefficients a_n and b_n was calculated using the *Jama* package. The Z_{upper} and Z_{lower} distributions were calculated using equations (11) and (12), with an x distribution calculated using equation (17). The Z_{upper} and Z_{lower} values and the x values were multiplied with the chord length (0.2m) and appended to an open *.csv* file. A final column containing values of $y = 0$ was added to save and close a *.csv* file with three columns forming 101 ordered (x, y, z) coordinates. The same approach was followed in the Python program as in Section 3.2.

5.2. Calculating the Design Space

Typically, in airfoil design, the PARSEC parameterization did not describe a method used to assign upper and lower bound parameters. In this work, careful consideration of the design space led to two limiting factors regarding these parameters. First, the biological limitations of a cross section of the wing, i.e., certain geometries are just not physically possible due to the skeletal and structural properties of the bird. Second, the mathematics which govern the geometry of an airfoil created by the PARSEC method to produce feasible geometries.

Self-intersecting geometry was a problem associated with design spaces that were too large. An intuitive example of this is the case where $Z_{\text{up}} \leq Z_{\text{lo}}$ for $X_{\text{up}} \simeq X_{\text{lo}}$, demonstrated in Figure 41. This would inevitably cause the top and bottom surface of the wing to intersect.

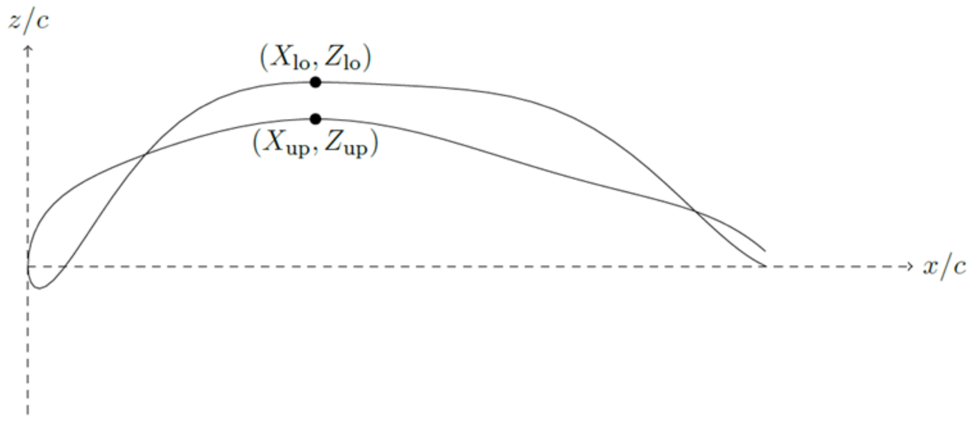

Figure 41: An airfoil showing the self-intersecting geometry caused when $Z_{\mathrm{up}} \leq Z_{\mathrm{lo}}$ for $X_{\mathrm{up}} \simeq X_{\mathrm{lo}}$

There are many other combinations of parameters that cannot be used together. To determine these combinations, two approaches can be taken. The first approach is to deduct the bounds and interdependencies between the parameters using equations (9) through (12), to determine the allowable ranges for each parameter. The simplest parameter constraint can be demonstrated by the following. A viable airfoil is when,

$$\boldsymbol{z}_{\mathrm{upper}} > \boldsymbol{z}_{\mathrm{lower}} \tag{19a}$$

for all points, $x_i \in x = [x_1, x_2, \dots, x_k]$. Considering a single point, this is rewritten as,

$$\sum_{n=1}^{6} a_n \, x_i^{n-\frac{1}{2}} > \sum_{n=1}^{6} b_n x_i^{n-\frac{1}{2}} \tag{19b}$$

from equations (11) and (12) and expanded as,

$$a_1 x_i^{\frac{1}{2}} + a_2 x_i^{\frac{3}{2}} + \cdots + a_6 x_i^{\frac{11}{2}} > b_1 x_i^{\frac{1}{2}} + b_2 x_i^{\frac{3}{2}} + \cdots + b_6 x_i^{\frac{11}{2}} \tag{19c}$$

which is seen to be exactly the second equations in (9) and (10) if $x_i = X_{\mathrm{lo}} = X_{\mathrm{up}}$. Therefore,

$$Z_{\mathrm{up}} > Z_{\mathrm{lo}} \tag{19d}$$

This example demonstrates a single case in which a constraint on the parameters is calculated. Calculating additional constraints are challenging due to the nonlinear nature of equations (9) through (12). The coefficients a_n and b_n where $n = 1,2, \dots, 6$ can in no possible way be written in an explicit analytic form where $a_n = f\left(X_{\mathrm{up}}, Z_{\mathrm{te}}, \dots, r_{\mathrm{le,\,up}}\right)$, and similarly, for b_n. This led to the second method of calculating the design space which was to use statistical methods.

Using the PARSEC parameters for the arm and hand section shown in Table 4, respectively, bounds were inferred by adding and subtracting a certain percentage, δ, from the base design. This value was initially chosen as 50%. The upper and lower bounds were then calculated as,

$$\boldsymbol{P}_l = \boldsymbol{P}_0 - \delta|\boldsymbol{P}_0| \tag{20a}$$

and

$$\boldsymbol{P}_u = \boldsymbol{P}_0 + \delta|\boldsymbol{P}_0| \tag{20b}$$

where $\boldsymbol{P}_l$ and $\boldsymbol{P}_u$ are the lower and upper bounds for the PARSEC parameters, $\boldsymbol{P}_0$ is the baseline parameters from Table 4 and δ is the increment, set to 50%. Latin hypercube sampling was used to determine the success rate for the specific lower and upper bounds. A Latin hypercube sample generates n designs between $[0,1)^d$ where d denotes the number of dimensions associated with the problem. It was obvious that the PARSEC parameters used did not range between 0 and 1, but between the lower and upper bounds calculated according to equations (20). Therefore, the following transform was used.

$$(b - a) \times \text{sample} + a \tag{21}$$

where a and b are the upper and lower bounds. For example, let $d = 2$ and $n = 5$, the sample can look as follows.

$$\text{sample} = \begin{bmatrix} 0.09 & 0.01 \\ 0.72 & 0.24 \\ 0.47 & 0.89 \\ 0.34 & 0.60 \\ 0.80 & 0.49 \end{bmatrix}$$

And now scaled between the values of 1 and 10 for the first variable and 5 and 50 for the second.

$$\text{sample} = \begin{bmatrix} 1.85 & 5.07 \\ 7.55 & 15.84 \\ 5.31 & 45.11 \\ 4.13 & 32.28 \\ 8.23 & 27.39 \end{bmatrix}$$

The first column of the Latin hypercube sample ranges exactly between 1 and 10, and the second column between 5 and 50, essentially mapping the initial Latin hypercube sample to a new sample with a different coordinate system. Previously, it was mentioned that a success rate will be determined. This success rate is simply calculated as,

$$\text{success rate} = 1 - \frac{n_{\text{failed}}}{n_{\text{total}}} \tag{22}$$

where n_{failed} and n_{total} are the number of failed designs and total number of designs respectively. A design is said to have failed if one of the following criteria is met,

$$z_{i,\text{upper}} \leq z_{i,\text{lower}} \text{ for any } x_i \text{ where } i \in [x_1, x_2, \dots, x_k] \tag{23a}$$

or

$$z_{i,\text{upper}} > Z_{\text{up}}\ for\ any\ x_i \text{ where } i \in [x_1, x_2, \dots, x_k] \tag{23b}$$

The STAR-CCM+ documentation for using the SHERPA algorithm states that the number of failed designs should not exceed 80%. Therefore, the bounds were expanded to values that kept the success rate above 80%. The Latin hypercube sample was generated by the *Quasi-Monte Carlo (qmc)* submodule in the *Stats* module from the *SciPy* library. The *LatinHypercube* function was used to generate 1000 designs with 12 dimensions scaled using equations (20) and (21). Each design was then used to generate an airfoil using the PARSEC method. The specific design was then flagged if it failed according to equations (23) and the parameters which were used was stored. The matrix containing all failed designs was investigated using statistical methods to determine which parameters or combinations of parameters were the cause of failure. The failure matrix, f, is shown to be,

$$\boldsymbol{f} = \begin{bmatrix} \boldsymbol{P}_1 \\ \boldsymbol{P}_2 \\ \vdots \\ \boldsymbol{P}_{\text{n, failed}} \end{bmatrix} \tag{24}$$

where,

$$\boldsymbol{P}_i = [r_{\text{le, lo}} \quad r_{\text{le, up}} \quad X_{\text{lo}} \quad X_{\text{up}} \quad Z_{\text{lo}} \quad Z_{\text{up}} \quad Z_{\text{xx, lo}} \quad Z_{\text{xx, up}} \quad \alpha_{\text{te}} \quad \beta_{\text{te}} \quad Z_{\text{te}} \quad \Delta Z_{\text{te}}]$$

$$\text{for } i = 1,2, \dots, n_{\text{failed}}$$

The data had to be normalized to obtain accurate statistical conclusions. The normalization method used was mean centering and scaling according to the standard deviation. Mean centering subtracts the mean of each column vector from the original column vector after which the data is scaled to have a standard deviation of 1. Consider a single column vector, $\boldsymbol{p} = [p_1, p_2, \dots, p_{n_{\text{failed}}}]$, of $\boldsymbol{f}$, which represents all values causing failure for any of the 12 PARSEC parameters from the failure matrix $\boldsymbol{f}$. The data is mean centered and scaled according to,

$$p_i' = \frac{p_i - \overline{p}}{\sigma}, \text{for } i = 1,2, \dots, n_{\text{failed}} \tag{25}$$

where $\overline{p}$ and σ represent the mean and standard deviation of p respectively. This was done to all 12 columns of $\boldsymbol{f}$, resulting in the centered and scaled failure matrix, $\boldsymbol{F}$. Next, the covariance matrix was calculated as

$$\boldsymbol{C} = \frac{\boldsymbol{F}^T\boldsymbol{F}}{n_{\text{failed}} - 1} \tag{26}$$

The covariance matrix is a 12 × 12 square matrix and aided in showing the covariance between two independent observations and it pointed out which PARSEC parameters could cause failure. The investigation into the actual determination of the design space is given in Appendix F, showing that the design space created could achieve the 80% success rate whilst incorporating the biological limitations of the GHA wing.

The optimization of an airfoil is expected to behave like that shown by Nachtigall and Wieser (1966). The morphing of an airfoil in the presence of airflow is studied on a Pigeon wing at different angles of attack and airspeeds. Figure 42 shows the trailing edge location, which is represented as Z_{te} in this study, shifted vertically upwards. This movement of the trailing edge “decreased” the true angle of attack the airfoil experiences.

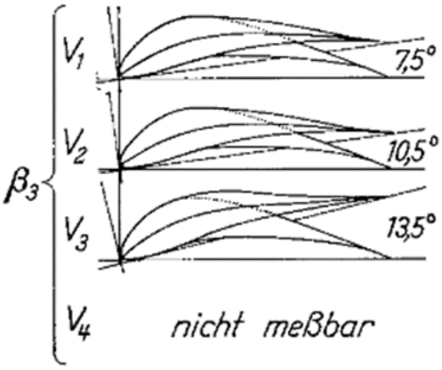

Figure 42: Pigeon wings at $V_1 = 5\text{ms}^{-1}$, $V_2 = 7.5\text{ms}^{-1}$, $V_3 = 10\text{ms}^{-1}$ at a constant angle of attack of $\alpha = 10°$ (Nachtigall and Wieser, 1966).

It was therefore important to ensure that the bounds were adequate to capture these types of morphed airfoils. This was done by simply estimating what the airfoil might look like under an aerodynamic load. An estimation of this is shown in Figure 43, together with the airfoil created using the PARSEC parametrization and having the bounds set to those developed earlier. The accurate matching between the hypothesised airfoil (an airfoil with a lifted trailing edge in Figure 42) and the airfoil created by the PARSEC method proved that the kind of morphing under an aerodynamic load can be accurately captured within the set bounds.

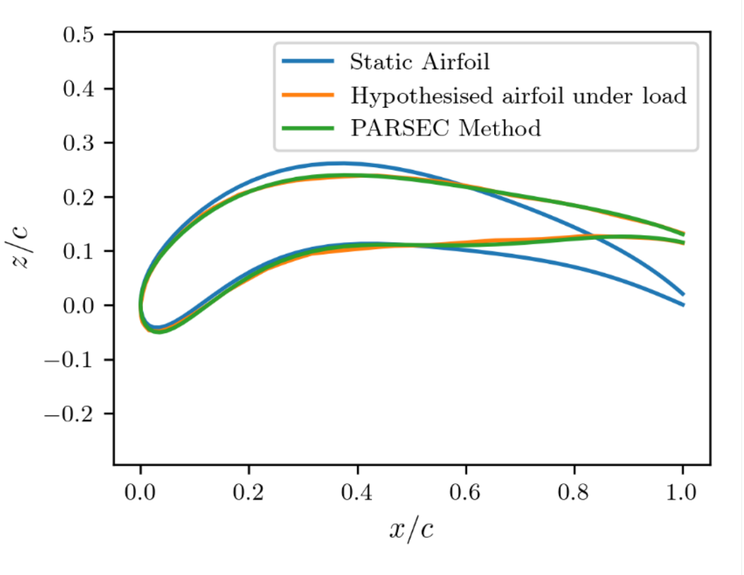

Figure 43: Hypothesised GHA arm section wing under aerodynamic load and the airfoil produced by the PARSEC method using the bounds developed.

5.3. Optimized geometry of a Grey-headed Albatross airfoil

The optimization of the parameterized GHA arm airfoil was completed using Siemens STAR-CCM+ in Design Manager as described in sub-section 5.1. In addition to the 12 PARSEC parameters, the angle of attack was also set to be a parameter which could be changed. The parameters can be changed subject to the design space calculated earlier. The starting design is the static GHA arm airfoil. The optimization aimed to maximize the C_L/C_D. Each design was terminated at either 1000 iterations, or earlier, if it was found that both the C_L and C_D values differ less than 1% for the previous 50 iterations. 800 designs were completed using the SHERPA algorithm, resulting in a total simulation time of 28.5 days including the meshing and initialization time of 10 hours. The optimization was performed on 5 CPU cores (Intel Core i7-3930K).

In Figure 44, the evolution of the aerodynamic coefficients of interest is shown for all the designs with a plateau reached after, approximately 600 designs. The C_L and C_D scatter plots indicate that the optimization aimed to reduce the C_D to increase the C_L/C_D and not to increase the C_L to achieve the same goal. The C_L increased by a factor of 2, whilst the C_D was decreased by a factor of 9.1.

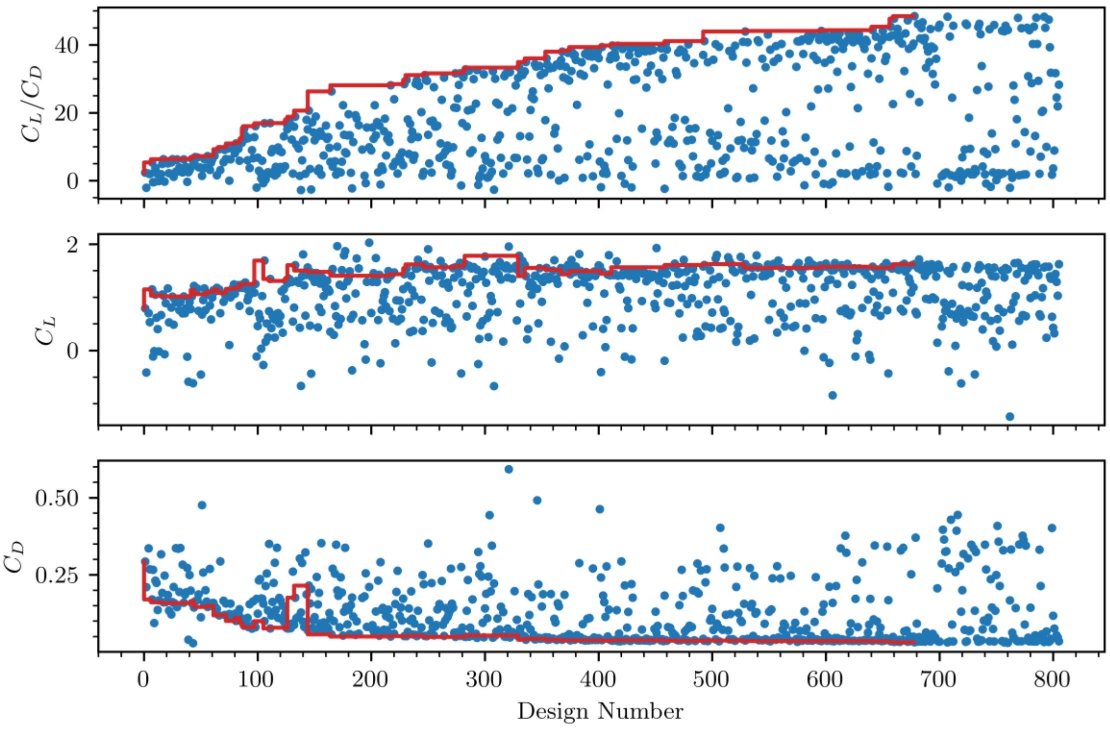

f

Figure 44: Aerodynamic quantities changing and improving as the number of designs tested increase. The red line shows the evolution of the best design.

The optimization strategy mentioned previously can be visualized in Figure 45. In this scatter plot, each design’s C_L and C_D is indicated together with the aerodynamic efficiency represented by the colour.

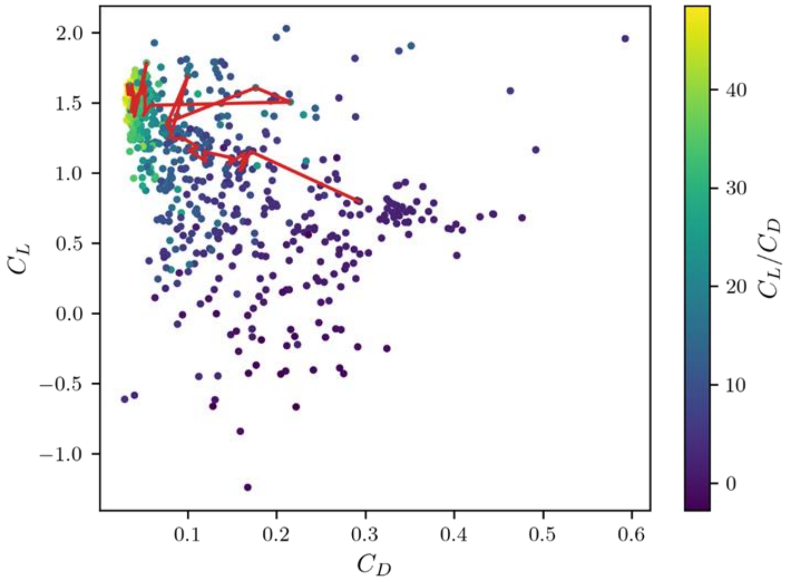

Figure 45: Scatter plot showing each design's C_D and C_L. The aerodynamic efficiency is also indicated. The red line shows the evolution of the best design.

The change in each PARSEC parameter as well as the angle of attack for each design iteration is shown in Figure 46 which indicates the search trends for each parameter followed towards obtaining an optimum. Starting from X_{lo}, shown at the top of Figure 46, this value was decreased to almost as low as possible within the bounds. It was expected that the camber would decrease, shifting the X_{lo} value toward the middle of the airfoil, but upon further inspection, this value was responsible for the concave indentation formed on the lower side of the airfoil.

The other parameter to be mentioned with X_{lo}, is Z_{lo}. This value was not changed drastically, but the effect of this value was exaggerated in conjunction with the low X_{lo} value. The upper crest location, $(X_{\mathrm{up}}, Z_{\mathrm{up}})$ was shifted much further to the right with the z coordinate almost staying the same. The upper and lower curvatures, $Z_{\mathrm{xx,\,up}}$ and $Z_{\mathrm{xx,\,lo}}$, were increased (i.e., more positive). This enabled the smooth surface between the upper crest location and the trailing edge, dictated by the value Z_{te}, which is seen to increase drastically. The lower surface curvature was also responsible for the concave indentation near the leading edge.

The only two other PARSEC parameters which had a direct geometrical influence on the airfoil was the upper and lower leading-edge radii, $r_{\mathrm{le,\,up}}$ and $r_{\mathrm{le,\,up}}$. These two values decreased from the original airfoil. The $r_{\mathrm{le,\,up}}$ value was responsible for the slight concave indentation on the upper surface near the leading edge. The small $r_{\mathrm{le,\,lo}}$ value mimicked the sharp leading edge encountered on the GHA airfoil shown in Figure 45, but it could not recreate the sharp feature which looks like it should almost be discontinuous. This sharp discontinuous edge was not possible using the PARSEC method, but the extremely low $r_{\mathrm{le,\,lo}}$ value showed that it tended to a sharp leading edge. The remaining quantities (α_{te}, β_{te}, and ΔZ_{te}) allowed streamlining of the trailing edge of the airfoil. They also allowed a thin trailing edge region to be generated mimicking few feathers at the trailing edge.

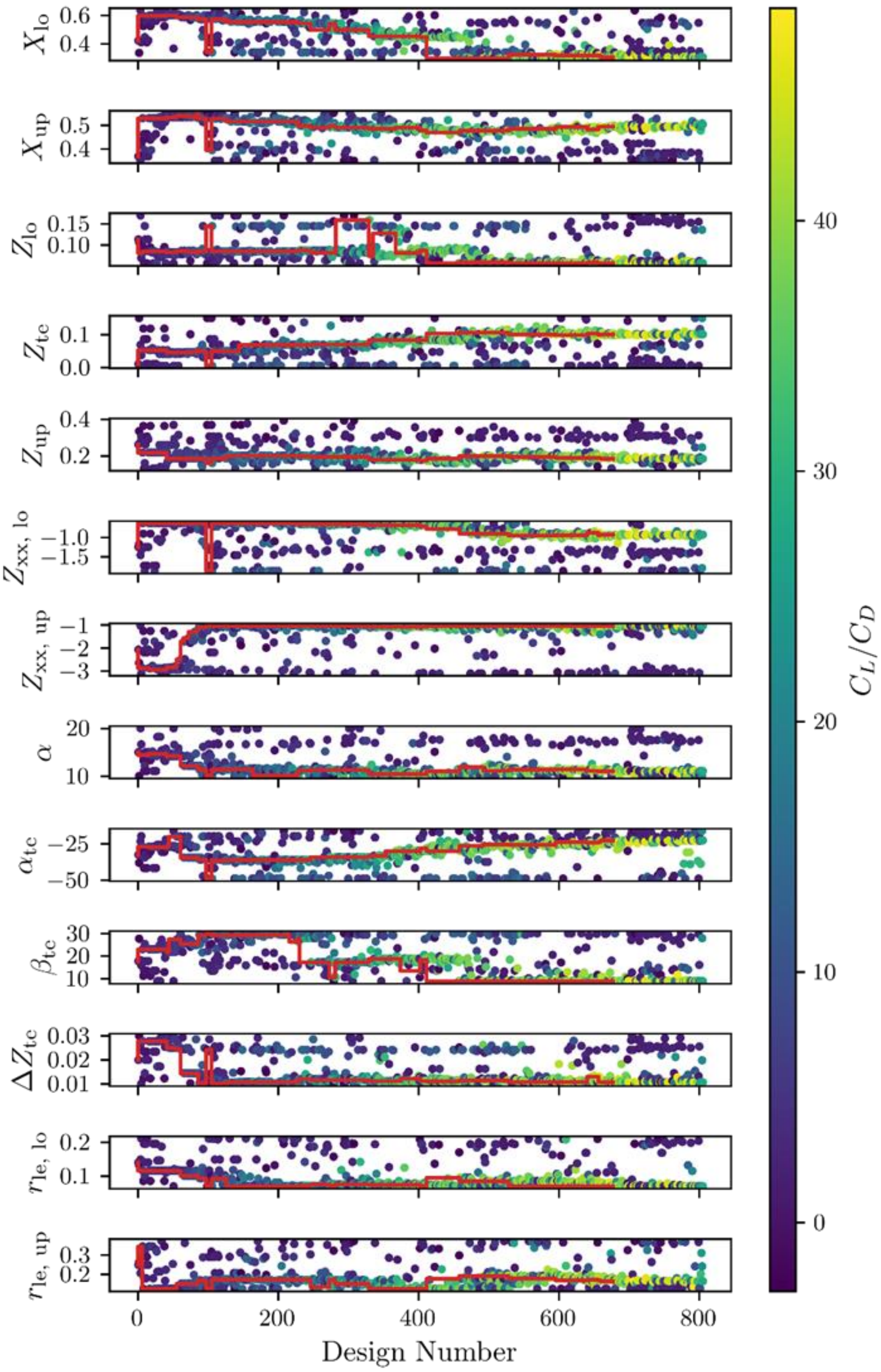

Figure 46: Scatter plot showing each PARSEC parameters changing for different designs. The aerodynamic efficiency is indicated with the colour of each design to give an indication on how it increases as the number of designs increase.

Figure 47 and Figure 48 show the evolution of the PARSEC parameters and the angle of attack. These figures give the PARSEC parameters and angle of attack of 6 different designs, each increasing in aerodynamic efficiency roughly by a count of 10 to show how the geometry is transformed from the baseline to the optimized airfoil. In Figure 47, each PARSEC parameter as well as the angle of attack was scaled between the lower and upper bounds given in Table 9b (Appendix F) to produce scaled values between 0 and 1. The following equation was used:

$$p^* = \frac{p - p_l}{p_u - p_l} \tag{27}$$

where p^* represents the scaled PARSEC parameter (or angle of attack in this case), p represents an arbitrary PARSEC parameter (or angle of attack), and p_l and p_u represent the lower and upper bounds of the parameters. The primary focus of Figure 47, is the paths followed for designs with increasing aerodynamic efficiency as well as the trend within the design space. There are many different airfoils which have the same aerodynamic efficiency and the results given in Figure 47 and Figure 48 are merely showing the types of airfoils created during the optimization together with their PARSEC parameters and angles of attack.

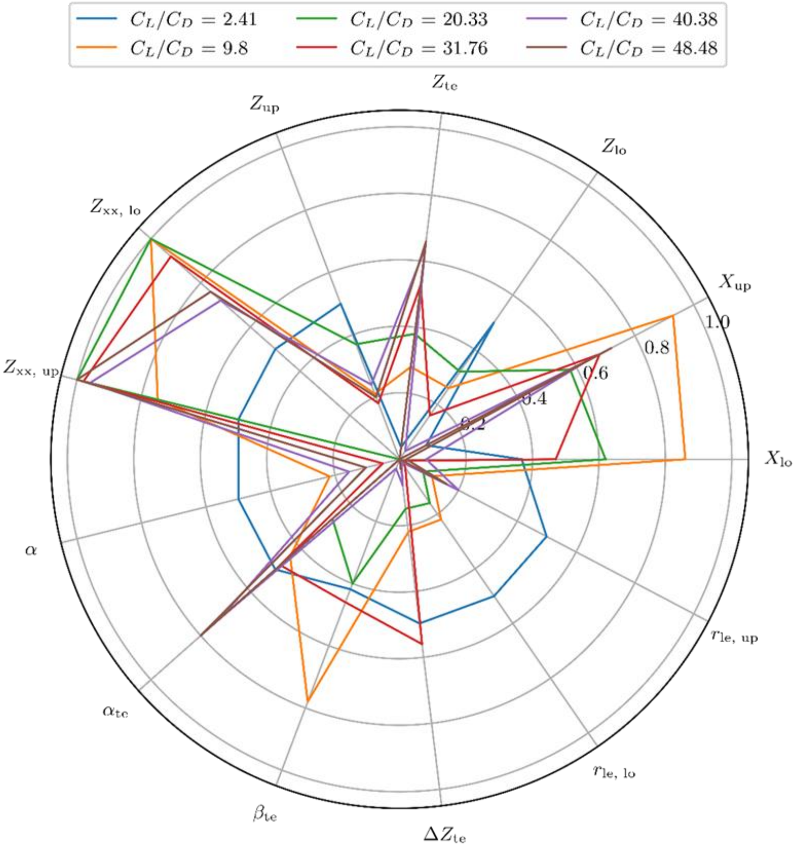

Figure 47: Spider plot showing the PARSEC parameters and angle of attack of 6 different designs, each increasing by roughly a count of 10 from the baseline design, shown in blue.

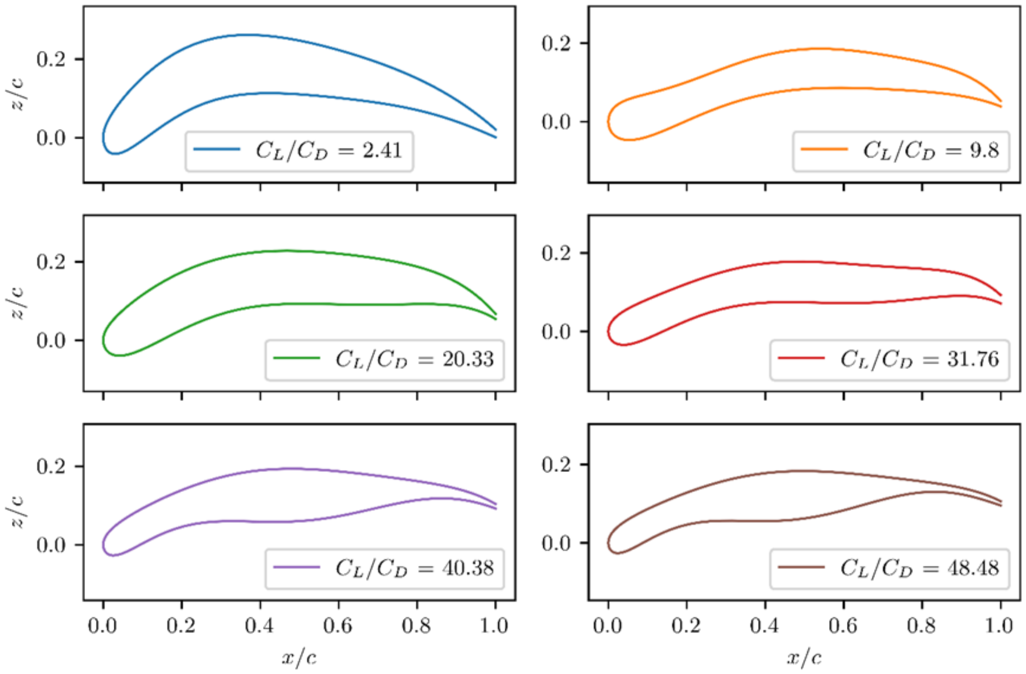

Figure 48: Airfoils created using the PARSEC parameters shown in Figure 47, each increasing in aerodynamic efficiency by roughly a count of 10.

The optimized airfoil is given in Figure 49 and the PARSEC parameters are given in Table 6. The aerodynamic efficiency is $C_L/C_D = 48.5$. As hypothesised, the camber decreased dramatically, similar to the work of Nachtigall and Wieser (1966) and Cheney et al. (2021). The other notable change in the airfoil was the "bump" on the pressure side of the airfoil. When inspecting an airfoil obtained from laser scan done in the presence of airflow at $V = 15\text{ms}^{-1}$, shown in Figure 50, it was observed that separating feathers resulted in a similar "bump" on the pressure side.

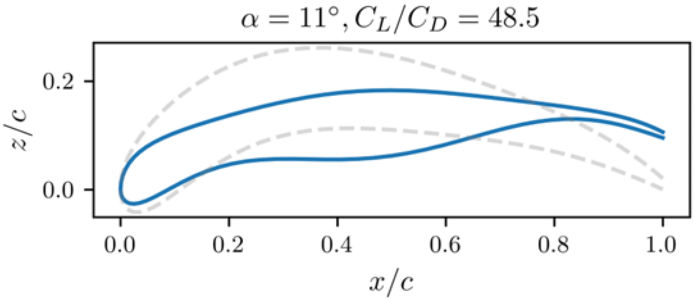

Figure 49: The optimized airfoil of the GHA arm wing showing the aerodynamic efficiency and the angle of attack at the maximum efficiency. The dashed grey line indicates the baseline airfoil. The geometric angle of attack of the aerofoil is −11.52° due to the TE deflection and the flow angle is 11°. The net angle of attack (chord relative to airflow) is therefore −0.52°.

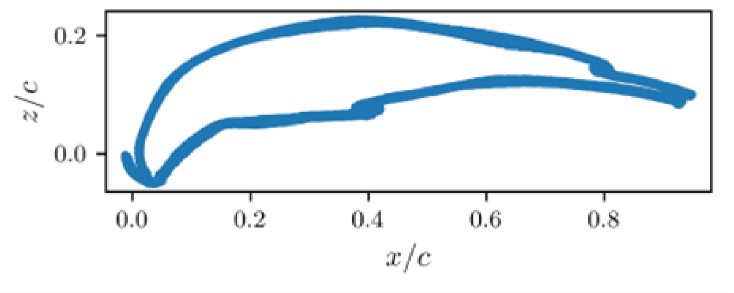

Figure 50: Airfoil of the GHA in the presence of airflow at $V = 15\text{ms}^{-1}$ showing similar geometrical features when compared to the optimized airfoil.

Table 6: PARSEC parameters of the optimized GHA arm airfoil compared to the baseline values indicating the change in each parameter.

Parameter	Optimized	Baseline	Change
$r_{\text{le, lo}}$	0.0702	0.1405	-50%
$r_{\text{le, up}}$	0.16406	0.2485	-34%
X_{lo}	0.3067	0.4230	-27.5%
X_{up}	0.4957	0.3683	+34.6%
Z_{lo}	0.0566	0.1131	+49.9%
Z_{up}	0.1831	0.2616	+29.6%
$Z_{\text{xx, up}}$	-1.0361	-2.0722	+50%
$Z_{\text{xx, lo}}$	-0.9249	-1.2498	+26%
α_{te}	-22.8148	-32.593	+42.1%
β_{te}	8.8457	17.691	-50%
Z_{te}	0.1008	0.0106	+850%
ΔZ_{te}	0.0106	0.0200	-47%

5.4. Aerodynamic findings of the optimized GHA airfoil

5.4.1. Steady and unsteady state validation study

Although Section 4 indicated that an unsteady solver would more realistically capture the flow variables for certain geometries and high angles of attack, the computational cost was exorbitant. Therefore, the optimization was done using the steady solver following the findings of Pauley et al. (1990) who showed time averaged results from the steady solver correlate within reason to unsteady solver results.

However, to provide a comprehensive overview of the optimized GHA airfoil that was developed from the steady solution, further investigations were all completed using the unsteady solver. Time sensitive quantities such as lift and drag coefficients and separation locations would also not require time averaging. The difference between the steady solver (which was used for the optimization) and an unsteady solver were investigated and compared to ensure that the objective function on which the optimization was based was reasonable. Figure 51 shows the C_L, C_D and C_L/C_D polars using both the steady and unsteady solver for the optimized GHA airfoil at a variety of angles of attack.

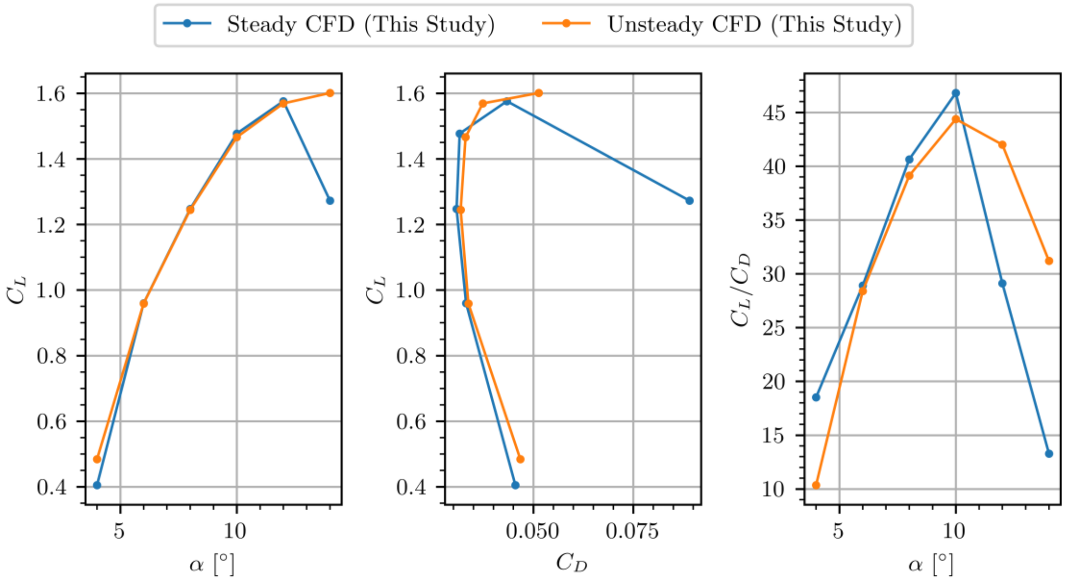

Figure 51: The polars computed for the optimized GHA arm airfoil at Re = 2×10^5 used to compare the two different solvers.

The steady and unsteady results for angles of attack before stall showed an average difference of 5% and 3% with regards to the C_L and C_D respectively For the sake of accuracy, the results presented in the remainder of this section was computed using the unsteady solver since it was seen to be more stable at higher angles of attack when considering Figure 51.

5.4.2. Unsteady results of aerodynamic analyses on optimized GHA airfoil

Figure 52 shows the C_L vs α polars for the optimized airfoil and the baseline arm airfoil at Re = 2×10^5. The optimized airfoil and the baseline airfoil exhibit very similar polars, and the only difference is that the angle of attack is shifted by 6° between the two. This value is consistent with the angle of the optimized airfoil's geometric chord, which is approximately $-6°$ relative to a horizontal flow vector.

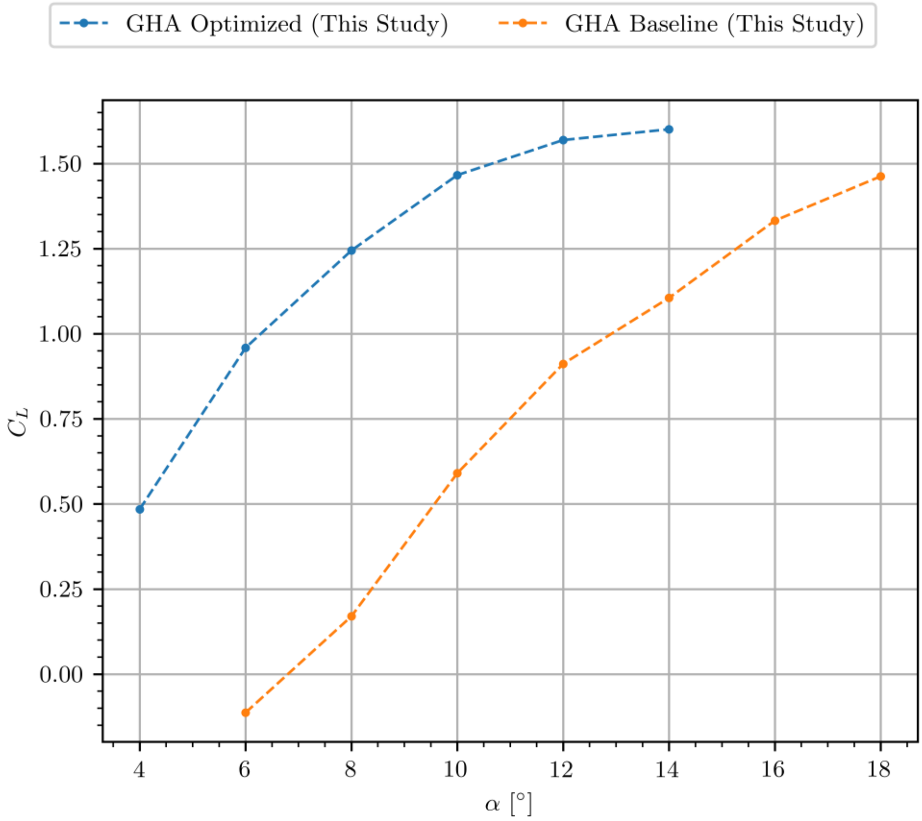

Figure 52: C_L vs α polar comparison for the optimized airfoil and the baseline airfoil at $\mathrm{Re} = 2 \times 10^5$.

Figure 53 shows the C_D vs α polars for the optimized and baseline airfoils. The $(C_D)_{\min}$ value of the baseline airfoil is 437% higher than the optimized airfoil. The drastic difference between the $(C_D)_{\min}$ values between the optimized GHA and the baseline GHA show one of the strategies used by the optimization to increase the aerodynamic efficiency. The shape of the optimized airfoil's C_D vs α curve is like that found on other airfoils. The baseline case however shows a linear dependency on the angle of attack, mimicking that of a bluff body.

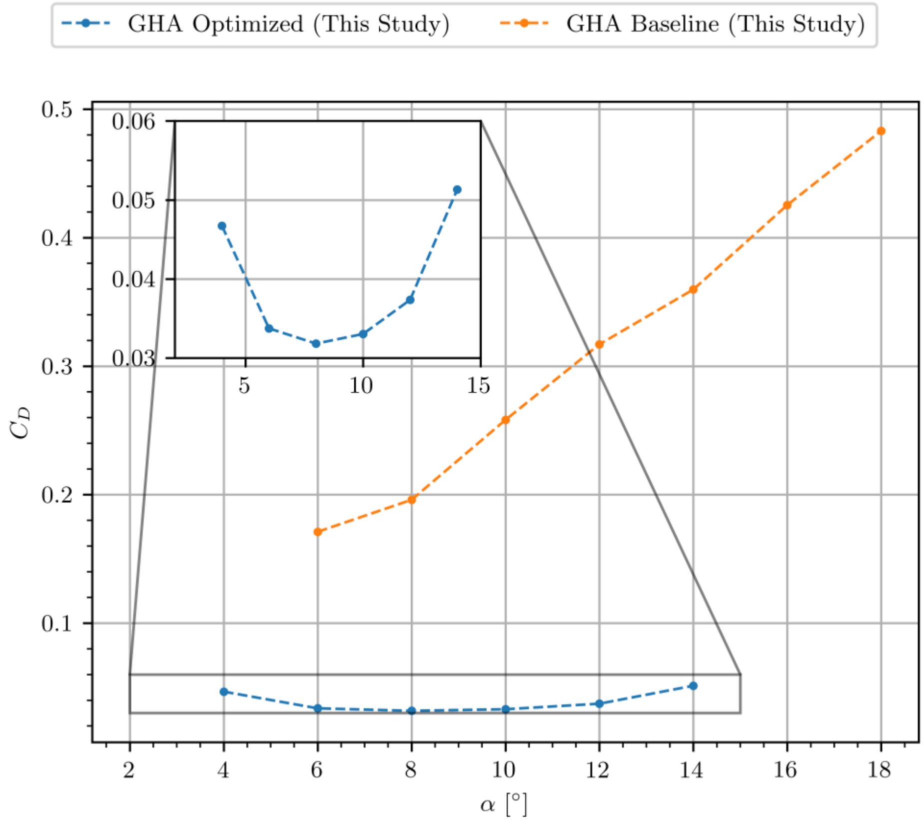

Figure 53: C_D vs α polar comparison for the optimized airfoil and the baseline airfoil at Re = 2×10^5.

The drag can be split into the friction ($C_{D,f}$) and pressure ($C_{D,P}$) drag components to describe the difference in the total drag values between the optimized and baseline GHA airfoils. The C_F vs x/c plots and velocity scalar fields are presented in Figure 54 and Figure 55. Figure 54a shows the separation and reattachment locations on the baseline airfoil at the angle of attack at which the maximum efficiency is encountered. Flow separation occurred at $x/c = 0.2$ and $x/c = 0.03$ on the top and bottom surfaces, respectively. The flow on the top surface did not reattach, but the flow on the bottom surface reattached at $x/c = 0.7$.

The size of the wake was visually larger and representative of a bluff body rather than a streamlined aerodynamic body. The optimized airfoil had multiple short separation and reattachment regions shown in Figure 54b. On the optimized airfoil, flow separation occurred at $x/c = 0.05$ and reattached at $x/c = 0.23$ on the bottom surface. The flow was attached on the bottom surface until the trailing edge. The flow on the top surface separated $x/c = 0.46$ and reattached at $x/c = 0.7$. This caused a separation bubble with a length of $0.24c$. A final separation occurred at $x/c = 0.95$.

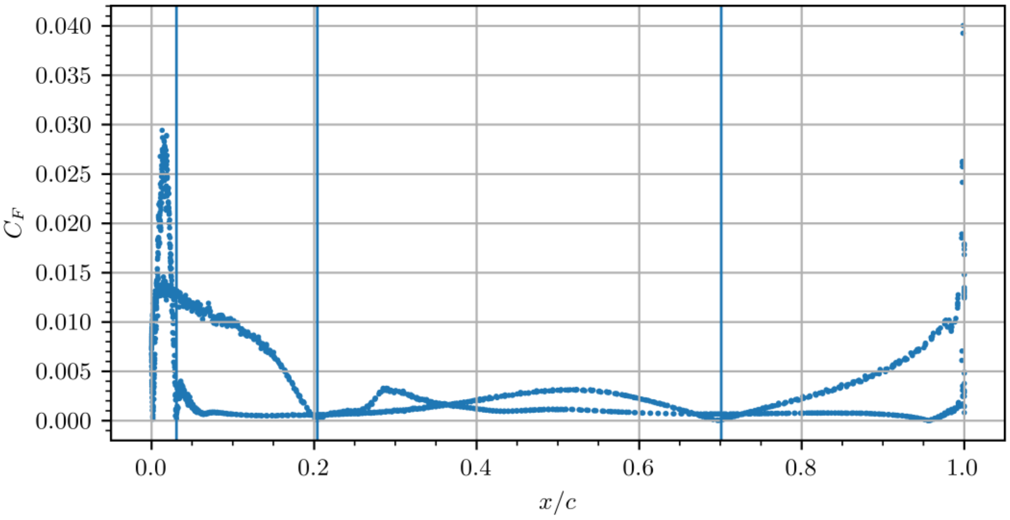

(a)

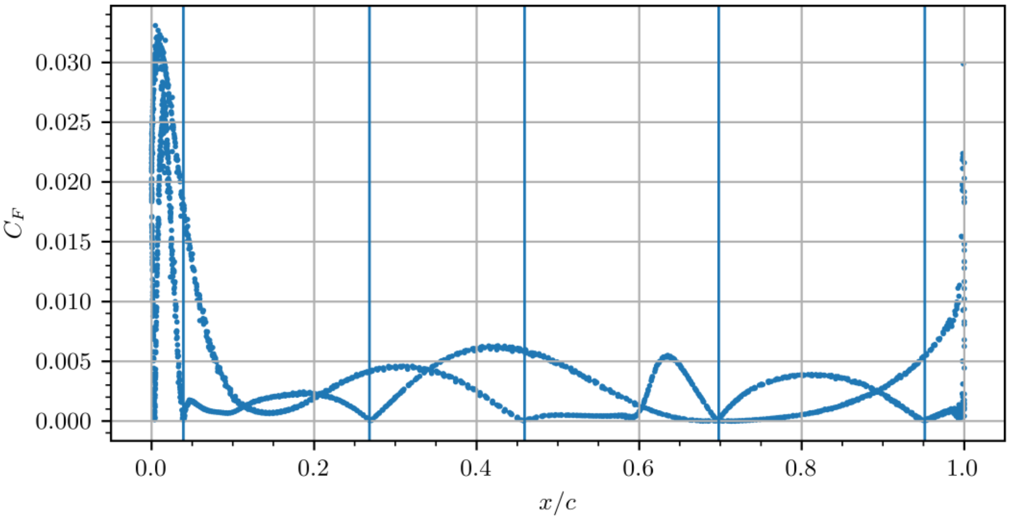

(b)

Figure 54: C_F vs x/c at Re $= 2 \times 10^5$ for the (a) baseline GHA airfoil at $\alpha = 15°$ and the (b) optimized GHA airfoil at 10° showing the separation and reattachment locations as vertical lines.

The separation and reattachment locations are shown as vertical red lines on the normalized velocity contour plots shown in Figure 55. Figure 55a shows the natural separation at $x/c = 0.2$ on the top surface of the baseline GHA airfoil as well as the separation and reattachment on the bottom surface. The separation and reattachment on the bottom surface was not a separation bubble but merely a separation at the leading edge followed by flow which reencountered the bottom surface of the airfoil again at $x/c = 0.7$. Figure 55b shows the separation bubbles at $x/c = 0.05$ on the bottom surface and $x/c = 0.46$ on the top surface of the optimized airfoil. The $C_{D,f}$ values of the baseline and optimized airfoils were 0.002 (0.6% of total drag) and 0.005 (15% of total drag) respectively. Since a larger section of the flow remained attached to the surface of the optimized airfoil there was an increase in the friction drag component. The percentage of attached flow was 26.5% ($x/2c = 0.53$) and 76.5% ($x/2c = 1.53$) on the baseline and optimized airfoils respectively (adding the top and bottom surfaces, hence using $2c$).

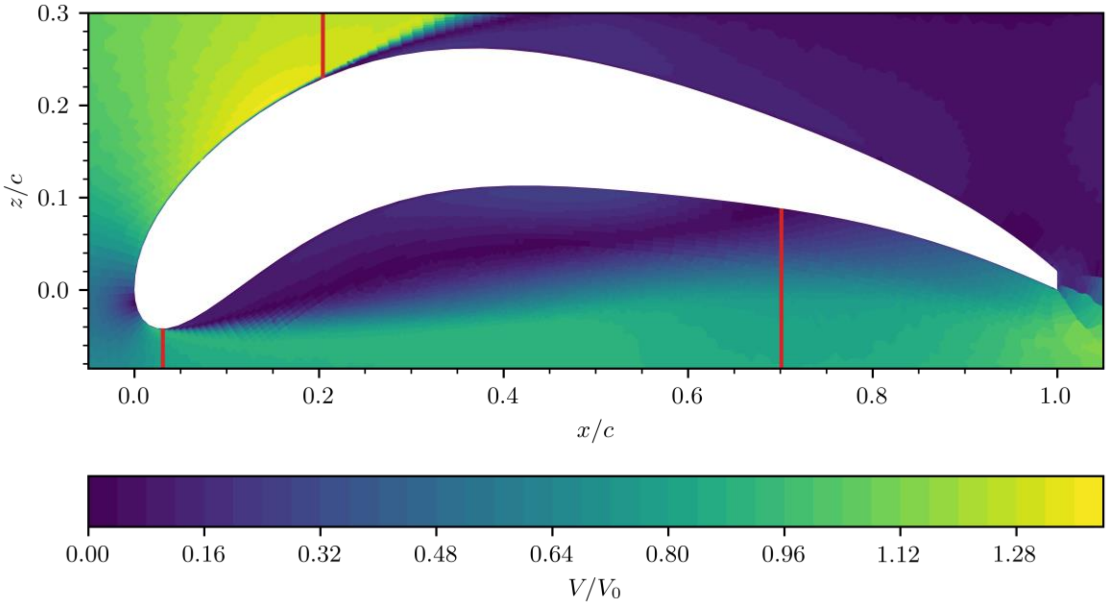

(a)

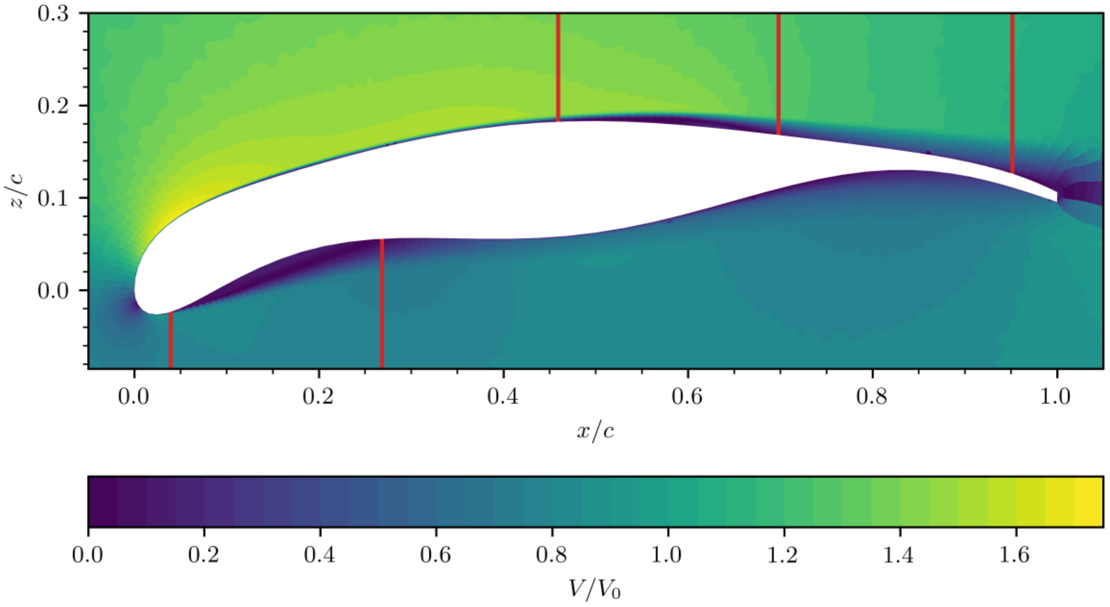

(b)

Figure 55: Normalized velocity magnitude contour plot for the (a) baseline GHA airfoil and the (b) optimized GHA airfoil.

The $C_{D,P}$ for the baseline and optimized airfoils were 0.395 and 0.029 respectively. The pressure drag for the baseline case was therefore a factor of 13.6 times more than the optimized case. Figure 56 shows the normalized x velocity profiles for different streamwise stations comparing the wake sizes between the baseline and optimized airfoils. At all the streamwise stations, the minimum velocity of the baseline case was much lower (and at $x/c = 1$ and $x/c = 2$ it is negative), which indicates that the wake of the baseline airfoil would take much longer to dissipate when compared to the optimized airfoil.

The momentum deficit observed at the different streamwise locations for the two airfoils show a clear reduction in the energy loss. The baseline airfoil had a larger bluffness as experienced from the flow leading to a thicker wake profile, compared to the optimized airfoil that has significantly reduced the wake thickness. This increase in bluffness is supported by the findings of Nachtigall and Wieser (1966) and Cheney et al. (2021) which shows the decrease of camber of avian airfoils when in flight (also see Figure 42). This can be interpreted as decreasing the bluffness of the airfoil i.e., turning it from a bluff body shape to a streamlined shape.

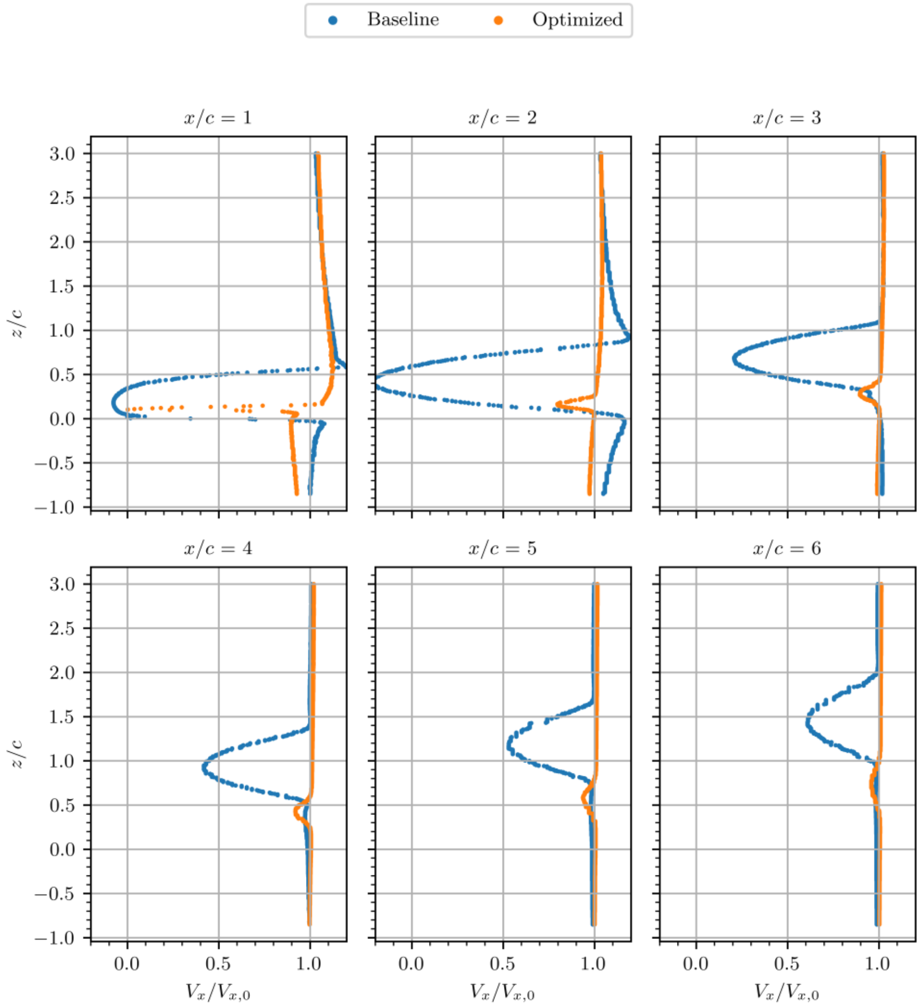

Figure 56: Normalized velocity profiles in the x direction as a function of the vertical height for different streamwise stations.

Figure 57 shows the C_L/C_D vs α polars for the baseline and optimized airfoils. The optimized airfoil and the baseline airfoil have $(C_L/C_D)_{\max}$ values of 44.5 and 3.1, respectively. The efficiency increased 1335% from the baseline to the optimized case. The improvement in efficiency was partly due to the decrease in pressure drag.

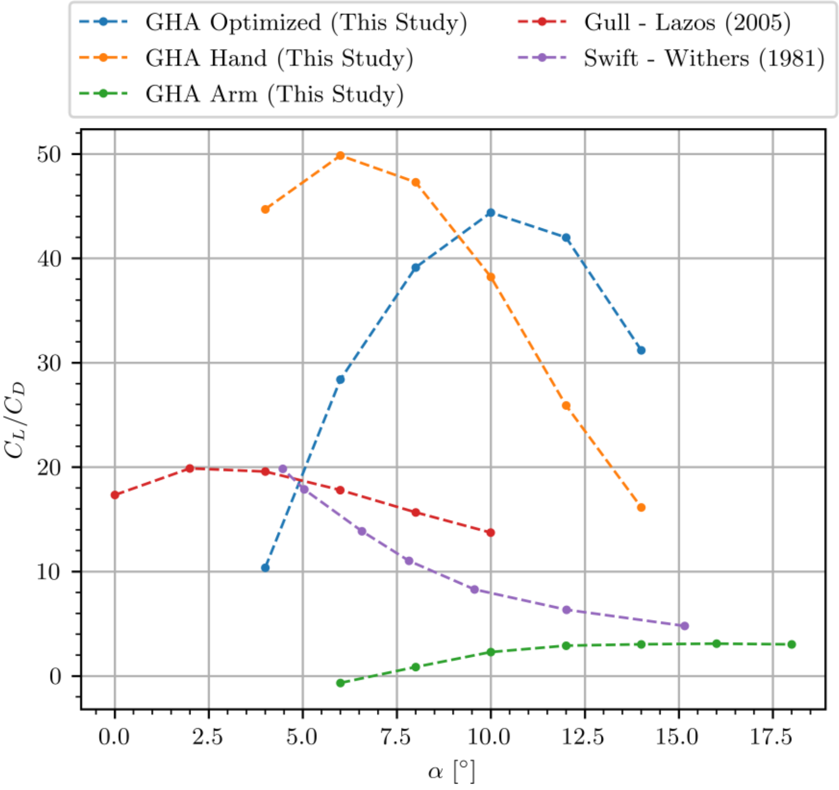

Figure 57: C_L/C_D vs α polar comparison for the optimized GHA airfoil and the GHA arm airfoil.

.

6. Conclusions and Recommendations

6.1. Reconstructing the GHA wing

The Grey-headed Albatross (GHA) is a highly efficient sea bird (Pennycuick and Lighthill, 1982) and it is known that birds morph their wings to generate the highest aerodynamic efficiency (Norberg, 1990, 2006). A reliable geometrical model needs to be created, to investigate the aerodynamic performance of the GHA wing. The point cloud data of a GHA wing was obtained using a 3D laser scanner. Thirty airfoils along the span of the wing were extracted and used to determine the geometrical characteristics of a GHA wing in the absence of airflow (static). The static undeformed geometry of the GHA wing was extracted and compared to methods used previously. The methods used are novel to the field of avian airfoils.

The new methodology used the PARSEC parameterization method, and it was found that it consistently recreated airfoils of different geometries. The same set of mathematical rules and equations were used for any given airfoil and as few as 12 geometrical parameters were required to recreate a given airfoil, even if the airfoil contains sporadic outliers. The PARSEC parameters were calculated from 2D airfoil data from the scanned wing using a differential evolution optimization algorithm aiming to minimize the mean squared error between the actual airfoil and the airfoil created using the PARSEC method. This was done for each of the 30 airfoils extracted on the GHA wing in the spanwise direction.

The traditionally used Birnbaum-Glauert method (Liu *et al.*, 2006; Klän *et al.*, 2009). as well as the PARSEC method was used to generate two sets of separate airfoil data for the entire wing (30 airfoils per wing). The two sets of data could then be used to compare the two methods to the actual scanned wing geometry. Each set consisted of a thickness distribution and a camber distribution. It was found that both methods could recreate the camber distribution of the wing within a reasonable error without any obvious geometrical deviations. The thickness distribution comparisons however indicated that the PARSEC method was more capable of recreating the actual scanned geometry with average deviations of $0.002c$ when compared to the actual scanned geometry. The Birnbaum-Glauert method had larger average deviations from the actual geometry of $0.0057c$, proving the need for a new method to mathematically quantify the geometry of avian wings.

The macro geometrical parameters of sweep, camber, twist and chord length, of the GHA wing was determined and used in conjunction with averaged airfoils of the arm and hand section to create a 3D model of the GHA wing. The static undeformed geometry of the GHA wing was modelled using the PARSEC parameterization method and compared to methods used previously.

6.2. Modelling the aerodynamics of the GHA wing

The second part of the work aimed to determine the 'in-flight" geometry of the arm section airfoil of the GHA wing. The method to determine the morphed geometry is a new approach to the field of avian wings. An aerodynamic optimization study was done using CFD (Siemens STAR-CCM+ and Design Manager) utilising the SHERPA optimization algorithm.

The CFD approach was validated using the E387 airfoil which has well documented results using wind tunnel experiments and CFD. A highly automated meshing approach to flows around low Reynolds number airfoils was developed, and it was found that this meshing strategy enabled the use of the same numerical "template" which was essentially the same domain, boundary conditions, solver etc., but the computational grid changes automatically for whichever geometry was used. The average C_L and C_D error was 4% and 7.6%, and 0.2% and 16% for the E387 and S1223, respectively.

The design space had to be determined, to perform an optimization study. A novel investigation into the bounds used for an optimization on a PARSEC airfoil was done. Using statistical methods, the largest design space was developed whist ensuring that the airfoils created by the PARSEC method did not have "failing" geometries more than 20% of the time. The anatomical and skeletal features of the wing was also accounted for to ensure that geometries could originate from the baseline (static) geometry.

The evolution of the PARSEC parameters during the optimization shows similar results compared to Nachtigall and Wieser (1966), and Cheney et al. (2021) where the peak camber of the airfoil decreases. The other result, consistent with Nachtigall and Wieser (1966) was that the trailing edge of the airfoil moved vertically up in order to create a more streamlined airfoil. The aerodynamic coefficients of lift and drag were compared between the optimized and baseline case.

Further investigations were conducted using the unsteady solver, to provide a more comprehensive overview of the optimized GHA airfoil developed from the steady solution, The results for angles of attack before stall indicated an average difference of 5% and 3%

for the lift and drag coefficients, respectively, between the steady and unsteady solutions. Therefore, the optimized airfoil was simulated using an unsteady solver before evaluating the results.

The optimized airfoil and the baseline airfoil have nearly identical lift polars, with the only discernible difference being a shift in angle of attack by to 6°. The baseline airfoil experiences an 8.6% higher maximum C_L than the optimized airfoil. Total drag is decomposed into friction and pressure components to explore the differences. Comparing the friction drag, it was noted that the $C_{D,f}$ values of the baseline and optimized airfoils are 0.002 (0.6% of total drag) and 0.005 (15% of total drag) respectively. The baseline airfoil therefore had less friction drag and could not be the cause of the high drag associated with it. It is important to note that the static arm section baseline airfoil likely represents the worst-case scenario with regards to aerodynamic efficiency. Sections of the wing toward the tip would likely achieve higher efficiencies, contributing to the overall performance.

The $C_{D,P}$ for the baseline and optimized airfoils are 0.395 (99.4% of total drag) and 0.029 (85% of total drag) respectively. The pressure drag for the baseline case is therefore a factor of 13.6 times more than the optimized case. This was also further supported by investigating the momentum deficit at different streamwise locations. This revealed a marked decrease in energy loss for the optimized airfoil. The baseline airfoil exhibited a larger bluffness, resulting in a thicker wake profile, while the optimized airfoil showed a significantly more streamlined profile, leading to a reduction in wake thickness. Typical drag values reported are 0.03 for a swift at $(C_L/C_D)_{\max} = 17$ (Withers, 1981), 0.025 for a gull at $(C_L/C_D)_{\max} = 19.88$, and roughly 0.045 for a GHA using $(C_L/C_D)_{\max} = 22$ and $C_L = 1.00$ (Pennycuick and Lighthill, 1982). The calculated $C_D = 0.029$ at $(C_L/C_D)_{\max} = 44$ is consistent with the drag values mentioned previously.

6.3. Recommendations for Future Work

The aerodynamics of low Reynolds number flyers is an exciting prospect and being able model these to a reasonable degree can allow key insights into the future of the development of similar low Reynolds number aircraft.

Further work on the GHA airfoil should include the following recommendations:

- The number of PARSEC variables can be increased. The bump on the bottom side of the airfoil is likely to be caused by a mathematical shortcoming of using the

PARSEC method as it is implemented in the study, shown in Figure 58. The fourth equation of the linear algebra problem posed in equations (9) and (10) controls the first derivative of the upper and lower surfaces. At X_{lo} and X_{up}, the gradient for the upper and lower crests are controlled. The value to which it is equated normally is zero, which forces a local minimum or maximum at the respective location (either $[X_{\mathrm{lo}}, Z_{\mathrm{lo}}]$ or $[X_{\mathrm{up}}, Z_{\mathrm{up}}]$). If the trailing edge is anticipated to be positioned at a moderately high Z_{te} value, it is crucial for the upper and lower crest gradient values to be non-zero (the dashed lines connecting the upper and lower crests to the trailing edge have a non-zero gradient). This non-zero value will facilitate a gradient, enabling a seamless transition between the crest location and the trailing edge. The standard value of 0 could be the cause for the bump on the underside of the airfoil. A new pair of PARSEC parameters could therefore be required in future applications. This new value can be introduced as $Z_{\mathrm{x,\,lo}}$ and $Z_{\mathrm{x,\,up}}$ (read as the first derivative of Z in x) and would be called the lower and upper crest gradients respectively. This would increase the number of PARSEC parameters to 14.

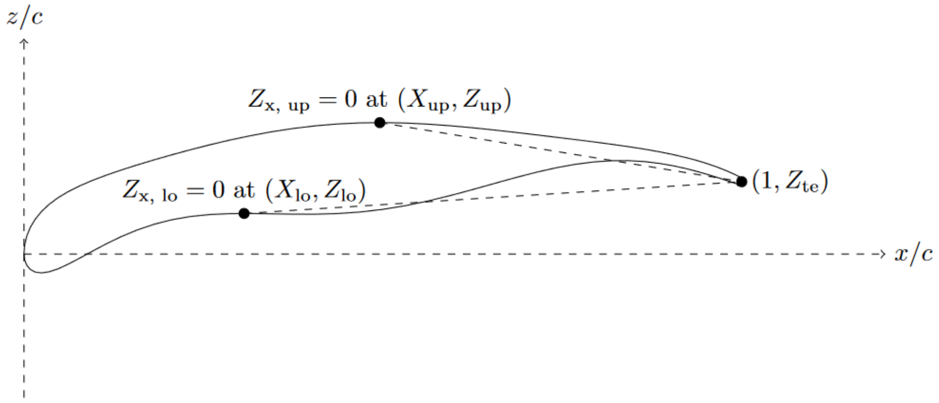

Figure 58: Optimized airfoil of the GHA showing the upper and lower crest locations which are required to have gradient of zero.

- Extend the scope of work to a three-dimensional CFD analysis of the wing to gain an understanding of the possible spanwise flows present.

This research offers a first step to understand the aerodynamic and geometric morphing properties and characteristics of the GHA and concrete conclusions are not able to be made when only considering a 2D case as done in this research

Bibliography

Akram, M.T. and Kim, M.-H. (2021) 'Aerodynamic Shape Optimization of NREL S809 Airfoil for Wind Turbine Blades Using Reynolds-Averaged Navier Stokes Model—Part II', *Applied Sciences*, 11(5), p. 2211. Available at: https://doi.org/10.3390/app11052211.

Alerstam, T., Gudmundsson, G.A. and Larsson, B. (1993) 'Flight tracks and speeds of Antarctic and Atlantic seabirds: radar and optical measurements', *Philosophical Transactions of the Royal Society of London. Series B: Biological Sciences*, 340(1291), pp. 55–67. Available at: https://doi.org/10.1098/rstb.1993.0048.

Althaus, D. and Wortmann, F.X. (1981) *Stuttgarter Profilkatalog*. Stuttgart: Universität Stuttgart.

Ananda, G.K. and Selig, M.S. (2018) 'Design of Bird-Like Airfoils', in *2018 AIAA Aerospace Sciences Meeting*. Reston, Virginia: American Institute of Aeronautics and Astronautics. Available at: https://doi.org/10.2514/6.2018-0310.

Anderson John D. Jr. (John David), 1937- (2012) *Introduction to flight*. 7th ed. New York: McGraw Hill (Anderson series). Available at: http://catdir.loc.gov/catdir/enhancements/fy1107/2010048329-d.html.

Arias-Montano, A., Coello Coello, C.A. and Mezura-Montes, E. (2012) 'Multi-objective airfoil shape optimization using a multiple-surrogate approach', in *2012 IEEE Congress on Evolutionary Computation*. IEEE, pp. 1–8. Available at: https://doi.org/10.1109/CEC.2012.6256491.

ASME (2008) 'Procedure for Estimation and Reporting of Uncertainty Due to Discretization in CFD Applications', *Journal of Fluids Engineering*, 130(7), p. 078001. Available at: https://doi.org/10.1115/1.2960953.

Babajee, J. and Arts, T. (2013) 'Investigation of the laminar separation-induced transition on two low-pressure turbine rotor blades', *International Journal of Engineering Systems Modelling and Simulation*, 5(1/2/3), p. 99. Available at: https://doi.org/10.1504/IJESMS.2013.052377.

Batill, S. and Mueller, T. (1980) 'Experimental studies of the laminar separation bubble on a two-dimensional airfoil at low Reynolds numbers', in *13th Fluid and PlasmaDynamics Conference*. Reston, Virigina: American Institute of Aeronautics and Astronautics. Available at: https://doi.org/10.2514/6.1980-1440.

Baudinette, R. V. and Schmidt-Nielsen, K. (1974) 'Energy cost of gliding flight in herring gulls', *Nature*, 248(5443), pp. 83–84. Available at: https://doi.org/10.1038/248083b0.

Beneke, A. (2018) *The Simultaneous Optimization of the Nose and Tail Geometry of a High-Speed Train for Drag and Crosswind Stability*. University of Pretoria.

Boughou, S. *et al.* (2022) 'Low Reynolds Number effect on CFD prediction of Bio Inspired Aerodynamics', in *AIAA SCITECH 2022 Forum*. Reston, Virginia: American Institute of Aeronautics and Astronautics. Available at: https://doi.org/10.2514/6.2022-1965.

Brooke, M. (2004) *Albatrosses and Petrels across the World (Bird Families of the World)*. Oxford University Press.

Carreño Ruiz, M. and D'Ambrosio, D. (2022) 'Validation of the $$\gamma \text{-Re }_{\theta }$$ Transition Model for Airfoils Operating in the Very Low Reynolds Number Regime', *Flow, Turbulence and Combustion*, 109(2), pp. 279–308. Available at: https://doi.org/10.1007/s10494-022-00331-z.

Carruthers, A.C. *et al.* (2010) 'Aerodynamics of aerofoil sections measured on a free-flying bird', *Proceedings of the Institution of Mechanical Engineers, Part G: Journal of Aerospace Engineering*, 224(8), pp. 855–864. Available at: https://doi.org/10.1243/09544100JAERO737.

Catry, P., Phillips, R.A. and Croxall, J.P. (2004) 'Sustained Fast Travel by a Gray-Headed Albatross (Thalassarche Chrysostoma) Riding an Antarctic Storm', *The Auk*, 121(4), pp. 1208–1213. Available at: https://doi.org/10.1093/auk/121.4.1208.

Cauchy, A. (1847) 'Methode generale pour la resolution des systemes d'equations simultanees', *C.R. Acad. Sci. Paris*, 25, pp. 536–538. Available at: https://cir.nii.ac.jp/crid/1573387450834953216.

Chen, L. *et al.* (2020) 'Aerodynamic performance and transition prediction of low-speed fixed-wing unmanned aerial vehicles in full configuration based on improved $\gamma - \text{Re}$ model', *Aerospace Science and Technology*, 107, p. 106281. Available at: https://doi.org/10.1016/j.ast.2020.106281.

Cheney, J.A. *et al.* (2021) 'Raptor wing morphing with flight speed', *Journal of The Royal Society Interface*, 18(180), p. 20210349. Available at: https://doi.org/10.1098/rsif.2021.0349.

Choudhry, A., Arjomandi, M. and Kelso, R. (2015) 'A study of long separation bubble on thick airfoils and its consequent effects', *International Journal of Heat and Fluid Flow*, 52, pp. 84–96. Available at: https://doi.org/10.1016/j.ijheatfluidflow.2014.12.001.

Collison, M.J., Harley, P.X.L. and di Cugno, D. (2017) 'Experimental and Numerical Investigation of Transition Effects on a Low Reynolds Number Airfoil', in *Volume 2B: Turbomachinery*. American Society of Mechanical Engineers. Available at: https://doi.org/10.1115/GT2017-63294.

Counsil, J.N.N. and Goni Boulama, K. (2012) 'Validating the URANS shear stress transport γ −Reθ model for low-Reynolds-number external aerodynamics', *International Journal for Numerical Methods in Fluids*, 69(8), pp. 1411–1432. Available at: https://doi.org/10.1002/fld.2651.

Denny, M. (2009) 'Dynamic soaring: aerodynamics for albatrosses', *European Journal of Physics*, 30(1), pp. 75–84. Available at: https://doi.org/10.1088/0143-0807/30/1/008.

Deshpande, P. and Modani, A. (2019) 'Experimental investigation of fluid–structure interaction in a bird-like flapping wing', *Journal of Fluids and Structures*, 91, p. 102712. Available at: https://doi.org/10.1016/j.jfluidstructs.2019.102712.

Duriez, O. *et al.* (2014) 'How Cheap Is Soaring Flight in Raptors? A Preliminary Investigation in Freely-Flying Vultures', *PLoS ONE*, 9(1), p. e84887. Available at: https://doi.org/10.1371/journal.pone.0084887.

Hájek, J. (2011) 'Parameterization of Airfoils and Its Application in Aerodynamic Optimization'.

Hansen, K.L., Kelso, R.M. and Dally, B.B. (2011) 'Performance Variations of Leading-Edge Tubercles for Distinct Airfoil Profiles', *AIAA Journal*, 49(1), pp. 185–194. Available at: https://doi.org/10.2514/1.J050631.

Harvey, C. *et al.* (2019) 'Wing morphing allows gulls to modulate static pitch stability during gliding', *Journal of The Royal Society Interface*, 16(150), p. 20180641. Available at: https://doi.org/10.1098/rsif.2018.0641.

Harvey, C. and Inman, D.J. (2021) 'Aerodynamic efficiency of gliding birds vs comparable UAVs: a review', *Bioinspiration & Biomimetics*, 16(3), p. 031001. Available at: https://doi.org/10.1088/1748-3190/abc86a.

Helmbold, H.B. and Keune, F. (1943) *Beiträge zur Profilforschung. 5, Theorie des Singularitätenverfahrens*. [München] (Bericht der Ernst-Heinkel-Flugzeugwerke, Seestadt Rostock).

Henningsson, P. and Hedenström, A. (2011) 'Aerodynamics of gliding flight in common swifts', *Journal of Experimental Biology*, 214(3), pp. 382–393. Available at: https://doi.org/10.1242/jeb.050609.

Herzog, K. (1968) 'Anatomie und Flugbiologie der Vögel', in.

Horton, H. (1968) *Laminar separation bubbles in two and three dimensional incompressible flow*. PhD. University of London.

Jung, S. *et al.* (2016) 'An Implementation of Self-Organizing Maps for Airfoil Design Exploration via Multi-Objective Optimization Technique', *Journal of Aerospace Technology and Management*, 8(2), pp. 193–202. Available at: https://doi.org/10.5028/jatm.v8i2.585.

Klän, S. *et al.* (2009) 'Experimental analysis of the flow field over a novel owl based airfoil', *Experiments in Fluids*, 46(5), pp. 975–989. Available at: https://doi.org/10.1007/s00348-008-0600-7.

König, H.E. *et al.* (2016) *Avian Anatomy : Textbook and Colour Atlas*. 2nd edn. Sheffield: 5m Publishing.

Langtry, R.B. *et al.* (2006) 'A Correlation-Based Transition Model Using Local Variables—Part II: Test Cases and Industrial Applications', *Journal of Turbomachinery*, 128(3), pp. 423–434. Available at: https://doi.org/10.1115/1.2184353.

Lazos, B.S. (2005) 'Biologically Inspired Fixed-Wing Configuration Studies', *Journal of Aircraft*, 42(5), pp. 1089–1098. Available at: https://doi.org/10.2514/1.10496.

Lees, J.J., Dimitriadis, G. and Nudds, R.L. (2016) 'The influence of flight style on the aerodynamic properties of avian wings as fixed lifting surfaces', *PeerJ*, 4, p. e2495. Available at: https://doi.org/10.7717/peerj.2495.

Lentink, D. *et al.* (2007) 'How swifts control their glide performance with morphing wings', *Nature*, 446(7139), pp. 1082–1085. Available at: https://doi.org/10.1038/nature05733.

Liu, T. *et al.* (2006) 'Avian Wing Geometry and Kinematics', *AIAA Journal*, 44(5), pp. 954–963. Available at: https://doi.org/10.2514/1.16224.

Loseille, A. *et al.* (2007) 'Achievement of Global Second Order Mesh Convergence for Discontinuous Flows with Adapted Unstructured Meshes', in *18th AIAA Computational Fluid Dynamics Conference*. Reston, Virigina: American Institute of Aeronautics and Astronautics. Available at: https://doi.org/10.2514/6.2007-4186.

Mair, W.A. (1961) 'Aerofoil Sections. By F. W. R IEGELS . Translated from the German by D. G. RANDALL. London: Butterworths, 1961. 281 pp. £10.', *Journal of Fluid Mechanics*, 11(04), p. 637. Available at: https://doi.org/10.1017/S0022112061220799.

McGhee, R.J. and Walker, B.S. (1989) 'Performance Measurements of an Airfoil at Low Reynolds Numbers', in, pp. 131–145. Available at: https://doi.org/10.1007/978-3-642-84010-4_11.

Menter, F.R. *et al.* (2006) 'A Correlation-Based Transition Model Using Local Variables—Part I: Model Formulation', *Journal of Turbomachinery*, 128(3), p. 413. Available at: https://doi.org/10.1115/1.2184352.

Michal, T.R. *et al.* (2020) 'Comparing Unstructured Adaptive Mesh Solutions for the High Lift Common Research Model Airfoil', in *AIAA AVIATION 2020 FORUM*. Reston, Virginia: American Institute of Aeronautics and Astronautics. Available at: https://doi.org/10.2514/6.2020-3219.

Nachtigall, W. and Wieser, J. (1966) 'Profilmessungen am Taubenfl�gel', *Zeitschrift f�r Vergleichende Physiologie*, 52(4), pp. 333–346. Available at: https://doi.org/10.1007/BF00302288.

Norberg, U.M. (1990) *Vertebrate Flight*. Berlin, Heidelberg: Springer Berlin Heidelberg. Available at: https://doi.org/10.1007/978-3-642-83848-4.

Norberg, U.M.L. (2006) 'Flight And Scaling Of Flyers In Nature', *WIT Transactions on State-of-the-art in Science and Engineering*, 3.

Omar, A., Rahuma, R. and Emhemmed, A. (2020) 'Numerical Investigation on Aerodynamic Performance of Bird's Airfoils', *Journal of Aerospace Technology and Management* [Preprint], (12). Available at: https://doi.org/10.5028/jatm.v12.1182.

van Oorschot, B.K., Mistick, E.A. and Tobalske, B.W. (2016) 'Aerodynamic consequences of wing morphing during emulated take-off and gliding in birds', *Journal of Experimental Biology* [Preprint]. Available at: https://doi.org/10.1242/jeb.136721.

Pauley, L.L., Moin, P. and Reynolds, W.C. (1990) 'The structure of two-dimensional separation', *Journal of Fluid Mechanics*, 220, pp. 397–411. Available at: https://doi.org/10.1017/S0022112090003317.

Pennycuick, C.J. and Lighthill, M.J. (1982) 'The flight of petrels and albatrosses (procellariiformes), observed in South Georgia and its vicinity', *Philosophical Transactions of the Royal Society of London. B, Biological Sciences*, 300(1098), pp. 75–106. Available at: https://doi.org/10.1098/rstb.1982.0158.

Rader, J.A. *et al.* (2020) 'Functional Morphology of Gliding Flight II. Morphology Follows Predictions of Gliding Performance', *Integrative and Comparative Biology*, 60(5), pp. 1297–1308. Available at: https://doi.org/10.1093/icb/icaa126.

Raul, V. and Leifsson, L. (2021) 'Surrogate-based aerodynamic shape optimization for delaying airfoil dynamic stall using Kriging regression and infill criteria', *Aerospace Science and Technology*, 111, p. 106555. Available at: https://doi.org/10.1016/j.ast.2021.106555.

Richardson, P.L. (2011) 'How do albatrosses fly around the world without flapping their wings?', *Progress in Oceanography*, 88(1–4), pp. 46–58. Available at: https://doi.org/10.1016/j.pocean.2010.08.001.

Rosén, M. and Hedenström, A. (2001) 'Gliding flight in a jackdaw: a wind tunnel study', *Journal of Experimental Biology*, 204(6), pp. 1153–1166. Available at: https://doi.org/10.1242/jeb.204.6.1153.

Ruck, S. and Oertel, H. (2010) 'Fluid–structure interaction simulation of an avian flight model', *Journal of Experimental Biology*, 213(24), pp. 4180–4192. Available at: https://doi.org/10.1242/jeb.041285.

Sachs, G. *et al.* (2012) 'Flying at No Mechanical Energy Cost: Disclosing the Secret of Wandering Albatrosses', *PLoS ONE*, 7(9), p. e41449. Available at: https://doi.org/10.1371/journal.pone.0041449.

Sakamoto, K.Q. *et al.* (2013) 'Heart rate and estimated energy expenditure of flapping and gliding in black-browed albatrosses', *Journal of Experimental Biology* [Preprint]. Available at: https://doi.org/10.1242/jeb.079905.

Schoombie, S., Wilson, R. and Ryan, P. (2023) 'Wind driven effects on the fine-scale flight behaviour of dynamic soaring wandering albatrosses', *Marine Ecology Progress Series*, WIND. Available at: https://doi.org/10.3354/meps14265.

Selig, M.S. and Guglielmo, J.J. (1997) 'High-Lift Low Reynolds Number Airfoil Design', *Journal of Aircraft*, 34(1), pp. 72–79. Available at: https://doi.org/10.2514/2.2137.

Shan, H., Jiang, L. and Liu, C. (2005) 'Direct numerical simulation of flow separation around a NACA 0012 airfoil', *Computers & Fluids*, 34(9), pp. 1096–1114. Available at: https://doi.org/10.1016/j.compfluid.2004.09.003.

Shen, X. *et al.* (2017) 'Computational methods for investigation of surface curvature effects on airfoil boundary layer behavior', *Journal of Algorithms & Computational Technology*, 11(1), pp. 68–82. Available at: https://doi.org/10.1177/1748301816665527.

Siemens Digital Industries Software (2022a) 'Simcenter STAR-CCM+ User Guide, version 2022.1', in *Adaptive Mesh General Workflow*. Siemens, pp. 3283–3284.

Siemens Digital Industries Software (2022b) 'Simcenter STAR-CCM+ User Guide, version 2022.1', in *The SHERPA Algorithm*. Siemens, pp. 6988–6989.

Sobieczky, H. (1997) 'Geometry Generator for CFD and Applied Aerodynamics', in *New Design Concepts for High Speed Air Transport*. Vienna: Springer Vienna, pp. 137–157. Available at: https://doi.org/10.1007/978-3-7091-2658-5_9.

Sobieczky, H. (1999) 'Parametric Airfoils and Wings', in, pp. 71–87. Available at: https://doi.org/10.1007/978-3-322-89952-1_4.

Storn, R. and Price, K. (1997) 'Differential Evolution – A Simple and Efficient Heuristic for global Optimization over Continuous Spaces', *Journal of Global Optimization*, 11(4), pp. 341–359. Available at: https://doi.org/10.1023/A:1008202821328.

Tank, J., Smith, L. and Spedding, G.R. (2017) 'On the possibility (or lack thereof) of agreement between experiment and computation of flows over wings at moderate Reynolds number', *Interface Focus*, 7(1), p. 20160076. Available at: https://doi.org/10.1098/rsfs.2016.0076.

Tucker, V. (1972) 'Metabolism during flight in the laughing gull, Larus atricilla', *American Journal of Physiology-Legacy Content*, 222(2), pp. 237–245. Available at: https://doi.org/10.1152/ajplegacy.1972.222.2.237.

Usherwood, J.R. *et al.* (2020) ‘High aerodynamic lift from the tail reduces drag in gliding raptors’, *Journal of Experimental Biology*, 223(3). Available at: https://doi.org/10.1242/jeb.214809.

Volkers, D.F. (1977) ‘Preliminary results of windtunnel measurements on some airfoil sections at Reynolds numbers between 0.6 x 10^5 and 5.0 x 10^5’, in.

Wackers, J. *et al.* (2017) ‘Can adaptive grid refinement produce grid-independent solutions for incompressible flows?’, *Journal of Computational Physics*, 344, pp. 364–380. Available at: https://doi.org/10.1016/j.jcp.2017.04.077.

Wagner, H. *et al.* (2017) ‘Features of owl wings that promote silent flight’, *Interface Focus*, 7(1), p. 20160078. Available at: https://doi.org/10.1098/rsfs.2016.0078.

Waldrop, L.D. *et al.* (2020) ‘Functional Morphology of Gliding Flight I: Modeling Reveals Distinct Performance Landscapes Based on Soaring Strategies’, *Integrative and Comparative Biology*, 60(5), pp. 1283–1296. Available at: https://doi.org/10.1093/icb/icaa114.

Walters, D.K. and Cokljat, D. (2008) ‘A Three-Equation Eddy-Viscosity Model for Reynolds-Averaged Navier–Stokes Simulations of Transitional Flow’, *Journal of Fluids Engineering*, 130(12). Available at: https://doi.org/10.1115/1.2979230.

Withers, P.C. (1981) ‘An Aerodynamic Analysis of Bird Wings as Fixed Aerofoils’, *Journal of Experimental Biology*, 90(1), pp. 143–162. Available at: https://doi.org/10.1242/jeb.90.1.143.

Appendix A – Optimizer comparison for calculating PARSEC Parameters

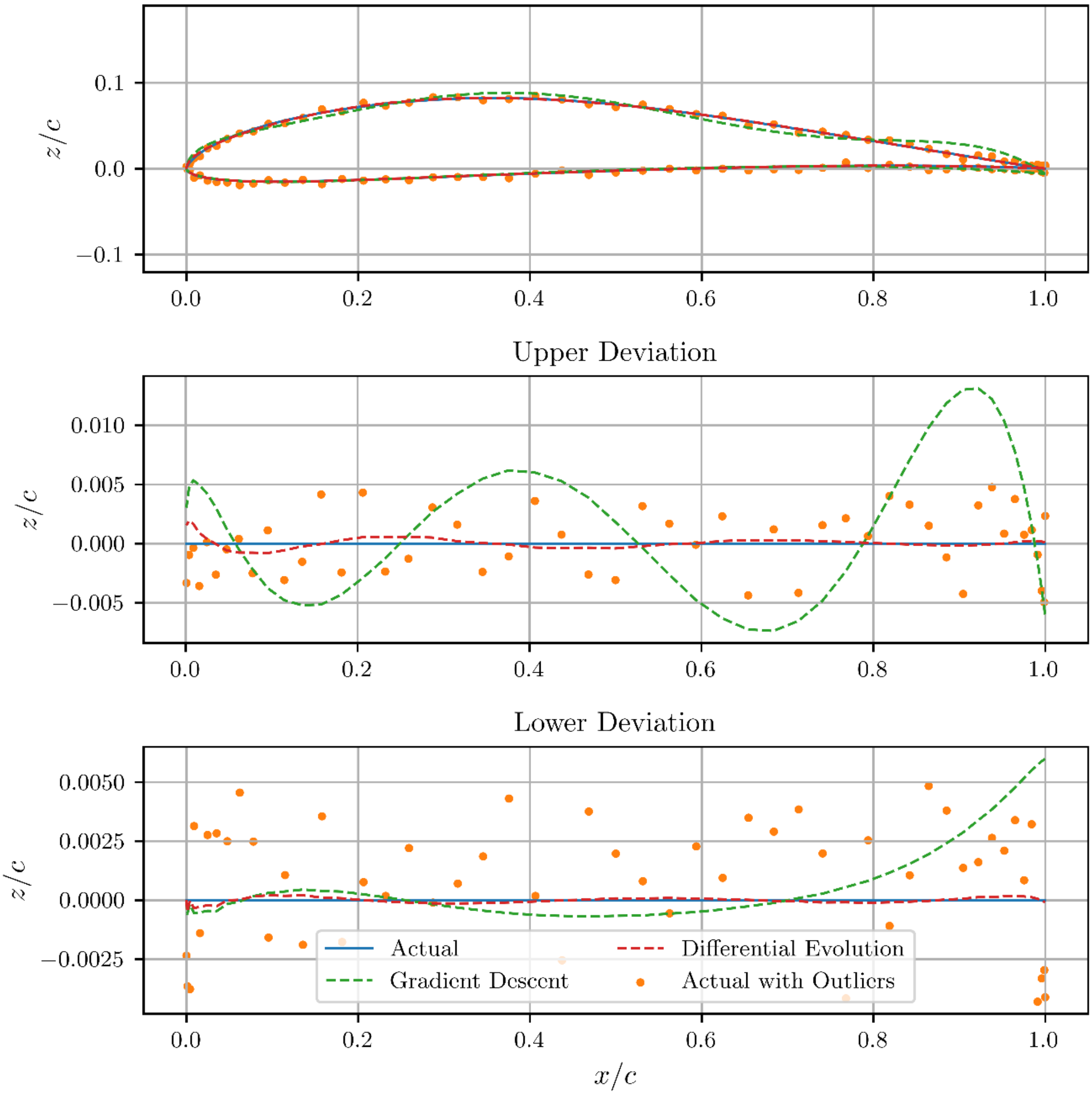

Figure 59: E387 GD: 0.25s, DE: 38.57s

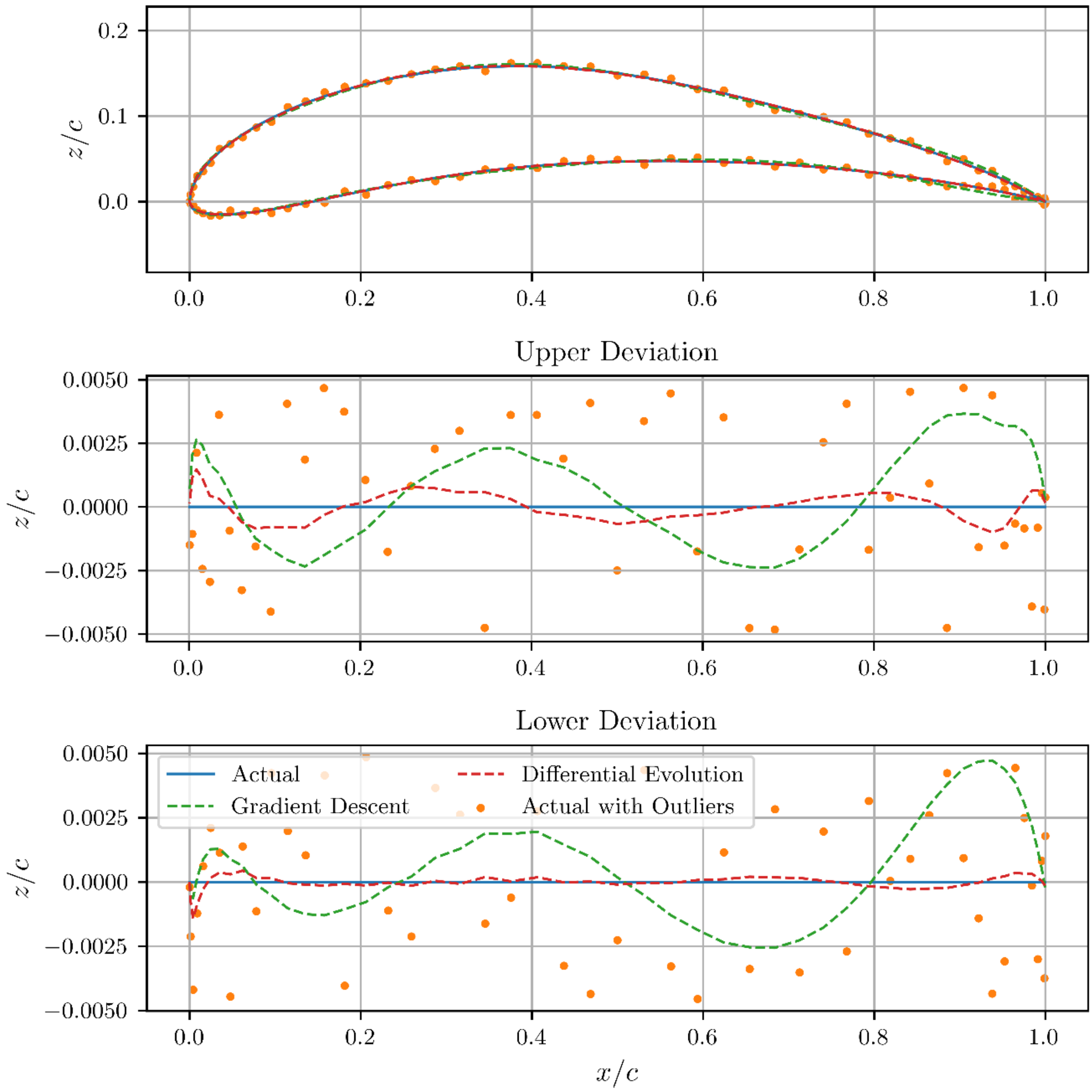

Figure 60: E423 GD: 0.14s, DE: 13.25s

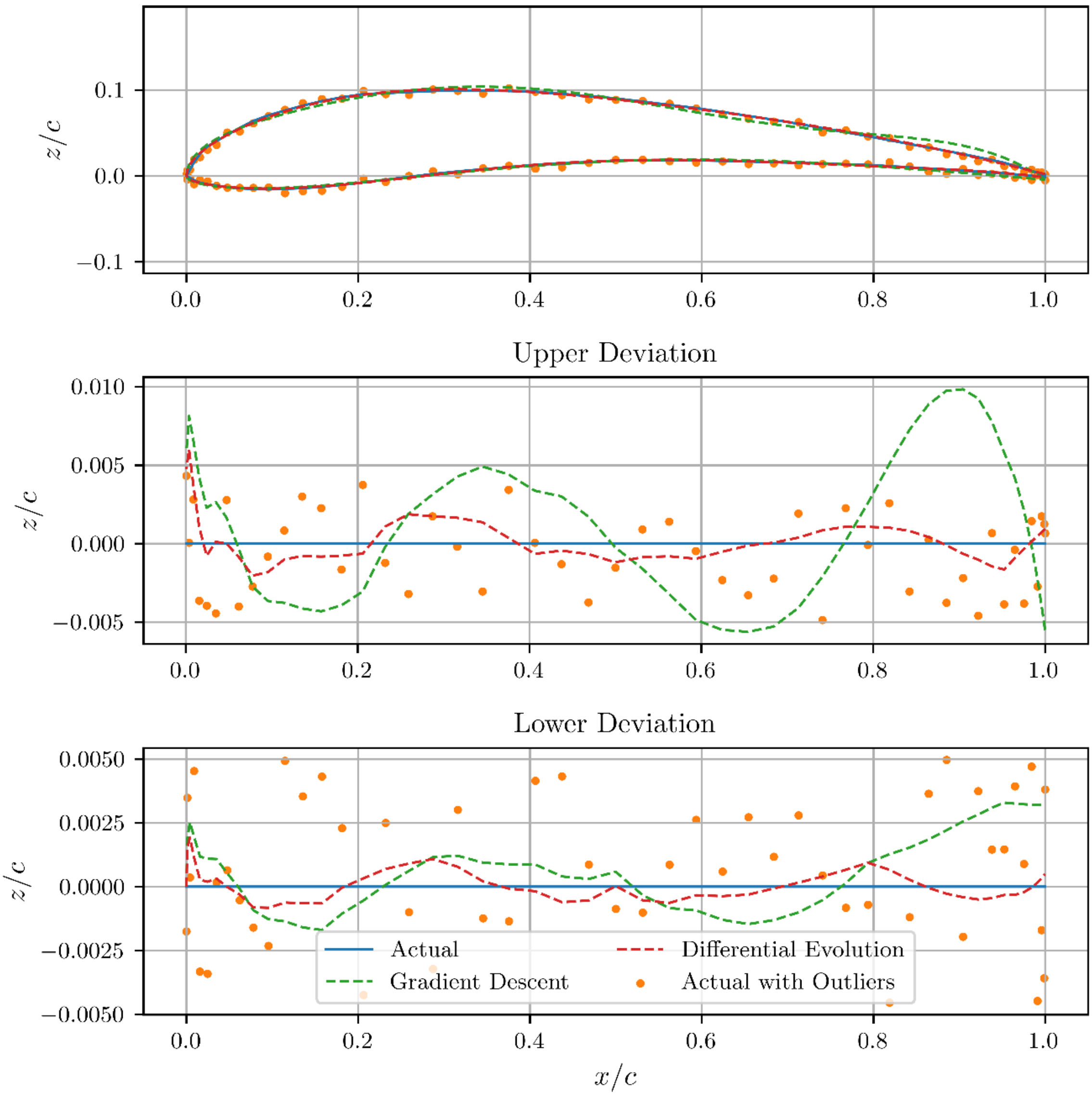

Figure 61: GOE176 GD: 0.20s, DE: 11.10s

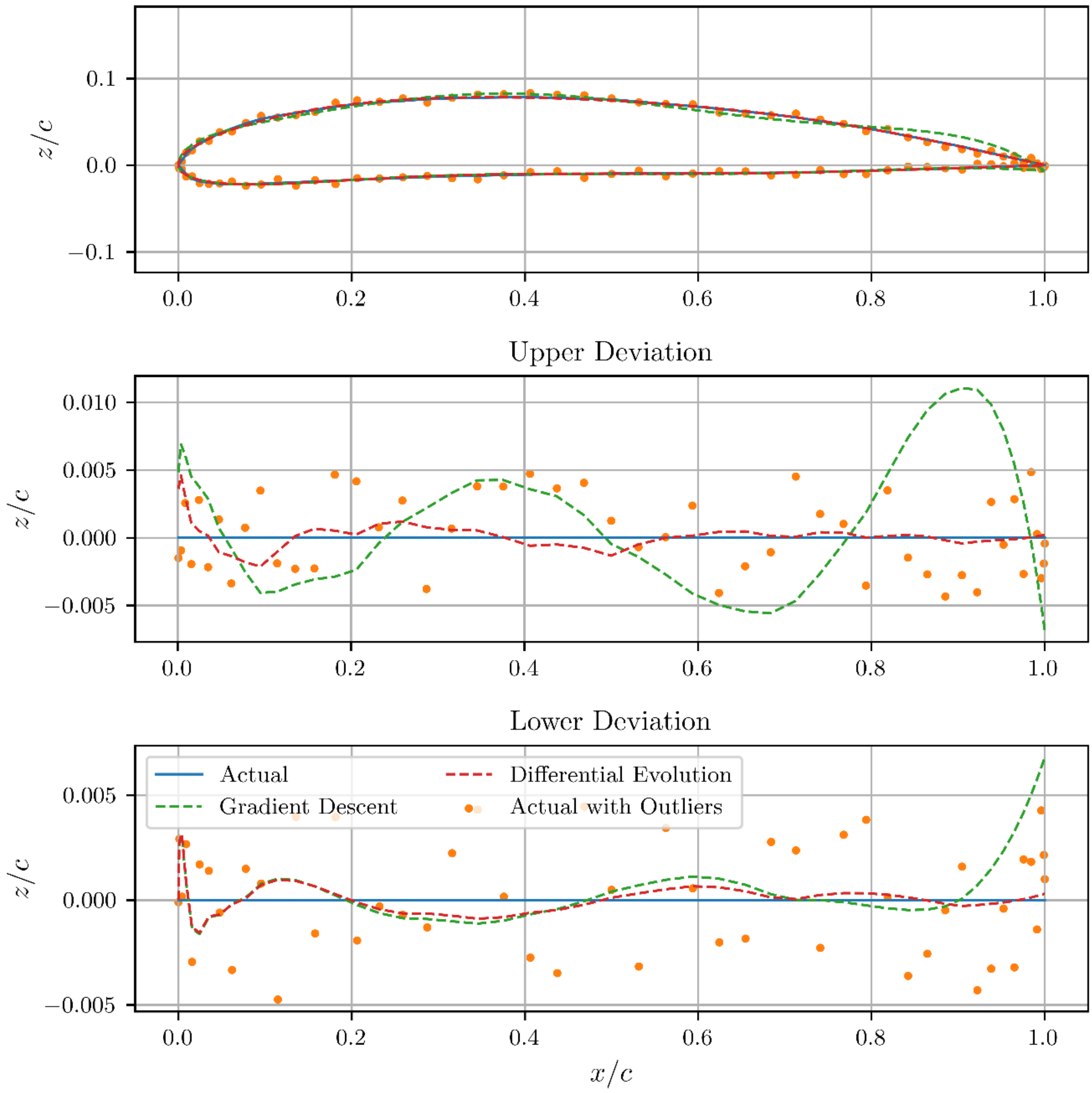

Figure 62: GOE676 GD: 0.18s, DE: 11.68s

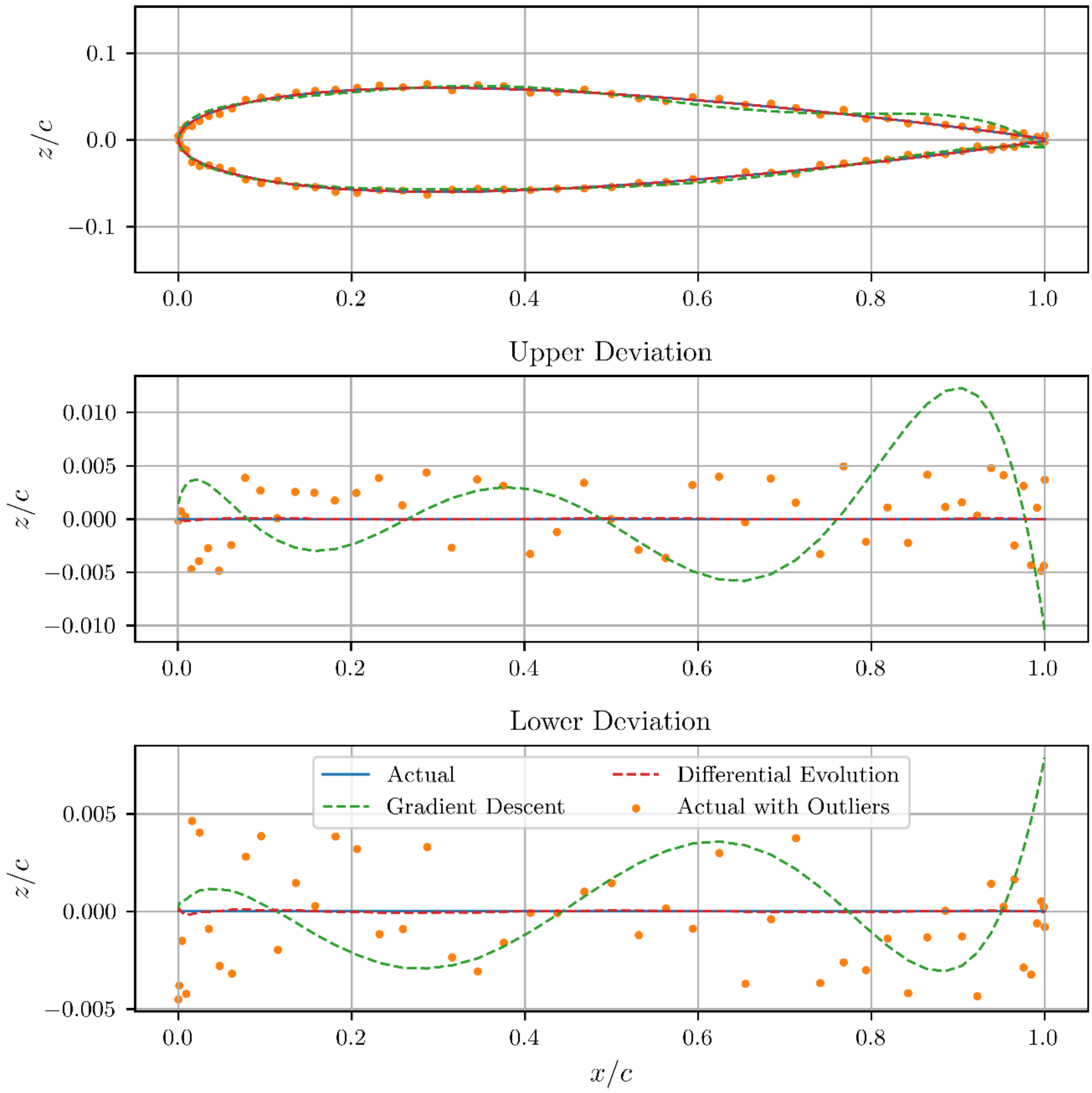

Figure 63: NACA0012 GD: 0.14s, DE: 15.01s

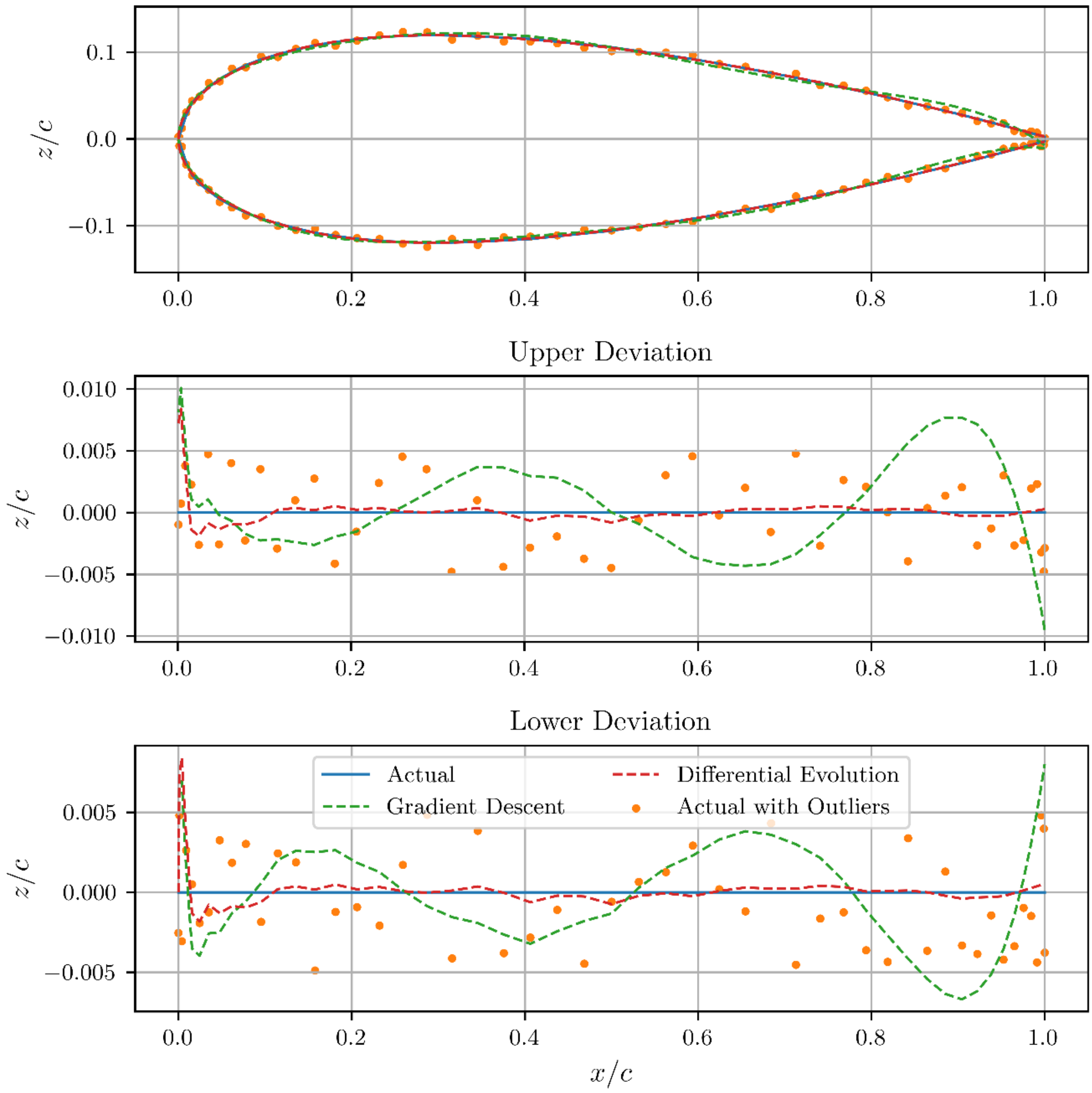

Figure 64: NACA0024 GD: 0.44s, DE: 14.93s

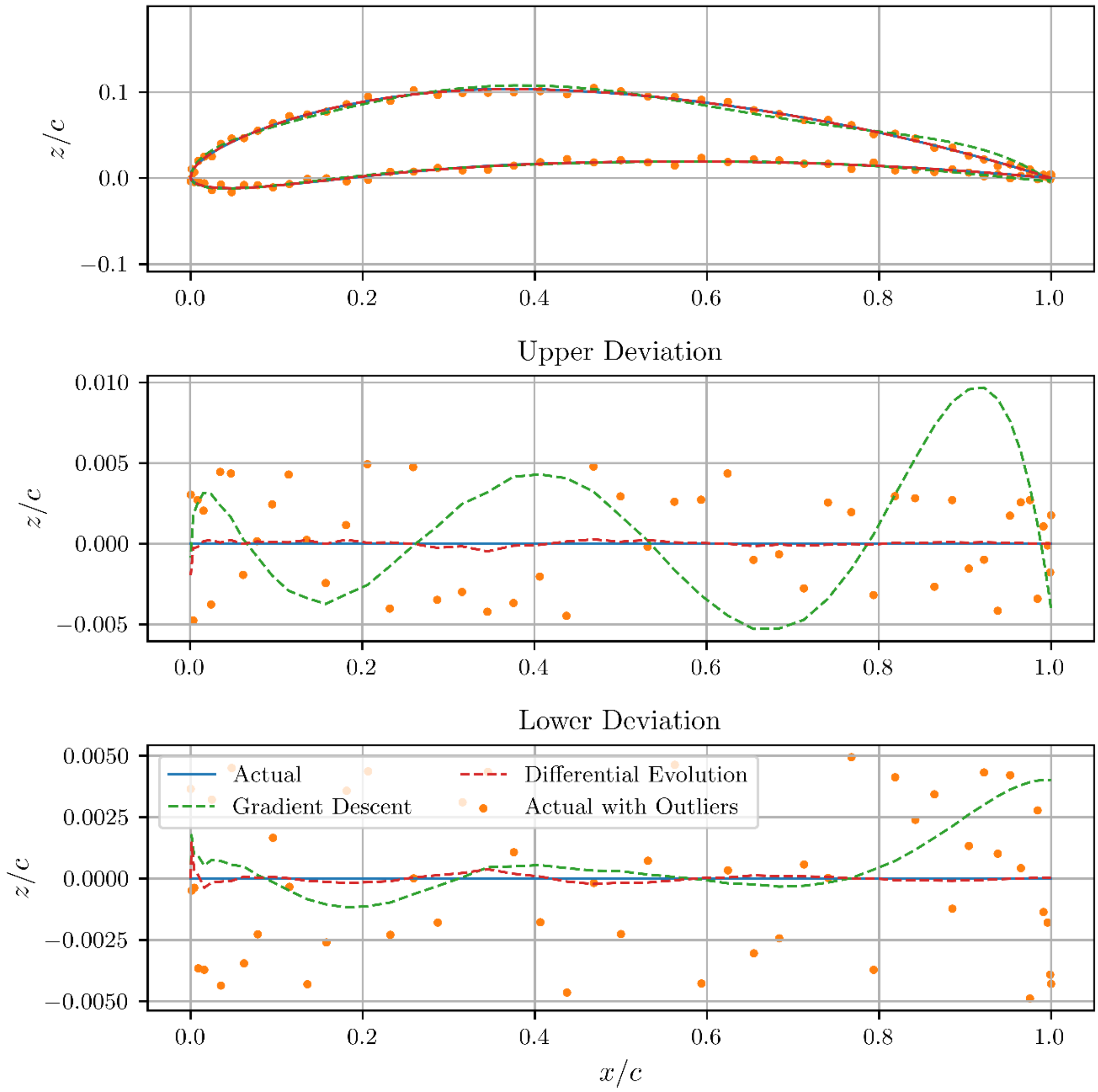

Figure 65: NACA6409, GD: 0.18s, 14.59s

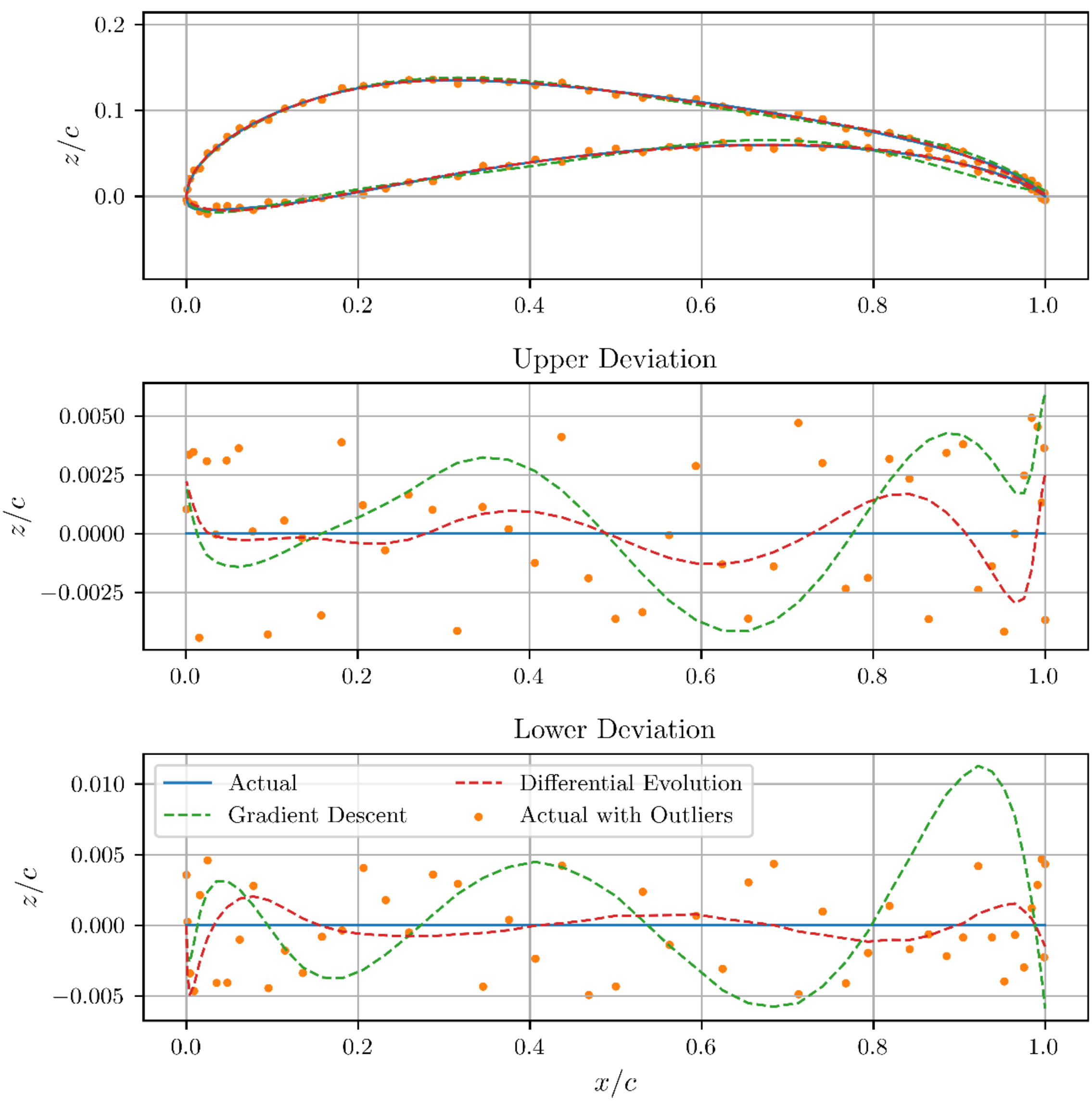

Figure 66: S1223, GD: 0.20s, DE: 17.42s

Appendix B – Airfoils of the GHA

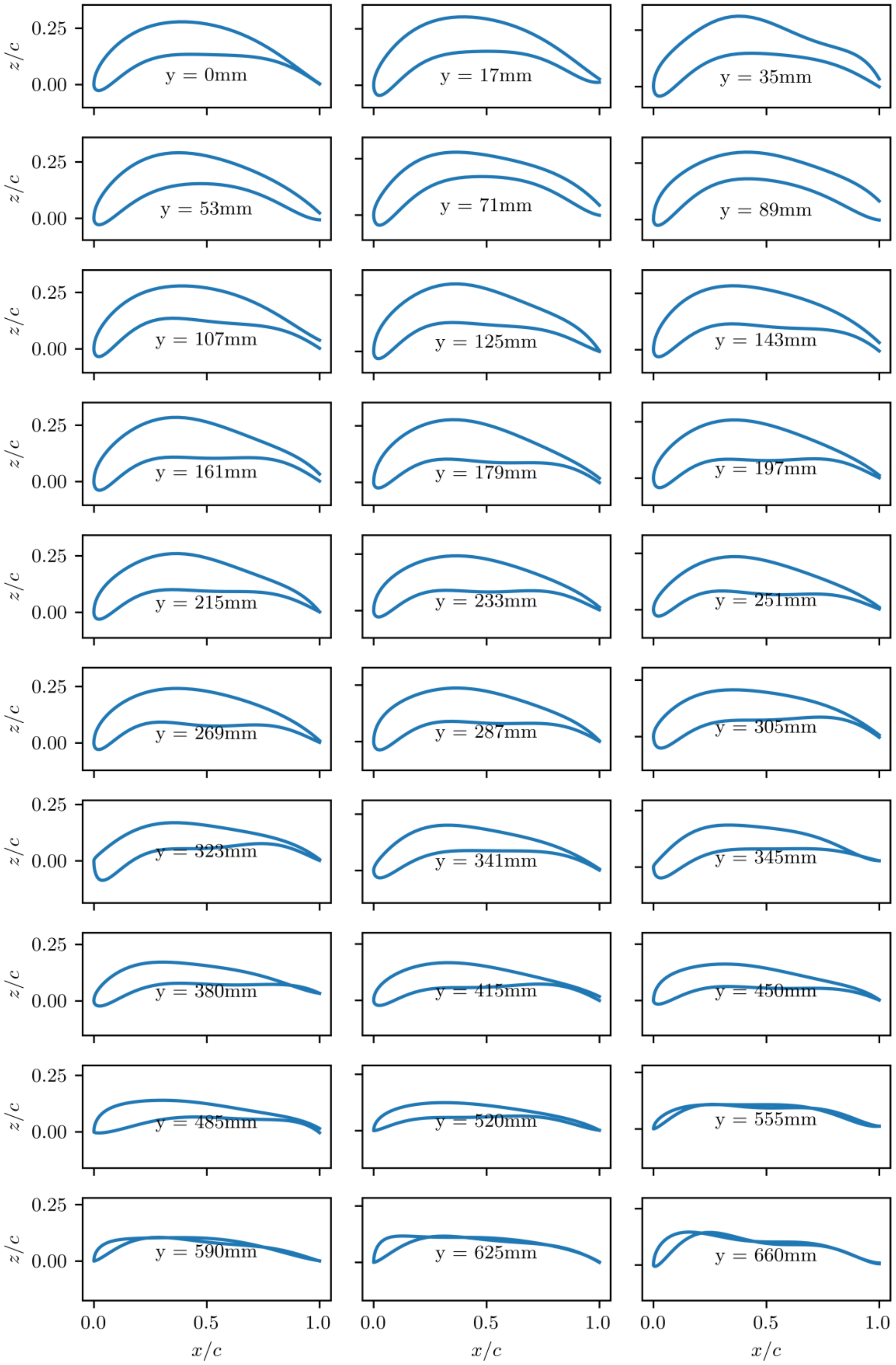

Figure 67: The airfoils created using the PARSEC method for different spanwise locations

y	rleup	alphate	betate	zte	deltazte	xup	zup	zxxup	xlo	zlo	zxxlo	rlelo
0	0.253	-33.791	-1.454	0.003	0.002	0.390	0.278	-1.734	0.427	0.134	-0.636	0.079
17	0.242	-13.579	40.000	0.020	0.014	0.397	0.303	-1.834	0.505	0.150	-0.584	0.195
35	0.305	-45.348	29.674	0.016	0.034	0.380	0.311	-3.667	0.433	0.147	-1.194	0.166
53	0.256	-22.564	40.000	0.008	0.030	0.376	0.291	-2.125	0.474	0.154	-1.292	0.084
71	0.187	-27.954	35.882	0.021	0.045	0.365	0.278	-1.890	0.478	0.171	-1.029	0.190
89	0.388	-25.882	37.417	0.040	0.084	0.414	0.298	-1.976	0.419	0.180	-1.764	0.082
107	0.260	-29.730	-6.255	0.021	0.036	0.390	0.279	-1.622	0.351	0.136	-2.127	0.127
125	0.365	-36.959	36.922	0.002	0.003	0.363	0.299	-2.704	0.349	0.128	-1.728	0.116
143	0.320	-41.055	4.581	0.013	0.037	0.353	0.283	-1.915	0.348	0.114	-1.918	0.102
161	0.290	-38.930	11.994	0.018	0.031	0.364	0.284	-2.544	0.355	0.108	-1.330	0.147
179	0.345	-36.476	3.231	0.008	0.020	0.354	0.277	-2.366	0.325	0.102	-1.953	0.075
197	0.227	-31.647	13.369	0.007	0.011	0.358	0.258	-2.273	0.332	0.084	-1.534	0.163
215	0.283	-38.779	23.718	0.002	0.000	0.365	0.260	-2.434	0.348	0.100	-1.395	0.099
233	0.286	-31.744	16.317	0.009	0.012	0.367	0.242	-1.812	0.698	0.088	-1.166	0.090
251	0.140	-28.502	15.558	0.007	0.008	0.359	0.235	-2.222	0.712	0.070	-0.946	0.089
269	0.257	-32.650	18.577	0.006	0.008	0.367	0.241	-1.647	0.298	0.092	-2.389	0.097
287	0.331	-37.855	15.333	0.002	0.003	0.366	0.237	-1.758	0.343	0.089	-1.563	0.127
305	0.135	-37.056	0.797	0.001	0.010	0.354	0.207	-1.365	0.430	0.072	-0.001	0.198
323	0.025	-29.704	14.836	0.004	0.005	0.357	0.169	-1.618	0.411	0.054	0.000	0.489
341	0.075	-31.648	3.332	0.004	0.005	0.328	0.201	-1.939	0.426	0.088	-0.448	0.094
345	0.022	-6.079	-10.956	0.028	0.000	0.333	0.186	-1.488	0.476	0.080	-0.001	0.178
380	0.118	-17.036	-18.325	0.033	0.000	0.304	0.172	-1.401	0.381	0.078	-1.032	0.049
415	0.147	-26.922	-2.365	0.008	0.018	0.330	0.167	-1.417	0.393	0.056	-0.001	0.050
450	0.229	-28.454	12.030	0.003	0.002	0.316	0.162	-1.264	0.328	0.062	-1.133	0.029
485	0.221	-34.398	-8.751	0.006	0.019	0.302	0.140	-0.864	0.449	0.066	-0.826	0.003
520	0.125	-16.537	20.653	0.002	0.000	0.312	0.124	-0.855	0.353	0.059	-0.001	0.000
555	0.081	-0.009	-11.593	0.012	0.000	0.505	0.107	-0.288	0.263	0.108	-2.155	0.000
590	0.169	-12.594	-8.414	0.001	0.001	0.382	0.104	-0.296	0.286	0.105	-1.981	0.000
625	0.346	-30.218	0.287	0.001	0.002	0.366	0.111	0.000	0.309	0.116	-1.774	0.000

Appendix C – Mesh Independence Study Prism Layer Mesher

For each mesh, the cell counts, denoted by N_1, N_2, and N_3, where the subscript, 1, refers to the fine mesh and the subscript, 3, refers to the coarsest mesh is used to calculate a representative cell size as,

$$h = \left(\frac{1}{N}V\right)^{\frac{1}{3}} \tag{28}$$

where V is the volume of the domain and N is the number of cells in the mesh. The refinement factor is then calculated as $r = h_{\text{fine}}/h_{\text{coarse}}$ between two successive mesh refinements. It is suggested that the refinement value be at least a value of 1.3. Now, $h_1 < h_2 < h3$, and having $r_{21} = h_2/h_1$ and $r_{32} = h_3/h_2$, the apparent order of the method is calculated as,

$$p = \frac{1}{\ln(r_{21})}\left|\ln\left|\frac{\epsilon_{32}}{\epsilon_{21}}\right| + q(p)\right| \tag{29}$$

$$q(p) = \ln\left(\frac{r_{21}^{p} - s}{r_{21}^{p} - s}\right) \tag{30}$$

$$s = 1 \times \left(\frac{\epsilon_{32}}{\epsilon_{21}}\right) \tag{31}$$

where $\epsilon_{32} = \phi_3 - \phi_2$ and $\epsilon_{21} = \phi_2 - \phi_1$, and ϕ is simply the engineering quantity of interest. The apparent order, p, is solved iteratively using equations (29) and (30). Negative values of s indicate oscillatory convergence. Next, the extrapolated values are calculated as,

$$\phi_{\text{ext}}^{21} = \frac{r_{21}^{p}\phi_1 - \phi_2}{r_{21}^{p} - 1} \tag{32}$$

And the value, ϕ_{ext}^{32} is calculated similarly. The following errors are then calculated, starting with the approximate relative error,

$$e_a^{21} = \left|\frac{\phi_1 - \phi_2}{\phi_1}\right| \tag{33}$$

and the extrapolated relative error,

$$e_{\text{ext}}^{21} = \left|\frac{\phi_{\text{ext}}^{21} - \phi_1}{\phi_{\text{ext}}^{21}}\right| \tag{34}$$

and finally, the fine-grid convergence index,

$$\mathrm{GCI}_{\mathrm{fine}}^{21} = \frac{1.25 e_a^{21}}{r_{21}^{p} - 1} \tag{35}$$

The results comparing the pressure distributions, separation locations and C_L and C_D values for the first iteration of the mesh refinement are shown in Figure 68 and Figure 69 and Table 7.

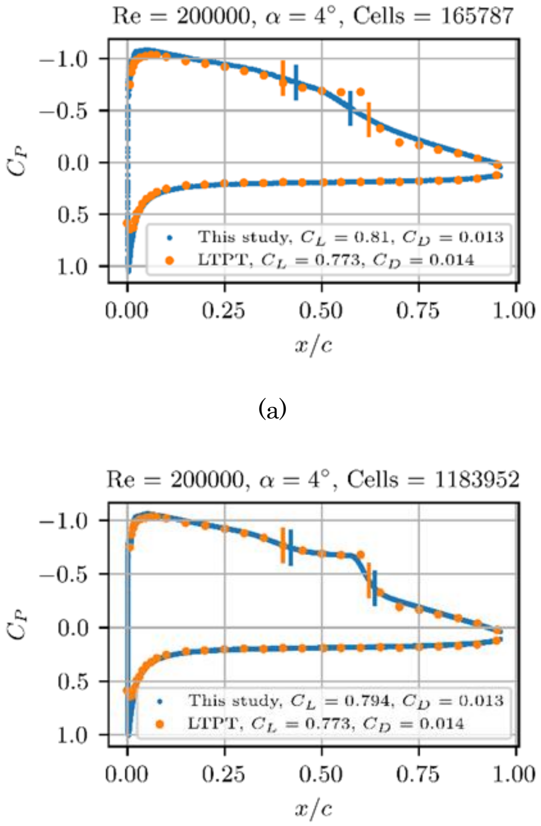

(a)

(b)

(c)

Figure 68: Pressure distributions for (a) coarse mesh (b) medium mesh and (c) fine mesh showing the separation and reattachment locations and C_L and C_D values.

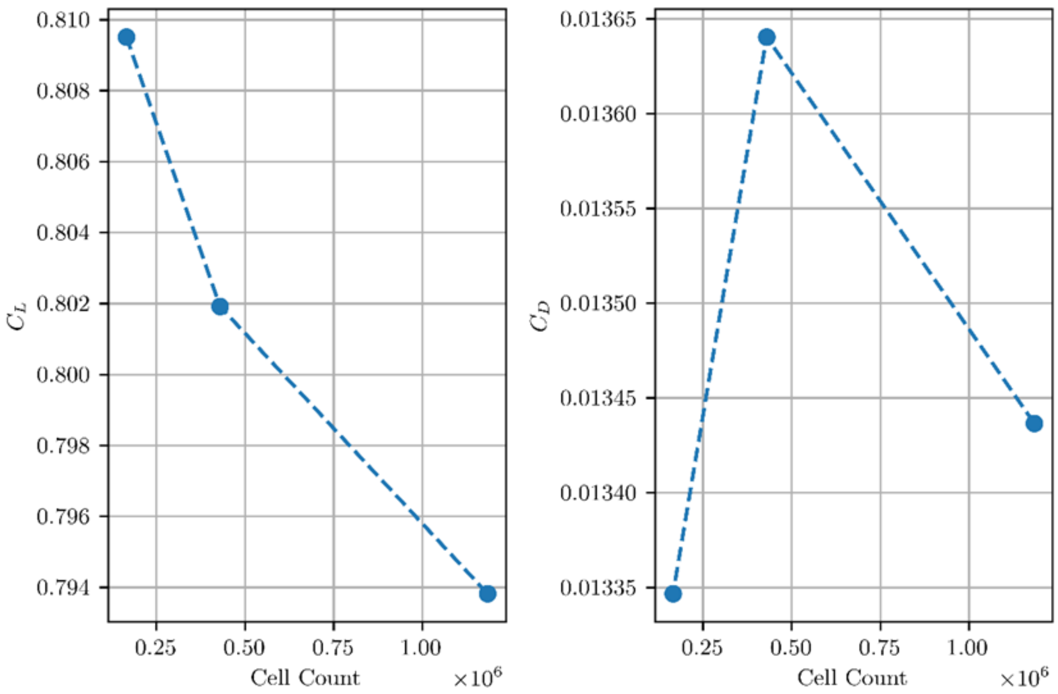

Figure 69: Change in C_L and C_D for the successive refinements

Table 7: Quantities calculated for the mesh independence study performed at $\alpha = 4°$ and $\mathrm{Re} = 2 \times 10^5$

	C_L	C_D
N	[1183952, 429567, 165787]	[1183952, 429567, 165787]
h_1, h_2, h_3	[0.01508, 0.02114, 0.0290]	[0.01508, 0.02114, 0.0290]
r_{21}, r_{32}	[1.4021, 1.3735]	[1.4021, 1.3735]
ϕ_1, ϕ_2, ϕ_3	[0.7938, 0.8019, 0.8095]	[0.0134, 0.0136, 0.0133]
e_{21}, e_{32}	[0.0081, 0.0076]	[0.0002, -0.0003]
s	1	-1
p	0.0027	1.1209
$\phi_{\mathrm{ext}}^{21}, \phi_{\mathrm{ext}}^{31}$	[-8.2243, -8.208]	[0.0130, 0.0143]
e_a^{21}	0.0010	0.0015
e_{ext}^{21}	1.0975	0.0498
$\mathrm{GCI}_{\mathrm{fine}}^{21}$	14.2005	0.0419

From Table 7 the solution of the finest mesh was not independent of the mesh, indicated by a grid convergence index (GCI) value of 14.2005, which should be almost zero for a mesh-independent solution. Increasing the number of cells in the mesh was not a viable option, since the mesh used for the optimization would have been too large when considering the number of simulations required. The choice was therefore made to investigate the difference in the meshing strategies used.

The initial meshes made use of the so-called prism layer mesher which extrudes prismatic cells from the surface to which it is applied. The prismatic cells near the trailing edge of the wing were visually inspected, and it was evident that these cells collapsed near the trailing edge as shown in Figure 70a The so-called advancing layer mesher was used instead which eliminated the collapsing prismatic cells, as shown in Figure 70b

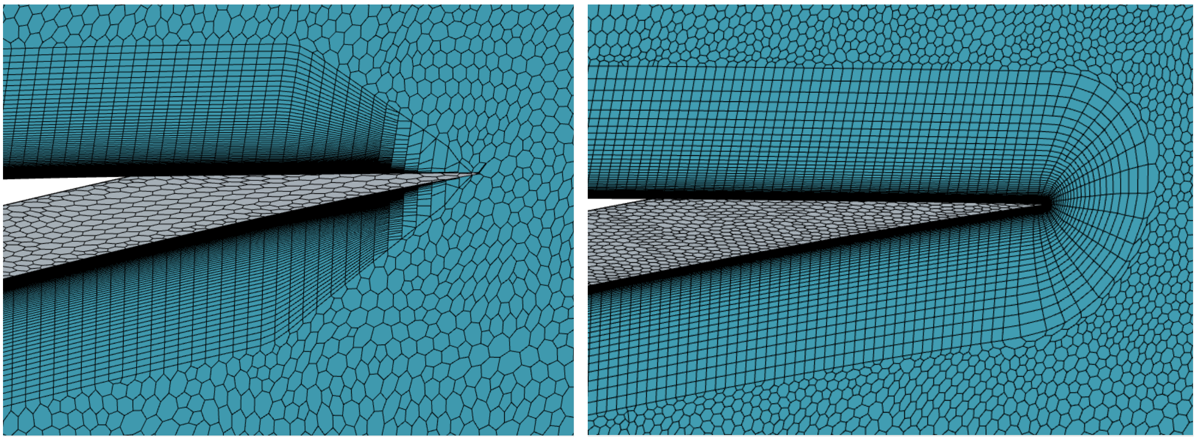

(a)

(b)

Figure 70: The trailing edge prismatic cells using the (a) prism layer mesher and (b) the advancing layer mesher.

For the new meshes generated by the advancing layer mesh, a new mesh independence study was performed to investigate whether improved trailing edge prismatic cells caused the prior simulations to be dependent on the mesh. Furthermore, the number of prism layers were changed during the mesh refinement to ensure that cell aspect ratios and sizes between the final prism layer cell and the first core polyhedral cell were uniform. For the fine mesh, 80 prism layers were used, for the medium mesh, 50 prism layers were used and for the coarse mesh, 30 prism layers were used.

Appendix D – Mesh Independence Study Advancing Layer Mesh

The pressure distribution results showing the laminar separation and turbulent reattachment location compared to experimental results are shown in Figure 59. The variation in the aerodynamic coefficients of interest, C_L and C_D as functions of the mesh size is shown in Figure 60, and the calculation of the grid convergence index is shown in Table 9.

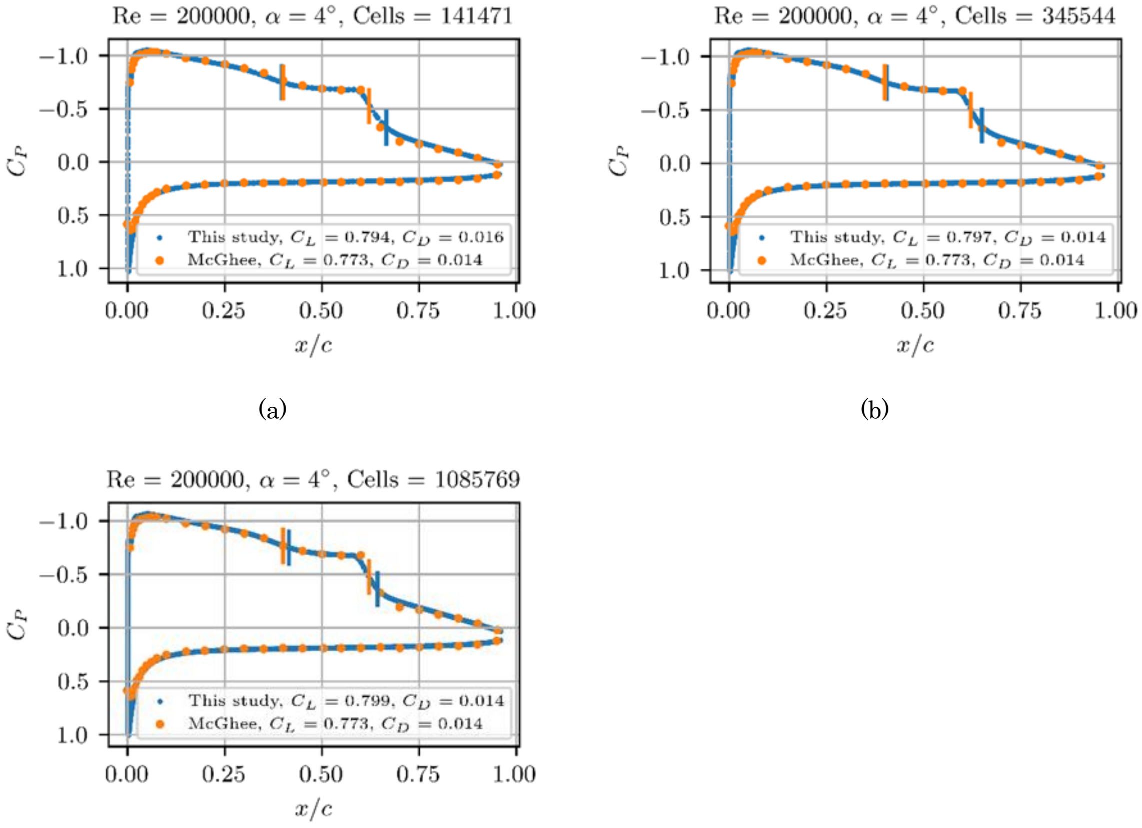

(a)

(b)

(c)

Figure 71: Pressure distributions for (a) coarse mesh (b) medium mesh and (c) fine mesh showing the separation and reattachment locations and C_L and C_D values.

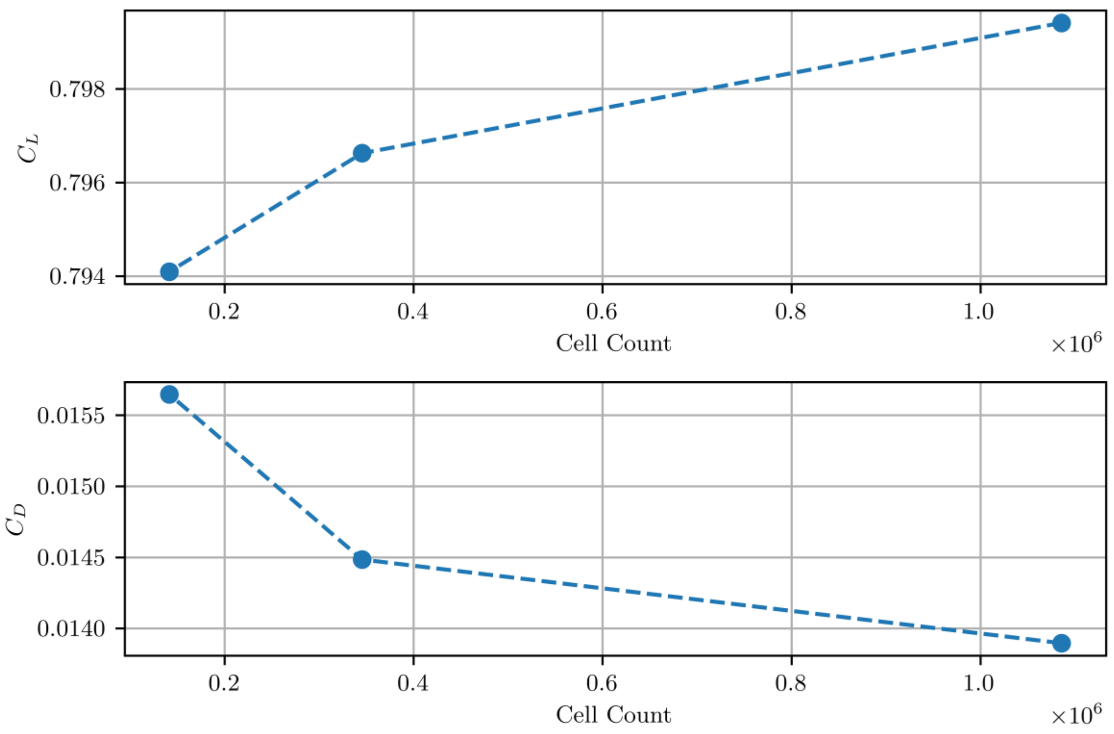

Figure 72: Change in C_L and C_D for the successive refinements

Table 8: Quantities calculated for the mesh independence study performed at $\alpha = 4°$ and Re $= 2 \times 10^5$

	C_L	C_D
N	[1085769, 345544, 141471]	[085769, 345544, 141471]
h_1, h_2, h_3	[0.0156, 0.02273, 0.0303]	[0.0156, 0.02273, 0.0306]
r_{21}, r_{32}	[1.465, 1.345]	[1.465, 1.345]
ϕ_1, ϕ_2, ϕ_3	[0.7994, 0.7966, 0.7941]	[0.0139, 0.0145, 0.0156]
e_{21}, e_{32}	[-0.0028, -0.0025]	[0.0005, 0.0012]
s	1	1
p	0.4535	2.7886
$\phi_{\text{ext}}^{21}, \phi_{\text{ext}}^{31}$	[0.8141, 0.8141]	[0.0136, 0.0136]
e_a^{21}	0.0035	0.0423
0.0215	0.00661	0.0498
$\text{GCI}_{\text{fine}}^{21}$	0.0230	0.0279

The GCI values were in the order of 2% (Table 8) which was a significant improvement and viable to use. Therefore, the mesh to be used was the medium mesh, containing ~ 350k cells. This would be the most practical compromise between mesh size (keeping the final mesh size used in the optimization in mind) and accurate results. The advancing layer mesh also improved on the pressure distributions which correlated better with the experimental data than the prism layer mesher. As a final check, an angle of attack sweep using $\alpha = 0°, 2°, 4°, 6°, 8°$ was done to verify whether results are applicable to a range of flow directions.

Appendix E – JAVA macro used for geometry updating

```
// Simcenter STAR-CCM+ macro: getParamsToCSV.java
// Written by Simcenter STAR-CCM+ 17.02.007
package macro;

import java.util.*;
import java.lang.Math;
import Jama.*;
import java.io.*;


import star.common.*;
import star.base.neo.*;
import star.vis.*;
import star.cadmodeler.*;
import star.meshing.*;

public class PARSEC_update_2d extends StarMacro {

  public void execute() {

    Simulation Sim = getActiveSimulation();

    // Root Airfoil

    ScalarGlobalParameter ParAlpha_te = ((ScalarGlobalParameter)
Sim.get(GlobalParameterManager.class).getObject("alpha_te"));
    ScalarGlobalParameter ParBeta_te = ((ScalarGlobalParameter)
Sim.get(GlobalParameterManager.class).getObject("beta_te"));
    ScalarGlobalParameter ParDelta_Y_te = ((ScalarGlobalParameter)
Sim.get(GlobalParameterManager.class).getObject("delta_Y_te"));
    ScalarGlobalParameter ParR_le_lo = ((ScalarGlobalParameter)
Sim.get(GlobalParameterManager.class).getObject("r_le_lo"));
    ScalarGlobalParameter ParR_le_up = ((ScalarGlobalParameter)
Sim.get(GlobalParameterManager.class).getObject("r_le_up"));
    ScalarGlobalParameter ParX_lo = ((ScalarGlobalParameter)
Sim.get(GlobalParameterManager.class).getObject("X_lo"));
    ScalarGlobalParameter ParX_up = ((ScalarGlobalParameter)
Sim.get(GlobalParameterManager.class).getObject("X_up"));
    ScalarGlobalParameter ParY_lo = ((ScalarGlobalParameter)
Sim.get(GlobalParameterManager.class).getObject("Y_lo"));
    ScalarGlobalParameter ParY_te = ((ScalarGlobalParameter)
Sim.get(GlobalParameterManager.class).getObject("Y_te"));
    ScalarGlobalParameter ParY_up = ((ScalarGlobalParameter)
Sim.get(GlobalParameterManager.class).getObject("Y_up"));
    ScalarGlobalParameter ParY_xx_lo = ((ScalarGlobalParameter)
Sim.get(GlobalParameterManager.class).getObject("Y_xx_lo"));
```

```
    ScalarGlobalParameter ParY_xx_up = ((ScalarGlobalParameter)
Sim.get(GlobalParameterManager.class).getObject("Y_xx_up"));


    // Root

    double alpha_te = ParAlpha_te.getQuantity().getSIValue();
    double beta_te = ParBeta_te.getQuantity().getSIValue();
    double delta_Y_te = ParDelta_Y_te.getQuantity().getSIValue();
    double r_le_lo = ParR_le_lo.getQuantity().getSIValue();
    double r_le_up = ParR_le_up.getQuantity().getSIValue();
    double X_lo = ParX_lo.getQuantity().getSIValue();
    double X_up = ParX_up.getQuantity().getSIValue();
    double Y_lo = ParY_lo.getQuantity().getSIValue();
    double Y_up = ParY_up.getQuantity().getSIValue();
    double Y_te = ParY_te.getQuantity().getSIValue();
    double Y_xx_lo = ParY_xx_lo.getQuantity().getSIValue();
    double Y_xx_up = ParY_xx_up.getQuantity().getSIValue();


    //Root

    double [][] A_up = {{1,1,1,1,1,1,},
                        {Math.pow(X_up,0.5),Math.pow(X_up,1.5),Math.pow(X_up,2
.5),Math.pow(X_up,3.5),Math.pow(X_up,4.5),Math.pow(X_up,5.5)},
                        {0.5,1.5,2.5,3.5,4.5,5.5},
                        {0.5*Math.pow(X_up,-
0.5),1.5*Math.pow(X_up,0.5),2.5*Math.pow(X_up,1.5),3.5*Math.pow(X_up,2.5),4.5*
Math.pow(X_up,3.5),5.5*Math.pow(X_up,4.5)},
                        {-0.25*Math.pow(X_up, -1.5), 0.75*Math.pow(X_up, -
0.5), (15.0/4.0)*Math.pow(X_up, 0.5), (35.0/4.0)*Math.pow(X_up, 1.5),
(63.0/4.0)*Math.pow(X_up, 2.5), (99.0/4.0)*Math.pow(X_up, 3.5)},
                        {1,0,0,0,0,0}



    };

    double [][] b_up = {{Y_te+0.5*delta_Y_te},
                        {Y_up},
                        {Math.tan((2*alpha_te - beta_te)/2)},
                        {0},
                        {Y_xx_up},
                        {Math.pow(r_le_up,0.5)}
    };


    double [][] A_lo = {{1,1,1,1,1,1,},
```

```
                        {Math.pow(X_lo,0.5),Math.pow(X_lo,1.5),Math.pow(X_lo,2
.5),Math.pow(X_lo,3.5),Math.pow(X_lo,4.5),Math.pow(X_lo,5.5)},
                        {0.5,1.5,2.5,3.5,4.5,5.5},
                        {0.5*Math.pow(X_lo,-
0.5),1.5*Math.pow(X_lo,0.5),2.5*Math.pow(X_lo,1.5),3.5*Math.pow(X_lo,2.5),4.5*
Math.pow(X_lo,3.5),5.5*Math.pow(X_lo,4.5)},
                        {-0.25*Math.pow(X_lo, -1.5), 0.75*Math.pow(X_lo, -
0.5), (15.0/4.0)*Math.pow(X_lo, 0.5), (35.0/4.0)*Math.pow(X_lo, 1.5),
(63.0/4.0)*Math.pow(X_lo, 2.5), (99.0/4.0)*Math.pow(X_lo, 3.5)},
                        {1,0,0,0,0,0}

    };

    double [][] b_lo = {{Y_te - 0.5*delta_Y_te},
                        {Y_lo},
                        {Math.tan((2*alpha_te + beta_te)/2)},
                        {0},
                        {Y_xx_lo},
                        {-1.0*Math.pow(r_le_lo,0.5)}};


    // Root
    Matrix A_up_M = new Matrix(A_up);
    Matrix b_up_M = new Matrix(b_up);
    Matrix A_lo_M = new Matrix(A_lo);
    Matrix b_lo_M = new Matrix(b_lo);


    //Root
    Matrix a_matrix = A_up_M.solve(b_up_M);
    Matrix b_matrix = A_lo_M.solve(b_lo_M);

    //Root
    double [][] a = a_matrix.getArray();
    double [][] b = b_matrix.getArray();


    int N = 50; //number of points to use

    //Root
    double xu;
    double yu;
    double xl;
    double yl;
    double[] xu_a = new double[N+1];
    double[] yu_a = new double[N+1];
    double[] xl_a = new double[N+1];
    double[] yl_a = new double[N+1];
    for (int i = 0; i < N + 1; i++){
```

```
      double i_d = (double) i;
      double N_d = (double) N;
      double xi = i_d/N_d;

      //Root
      xu = (Math.sin((xi - 0.5)*Math.PI) + 1.0)/2.0;
      xl = (Math.sin((xi - 0.5)*Math.PI) + 1.0)/2.0;
      yu = 0.0;
      yl = 0.0;

      for (int n = 0; n < 6; n++){
        //Root
        yu += a[n][0] * Math.pow(xu, ((float) n + 1.0) - 0.5);
        yl += b[n][0] * Math.pow(xl, ((float) n + 1.0) - 0.5);
      }
      //Root
      yu_a[i] = yu;
      xu_a[i] = xu;
      yl_a[i] = yl;
      xl_a[i] = xl;

    }

    String Dir = Sim.getSessionDir();

    //Root
    String fileName = Dir + File.separator + "PARSEC.csv";
    Sim.println("Root saved to " + fileName);

    double root_chordlength = 2e-01;
    double te_u_root_pt = 0.;
    double te_l_root_pt = 0.;

    FileWriter fw;
    try {
        fw = new FileWriter(new File(fileName));
        //Write the CSV file header
        //fw.write("x,y,z");
        //fw.write(System.lineSeparator());
        //Write table until N
        for (int i = 0; i < N + 1; i++) {
            fw.write(String.format(Locale.US, "%f,%f,%f", xu_a[N-
i]*root_chordlength, yu_a[N-i]*root_chordlength, 0.0));
            fw.write(System.lineSeparator());
            if (i==0){
                te_u_root_pt = yu_a[N-i]*root_chordlength;
                // Sim.println("Up - Root - Done");
            }
```

```
        }
        for (int i = 1; i < N + 1; i++) {
            fw.write(String.format(Locale.US, "%f,%f,%f",
xl_a[i]*root_chordlength, yl_a[i]*root_chordlength, 0.0));
            fw.write(System.lineSeparator());
            if (i==N){
                te_l_root_pt = yl_a[i]*root_chordlength;
                // Sim.println("Lo - Root - Done");
            }
        }

        fw.close();

        // Sim.println("CSV file was created successfully !!!");

    } catch (Exception ex) {
        Sim.println("OOPS !?!");
    }


    CadModel cadModel_0 =
      ((CadModel) Sim.get(SolidModelManager.class).getObject("Domain"));


    Sim.get(SolidModelManager.class).editCadModel(cadModel_0);

    Sim.println("#############################################################
#####################################");
    Sim.println("Starting with Root");

    Sketch3D sketch3D_0 =
      ((Sketch3D) cadModel_0.getFeature("Root"));
    cadModel_0.getFeatureManager().rollBack(sketch3D_0, false);
    cadModel_0.getFeatureManager().rollForward(sketch3D_0, true, false);
    sketch3D_0.setAutoPreview(true);
    cadModel_0.allowMakingPartDirty(false);
    cadModel_0.getFeatureManager().updateModelForEditingFeature(sketch3D_0);
    cadModel_0.getFeatureManager().startSketch3DEdit(sketch3D_0);
    SplineSketchPrimitive3D splineSketchPrimitive3D_0 =
      ((SplineSketchPrimitive3D) sketch3D_0.getSketchPrimitive3D("Spline 1"));
    Sim.println("Fetching Root from " + fileName);
    sketch3D_0.replaceSketchPrimitive3d(splineSketchPrimitive3D_0, fileName);
    sketch3D_0.setIsBodyGroupCreation(false);
    cadModel_0.getFeatureManager().markDependentNotUptodate(sketch3D_0);
    sketch3D_0.markFeatureForEdit();
    cadModel_0.allowMakingPartDirty(true);
    cadModel_0.getFeatureManager().stopSketch3DEdit(sketch3D_0, false);
    cadModel_0.getFeatureManager().markDependentNotUptodate(sketch3D_0);
```

```
    Sim.println("###################################################################################################");
    Sim.println("Starting with Domain Subtraction");

    cadModel_0.getFeatureManager().rollForwardToEnd(false);

    Sim.get(SolidModelManager.class).endEditCadModel(cadModel_0);


    Sim.println("Model Successfully Updated");


  }
}
```

Appendix F – PARSEC Parameter Bound Investigation

The initial case where δ = 0.5, and the upper and lower bounds calculated using equations (22), the covariance matrix is shown in Figure 73. (The values of the bounds used are given in at the end of the subsection in Table 9).

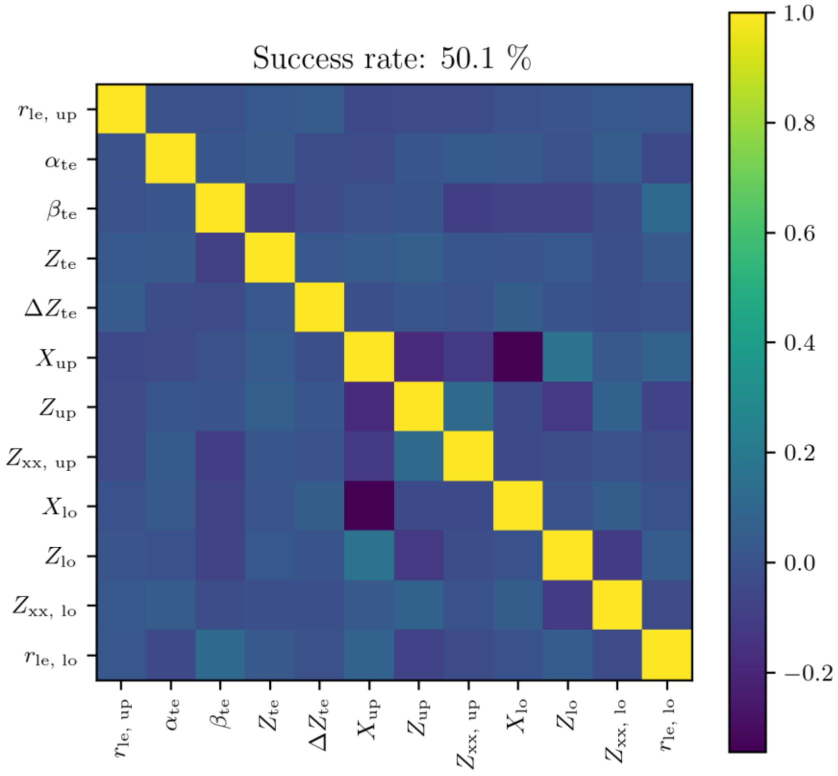

Figure 73: Covariance matrix of the failed designs with $\delta = 0.5$.

Another visual way of identifying which parameters caused the designs to fail was to simply plot each parameter as a function of every other parameter. Clusters of many points which do not seem form part of the rest of the points indicated which parameters were too high or too low.

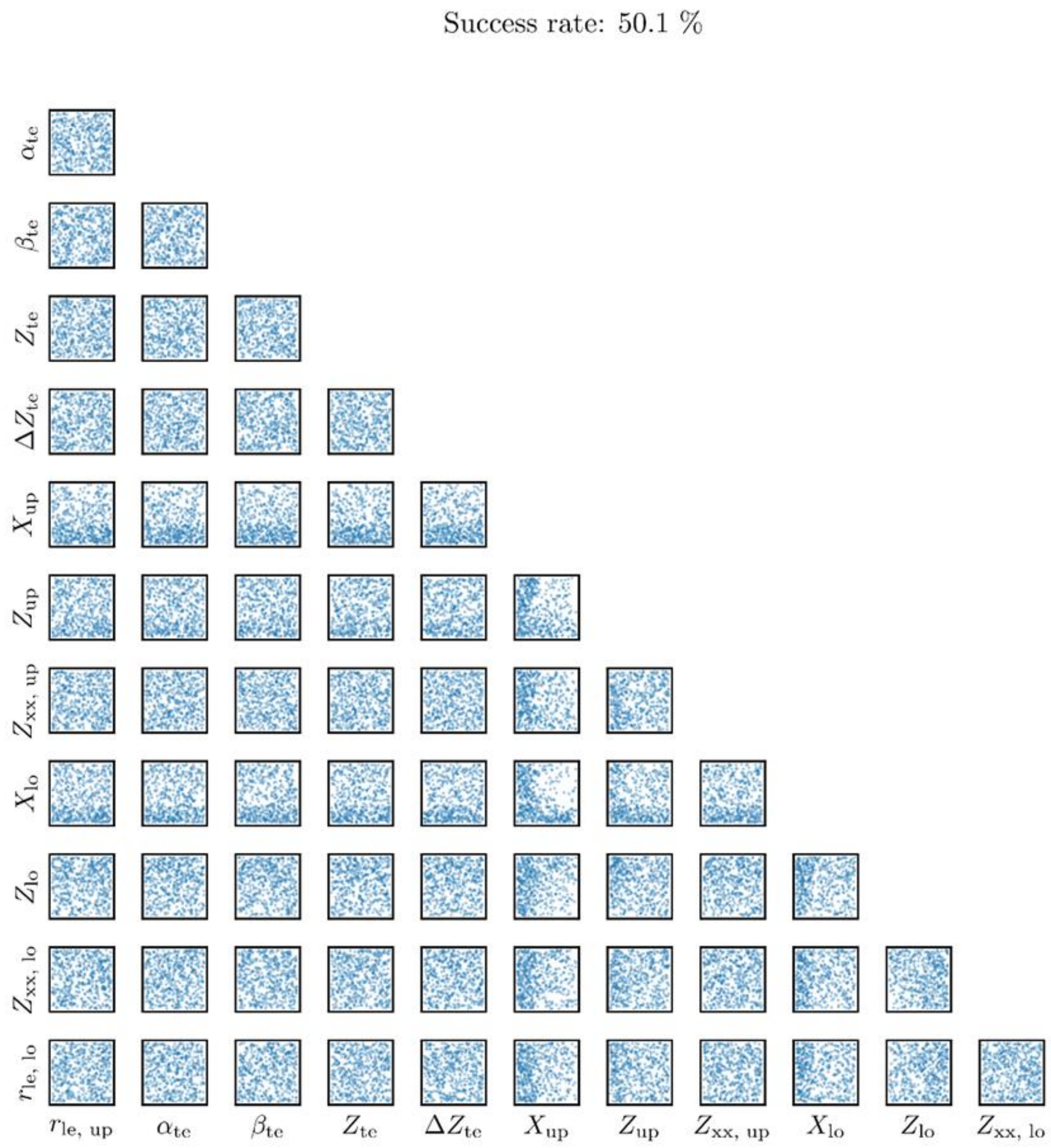

Figure 74: Scatter plots of each PARSEC parameter as a function of every other PARSEC parameter for all failed designs with $\delta = 0.5$.

It is obvious that presenting more plots like that shown in Figure 74 would be unnecessary due to the size thereof. From only Figure 74, the idea behind the cluster formations can be seen when looking at the X_{lo} and X_{up} data. There are thicker bands formed for lower X_{lo} values. Similarly, there are thicker bands formed for lower values of X_{up}. This fact is exactly pointed out in Figure 73, where the covariance matrix values for X_{lo} and X_{up} are clearly the largest in absolute value.

An attempt can now be made to slightly increase the lower bounds of X_{lo} and X_{up} because of the thicker bands formed at the lower range of X_{lo} and X_{up} according to Figure 74 (Table 9 at the end of the subsection shows the new bounds used to investigate if the success rate increased). The lower bounds were increased to $X_{lo} = 0.3$ and $X_{up} = 0.35$, a 30% and 5% decrease from the baseline values, instead of 50%, which made morphological sense given that the maximum thickness of the GHA wing would always be at the bone and very little deviation is expected in the chordwise direction. The Z_{te} upper bound was changed to 0.15 to accommodate the expected morphing of the trailing edge, a characteristic of feathered wings (Nachtigall and Wieser, 1966). The new covariance matrix was obtained and shown in Figure 75. From this figure it can be seen that the success rate increased, drastically, to above 80%. This method was therefore useful to obtain the largest design space possible, while still maintaining the morphological accuracy of a real GHA wing. If the success rate had to be increased to 100%, the same method can be used, and the next parameter to be changed is likely Z_{up}, but this is not recommended as an increase in Z_{up} upper limit may result in geometries outside the natural morphological limits of the GHA wing (i.e., the skin and feathers above the bone are not expected to deform significantly when the bird is in flight). Thus, the success rate of $> 80\%$ is deemed sufficient for the purposes of this study.

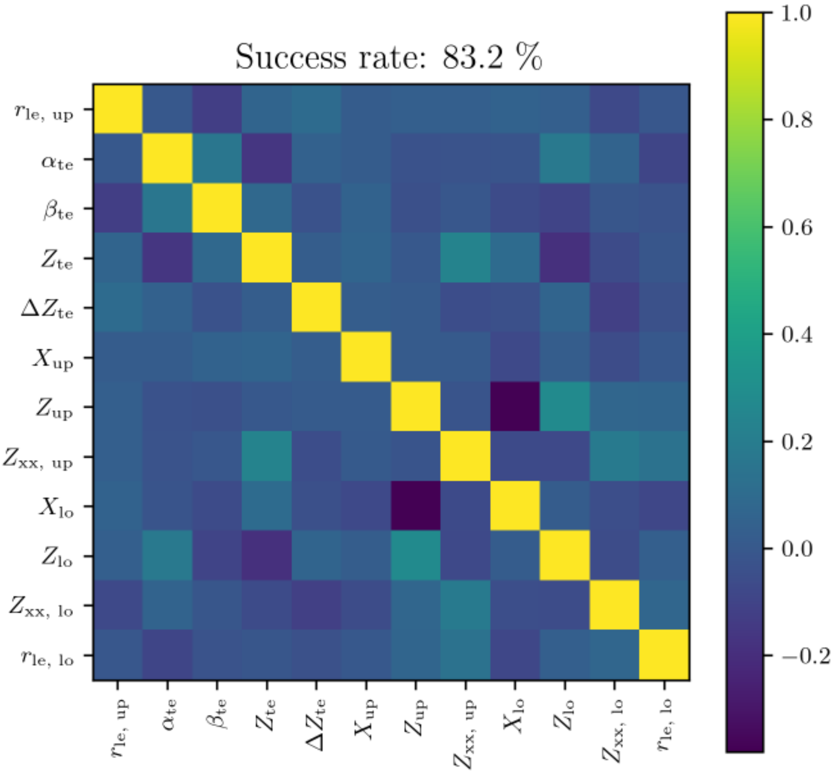

Figure 75: Covariance matrix of the PARSEC parameters after adjusting the bounds.

The original and new lower and upper bounds of the arm and hand airfoil of the GHA is shown in Table 9 and Table 10.

Table 9: PARSEC parameters bounds and baseline values for the arm section (a) before (50% success rate) and (b) after (80% success rate) updating the X_{lo}, X_{up},β_{te}, and Z_{te} bounds.

(a)

Parameter	Lower Bound	Baseline	Upper Bound
$r_{\mathrm{le,\,lo}}$	0.0702	0.1405	0.2107
$r_{\mathrm{le,\,up}}$	0.1243	0.2485	0.3728
X_{lo}	0.2115	0.4230	0.6346
X_{up}	0.1841	0.3683	0.5524
Z_{lo}	0.0566	0.1131	0.1697
Z_{up}	0.1308	0.2616	0.3924
$Z_{\mathrm{xx,\,up}}$	-3.1084	-2.0722	-1.0361
$Z_{\mathrm{xx,\,lo}}$	-1.8747	-1.2498	-0.6249
α_{te}	-48.8888	-32.5926	-16.2963
β_{te}	8.8457	17.6914	26.5371
Z_{te}	0.0053	0.0106.	0.0159
ΔZ_{te}	0.0100	0.0199	0.0299

(b)

Parameter	Lower Bound	Baseline	Upper Bound
$r_{\mathrm{le,\,lo}}$	0.0702	0.1405	0.2107
$r_{\mathrm{le,\,up}}$	0.1243	0.2485	0.3728
X_{lo}	0.3000	0.4230	0.6346
X_{up}	0.3500	0.3683	0.5524
Z_{lo}	0.0566	0.1131	0.1697
Z_{up}	0.1308	0.2616	0.3924
$Z_{\mathrm{xx,\,up}}$	-3.1084	-2.0722	-1.0361
$Z_{\mathrm{xx,\,lo}}$	-1.8747	-1.2498	-0.6249
α_{te}	-48.8888	-35.5926	-16.2963
β_{te}	8.8457	17.6914	30
Z_{te}	0.0053	0.0106	0.1500
ΔZ_{te}	0.0100	0.0199	0.0299

Table 10: PARSEC parameters bounds and baseline values for the hand section (a) before (50% success rate) and (b) after (80% success rate) updating the X_{lo}, X_{up},β_{te}, and Z_{te} bounds.

(a)

Parameter	Lower Bound	Baseline	Upper Bound
$r_{\mathrm{le,\,lo}}$	0.0221	0.0441	0.0662
$r_{\mathrm{le,\,up}}$	0.0674	0.1348	0.2021
X_{lo}	0.1887	0.3774	0.5661
X_{up}	0.1715	0.3431	0.5146
Z_{lo}	0.0364	0.0728	0.1092
Z_{up}	0.0755	0.1509	0.2264
$Z_{\mathrm{xx,\,up}}$	-1.6237	-1.0825	-1.5412
$Z_{\mathrm{xx,\,lo}}$	-1.1031	-0.7354	-0.3677
α_{te}	-27.7361	-18.4907	-9.2454
β_{te}	-4.1369	-2.7579	-1.3790
Z_{te}	0.0065	0.0130	0.0195
ΔZ_{te}	0.027	0.0054	0.0081

(b)

Parameter	Lower Bound	Baseline	Upper Bound
$r_{\mathrm{le,\,lo}}$	0.0221	0.0441	0.0662
$r_{\mathrm{le,\,up}}$	0.0674	0.1348	0.2021
X_{lo}	0.3000	0.3774	0.5661
X_{up}	0.2900	0.3431	0.5146
Z_{lo}	0.0364	0.0728	0.1092
Z_{up}	0.1200	0.1509	0.2264
$Z_{\mathrm{xx,\,up}}$	-1.6237	-1.0825	-1.5412
$Z_{\mathrm{xx,\,lo}}$	-1.1031	-0.7354	-0.3677
α_{te}	-27.7361	-18.4907	-9.2454
β_{te}	-4.1369	-2.7579	30.0000
Z_{te}	0.0065	0.0130	0.1
ΔZ_{te}	0.027	0.0054	0.0081